

DOT/FAA/AR-04/45,P1

Office of Aviation Research
Washington, D.C. 20591

Lightweight Ballistic Protection of Flight-Critical Components on Commercial Aircraft

Part 1: Ballistic Characterization of Zylon

December 2004

Final Report

This document is available to the U.S. public
through the National Technical Information
Service (NTIS), Springfield, Virginia 22161.



U.S. Department of Transportation
Federal Aviation Administration

NOTICE

This document is disseminated under the sponsorship of the U.S. Department of Transportation in the interest of information exchange. The United States Government assumes no liability for the contents or use thereof. The United States Government does not endorse products or manufacturers. Trade or manufacturer's names appear herein solely because they are considered essential to the objective of this report. This document does not constitute FAA certification policy. Consult your local FAA aircraft certification office as to its use.

This report is available at the Federal Aviation Administration William J. Hughes Technical Center's Full-Text Technical Reports page: actlibrary.tc.faa.gov in Adobe Acrobat portable document format (PDF).

1. Report No. DOT/FAA/AR 04/45,P1		2. Government Accession No.		3. Recipient's Catalog No.	
4. Title and Subtitle LIGHTWEIGHT BALLISTIC PROTECTION OF FLIGHT-CRITICAL COMPONENTS ON COMMERCIAL AIRCRAFT PART 1: BALLISTIC CHARACTERIZATION OF ZYLON				5. Report Date December 2004	
				6. Performing Organization Code	
7. Author(s) Kelvin Kwong and Werner Goldsmith				8. Performing Organization Report No.	
9. Performing Organization Name and Address University of California, Berkeley Berkeley, California 94720-5940				10. Work Unit No. (TRAIS)	
				11. Contract or Grant No.	
12. Sponsoring Agency Name and Address U.S. Department of Transportation Federal Aviation Administration Office of Aviation Research Washington, DC 20591				13. Type of Report and Period Covered Final Technical Report 1/2002 - 3/2003	
				14. Sponsoring Agency Code ANE-100, ANM-100	
15. Supplementary Notes The Federal Aviation Administration William J. Hughes Technical Center COTR was Donald Altobelli.					
16. Abstract <p>The University of California, Berkeley collaborated with The Boeing Company and SRI International to develop a lightweight ballistic protection for flight-critical components on commercial aircraft. Berkeley's role in support of this program was to provide small-scale ballistic testing and computational analysis. This report (part 1) describes the work performed and the results obtained by UC Berkeley. Separate parts of this report describe Boeing and SRI results.</p> <p>This report presents the results of an experimental study of the effects of normal impact on various numbers of adjacent Zylon[®] 35x35 and Kevlar[®] 29x29 sheets. As part of an effort to contain rotor burst fragments in commercial aircraft, a fragment simulator (right circular steel cylinder with a 1.27 cm (1/2 inch) diameter and 3.81 cm (1 1/2 inch) length) was fired at normal incidence against a 25.4- by 25.4-cm (10- by 10-inch) window of fabric at velocities of 57 m/s to 342 m/s (187 ft/sec to 1122 ft/sec). This study tested four different boundary conditions: (1) four clamping sides, (2) two clamping sides, (3) four corner pegs, and (4) eight pegs. The experimental investigation also considers the effects of three shot locations: (1) center shots, (2) diagonal shots, and (3) midway shots.</p> <p>From the ballistic tests, Zylon displayed better ballistic performance than Kevlar. Of the four different boundary conditions, the four- and eight-peg configuration absorbed the greatest amount of impact energy per ply without complete penetration. The shot location did not significantly affect the ballistic performance of the fabric.</p>					
17. Key Words Zylon, Target fabric, Target holder, Clamping edges			18. Distribution Statement This document is available to the public through the National Technical Information Service (NTIS) Springfield, Virginia 22161.		
19. Security Classif. (of this report) Unclassified		20. Security Classif. (of this page) Unclassified		21. No. of Pages 108	22. Price

TABLE OF CONTENTS

	Page
EXECUTIVE SUMMARY	ix
1. INTRODUCTION	1
1.1 Background	1
1.2 Motivation for the Study	2
1.3 Previous Studies on Zylon	2
1.4 Theoretical Considerations	3
1.5 Experimental Objective	4
2. EXPERIMENTAL SYSTEM AND PROCEDURE	4
2.1 Apparatus and Test Arrangement	4
2.1.1 Powder Gun	5
2.1.2 Velocity Measurement Techniques	5
2.1.3 Projectiles	6
2.1.4 Powder and Cartridges	6
2.1.5 Target Fabric	6
2.1.6 Target Holder	7
2.1.7 Target Mount	7
2.1.8 Blast Shield	7
2.1.9 Catcher Box	7
2.2 Test Procedures	7
2.2.1 Four-Clamp Configuration	8
2.2.2 Two-Clamp Configuration	8
2.2.3 Four-Peg Configuration	8
2.2.4 Eight-Peg Configuration	9
2.3 Test Setup	9
3. RESULTS AND DISCUSSION	10
3.1 Accuracy of Results	10
3.2 Four-Clamp Configuration/Center Shot/Zylon/Kevlar	12
3.3 Two-Clamp Configuration/Center Shot/Zylon/Kevlar	13
3.4 Four-Peg Configuration/Center Shot/Zylon/Kevlar	13
3.5 Eight-Peg Configuration/Center Shot/Zylon	15
3.6 Four-Clamp Configuration/Diagonal Shot/Zylon	16
3.7 Two-Clamp Configuration/Midway Shot/Zylon	16
3.8 Four-Peg Configuration/Diagonal Shot/Zylon	17

3.9	Eight-Peg Configuration/Diagonal Shot/Zylon	17
3.10	Comparison of Nonperforation and Complete Perforation Shots	18
4.	CONCLUSIONS AND RECOMMENDATIONS	18
5.	REFERENCES	19
APPENDICES		
	A—Modeling of the Ballistic Limit of Micro-Stochastic Fabric Shielding	
	B—Lightweight Ballistic Protection of Flight-Critical Components on Commercial Aircraft	
	C—Results of Small-Scale Impact Tests	
	D—Data Reduction Background	
	E—Derivation for the Force-Deflection Equation	

LIST OF FIGURES

Figure		Page
1	A DC-10 Aircraft	22
2	Zylon 35x35 Fabric Used in This Study	22
3	Experimental System in the Ballistics Laboratory	23
4	The Powder Gun	23
5	Back View of the Powder Gun	24
6	Side View of the Powder Gun	24
7	Top View of the Powder Gun	25
8	Powder Gun Breech	25
9	Uniphase Helium-Neon Gas Laser and Custom Photodiode	26
10	Paper Grid Targets With Alligator Clips Attached at the Bottom	26
11	Paper Targets After Perforation	27
12	Close-Up of Interlocking Conducting Ink Lines	27
13	Unused Paper Grid	28
14	Digital Video Camera Unit	28
15	Digital Camera Still of Test 64E	29
16	Digital Camera Still of Test 55E	29
17	Control Unit for the Digital Video Camera	30
18	Right Circular Cylindrical Projectile Shown With a .50 Caliber Cartridge	30
19	Cross Section of Hexagonal Tongue and Groove Used to Lock the Fabric in the Target Holder	31
20	Hexagon Groove on the Clamping Edge	31
21	Close-Up of the Complete Hexagonal Tongue and Groove System	32
22	Complete Target Holder With all Four Clamps	32

23	Target Mount Attached to the Powder Gun Table	33
24	Target Holder Attached to the Target Mount by Four C-Clamps	33
25	Blast Shield in Front of the Muzzle of the Powder Gun	34
26	Catcher Box Filled With Rags, Foam, and Newspaper	34
27	Side View of the Clamping Edge Installed Into the Target Holder	35
28	All Four Clamping Edges Installed With Nuts and Bolts Tightened	35
29	Front View of all Four Clamping Edges	36
30	Back View of all Four Clamping Edges	36
31	Target Holder in a Two Clamp Configuration	37
32	Arrowhead Cutter	37
33	The Four-Peg Configuration	38
34	The Four-Peg Configuration With Zylon Installed	38
35	The Eight-Peg Configuration	39
36	The Firing Switch	39
37	Sketch of the Damage Pattern on the Fabric in the Target Holder From a Center Shot	40
38	Slip at the Target Holder Boundary, Indicated by the Displacement of the Black Marker Line	40
39	Initial vs Residual Velocity for Zylon and Kevlar—Four-Clamp Center Shots	41
40	Impact Energy vs Absorbed Energy for Zylon and Kevlar—Four-Clamp Center Shots	41
41	Initial vs Residual Velocity for Zylon and Kevlar—Two-Clamp Center Shots	42
42	Impact Energy vs Absorbed Energy for Zylon and Kevlar—Two-Clamp Center Shots	42
43	Initial vs Residual Velocity for Zylon and Kevlar—Four-Peg Center Shots	43
44	Impact Energy vs Absorbed Energy for Zylon and Kevlar—Four-Peg Center Shots	43

45	Initial vs Residual Velocity for Zylon—Eight-Peg Center Shots	44
46	Impact Energy vs Absorbed Energy for Zylon—Eight-Peg Center Shots	44
47	Initial vs Residual Velocity for Zylon—Four-Clamp Diagonal Shots	45
48	Impact Energy vs Absorbed Energy for Zylon—Four-Clamp Diagonal Shots	45
49	Impact Energy vs Absorbed Energy for Zylon—Comparison Between Four-Clamp Center and Diagonal Shots	46
50	Initial vs Residual Velocity for Zylon—Two-Clamp Midway Shots	46
51	Impact Energy vs Absorbed Energy for Zylon—Two-Clamp Midway Shots	47
52	Impact Energy vs Absorbed Energy for Zylon—Comparison Between Two-Clamp Center and Midway Shots	47
53	Initial vs Residual Velocity for Zylon—Four-Peg Diagonal Shots	48
54	Impact Energy vs Absorbed Energy for Zylon—Four-Peg Diagonal Shots	48
55	Impact Energy vs Absorbed Energy for Zylon—Comparison Between Four-Peg Center and Diagonal Shots	49
56	Initial vs Residual Velocity for Zylon—Eight-Peg Diagonal Shots	49
57	Impact Energy vs Absorbed Energy for Zylon—Eight-Peg Diagonal Shots	50
58	Impact Energy vs Absorbed Energy for Zylon—Comparison Between Eight-Peg Center and Diagonal Shots	50
59	Impact Energy vs Absorbed Energy for Zylon—All Diagonal Shots	51
60	Impact Energy vs Absorbed Energy for Zylon and Kevlar—All Center Shots	51

LIST OF TABLES

Table	Page
Summary of Absorbed Energies for Nonperforating Shots	52

LIST OF ACRONYMS

FAA	Federal Aviation Administration
PBO	Poly- benzoxazole (generic) poly-benzobisoxazole (Zylon [®])
UC	University of California
ACFPP	Aircraft Catastrophic Failure Prevention Program

EXECUTIVE SUMMARY

Uncontained turbine engine failures remain a cause of commercial aircraft incidents and has led to catastrophic aircraft accidents. To mitigate the effect of uncontained engine debris on critical aircraft components, the Federal Aviation Administration (FAA) under the Aircraft Catastrophic Failure Prevention Program, has sponsored research to develop lightweight barrier systems for aircraft and to develop the computational capability to design these barriers.

The goal of this research project, carried out under the auspices of the FAA Airworthiness Assurance Center of Excellence, was to use the technical strengths and experience of the Boeing Company, SRI International, and the University of California, Berkeley, to develop rotor burst fragment aircraft shielding and finite element modeling methodology. Since the development of an experimental set of data to support the calibration of the finite element models was essential, various experimental methods were used to measure material and structural response of the fabrics.

Each member of the team developed a report describing the details and the findings of their research task. The comprehensive report, “Lightweight Ballistic Protection of Flight-Critical Components on Commercial Aircraft,” is comprised of the following three parts.

- Part 1: “Small Scale Testing and Computational Analysis” by the University of California, Berkeley.
- Part 2: “Large-Scale Ballistic Impact Tests and Computational Simulations” by SRI International.
- Part 3: “Zylon Yarn Tests” by the Boeing Company.

This report (part 1) summarizes the results of an experimental study of the effects of ballistic impact on various numbers of adjacent Zylon[®] AS-500 Denier 35x35 weave and Kevlar[®] KM-2-600 Denier 29x29 weave sheets. As part of an effort to mitigate engine rotor burst fragments in commercial aircraft, a fragment simulator (right circular steel cylinder with a 1.27 cm (1/2 inch) diameter and 3.81 cm (1 1/2 inch) length) was fired at normal incidence against a 10- by 10-inch window of fabric at velocities of 57 m/s to 342 m/s (187 ft/sec to 1122 ft/sec). This study tested four different boundary conditions: (1) four clamp edges, (2) two clamp edges, (3) four corner pegs, and (4) eight pegs. The study also considered the effects of three shot locations: (1) center shots, (2) diagonal shots, and (3) midway shots.

From the ballistic tests, Zylon displayed better ballistic performance than Kevlar. Of the four different boundary conditions, the four-peg and eight-peg configuration absorbed the greatest amount of impact energy per ply without complete penetration. The shot location did not significantly affect the ballistic performance of the fabric.

Appendix A contains the computational results from this study.

1. INTRODUCTION.

1.1 BACKGROUND.

To mitigate the effect upon critical aircraft components of uncontained fragments from turbine engine failures, the Federal Aviation Administration (FAA) under the Aircraft Catastrophic Failure Prevention Program (ACFPP), has sponsored research to develop lightweight barrier systems for aircraft and to develop a physics-based computational capability for designing these barriers.

Laboratory gas gun tests in which small-scale fragment simulators impacted a variety of potential barrier materials showed that woven fabrics of high-strength polymers, such as aramids (e.g., Kevlar[®]), polyethylenes (e.g., Spectra), and particularly poly-benzoxazole (PBO) (e.g., Zylon[®]), had very high energy absorption per unit weight in impact tests against fragment simulators. Full-scale fragment impact tests against aircraft fuselage sections fortified with the woven fabric confirmed the suitability of these materials as fragment barriers.

SRI International developed a computational capability for high-strength fabrics by modeling the geometry, properties, and interactions of individual yarns within the woven fabric. Input to the model was provided by laboratory tests to measure yarn tensile and friction properties, quasi-static penetration tests to measure the evolution and phenomenology of fabric deformation and failure, and projectile impact tests to measure the effects of fabric material, mesh density, boundary conditions (how a fabric is gripped), and projectile sharpness. The model was implemented in the LS-DYNA3D finite element code and used to simulate the failure behavior of yarns and fabrics under various scenarios. The resulting insights assisted barrier design. A simplified version of the detailed computational model has been developed to assist the transport aircraft industry in designing engine fragment barriers.

At the Fourth FAA Uncontained Engine Debris Characterization Modeling and Mitigation Workshop, the Boeing Company expressed interest in the potential of Zylon for protecting specific flight-critical components such as the rotary auxiliary turbine system and auxiliary fuel tanks for long-distance flights. SRI and Boeing discussed initiating a program in this area and invited University of California (UC), Berkeley, with its expertise in both ballistic impacts and finite element analyses, to join in these discussions.

UC Berkeley (teamed with SRI and Boeing) was granted an FAA Airworthiness Assurance Center of Excellence grant to do an experimental and computational study program to transition the results of the research grant to an industrial application, using Zylon ballistic fabric barriers for protection against transport airplane rotor burst fragments. Ballistic tests were performed to characterize the ballistic effectiveness of Zylon barriers against a range of realistic fragment threats in specific test cases of interest to transport aircraft. SRI's finite element Zylon computational model was then adapted, as needed, to address these specific shielding scenarios, verified by comparison with the ballistic test results, and transferred to Boeing. Various mechanical, thermal, environmental, and compatibility tests were performed to address the suitability of the Zylon material for use on transport aircraft. This report summarizes the results of this study.

1.2 MOTIVATION FOR THE STUDY.

Many applications exist for fragment barriers, including body armor, automobile gas tanks, bomb shelters, military tanks, submarines, reinforced buildings, critical aircraft equipment, and other commercial components. Metals and composite structures have been used as fragment barriers in many applications; for example, Kevlar is used in bulletproof vests. Composites have received a lot of attention over the past decade due to their lightweight and high strength features. Zylon was of a particular interest to this experimental investigation.

Aircraft safety, when rotor compressor blades fail, is a critical problem. To reduce the number of in-flight accidents, the FAA created the ACFPP. The program's goals were to investigate and integrate advance technologies into commercial aircraft to prevent future accidents. The problem of engine burst fragments crippling flight-critical components is a serious issue which needs to be resolved. In 1989, a DC-10's (Sioux City Accident, figure 1) engine burst fragments severed all three hydraulic lines, making the aircraft inoperable and resulting in casualties. To keep aircraft operational despite an unexpected turbine engine failure, the ACFPP focused their efforts in the area of fragment barriers.

1.3 PREVIOUS STUDIES ON ZYLON.

Zylon (poly-benzobisoxazole-PBO), a low-density and high-strength polymer, shows good potential to be the next-generation armor material. Manufactured by Toyobo Corporation, Zylon is available in various weaves (e.g., 35x35) and Deniers (unit of weight, measuring the fineness of the thread) (e.g., 500). Figure 2 shows the Zylon fabric used in this experimental investigation. According to Toyobo's technical data, Zylon AS (as spun) has a modulus of 180 GPa, elongation at break of 3.5%, and an ultimate stress of 5.7 GPa. Zylon has a 100°C higher decomposition temperature than p-Aramid fiber. The limiting oxygen index is 68, which is the highest among organic super fibers. For further material properties, see reference 1.

Studies conducted by SRI, in collaboration with the FAA, concluded that Zylon possesses mechanical properties that exceed those of existing armor materials, i.e., Kevlar, Spectra, etc. [2-9]. Not only possessing good resistance to heat, moisture, abrasion, and seawater corrosion, Zylon demonstrated advance ballistic performance, which makes it an ideal lightweight fragment barrier candidate. In addition to the FAA, Boeing is interested in the idea of furnishing their aircraft with Zylon to protect the fuselage and other critical in-flight components from turbine engine fragments. As a result, Boeing investigated Zylon material properties such as (1) stress/strain behavior; (2) thermal characteristics, including the coefficient of thermal expansion, thermal conductivity, and ignition temperature; (3) effects of environmental exposure, including light, moisture, temperature; and (4) other issues, including toxicity and chemical compatibility. Toyobo, SRI, and Boeing have independently measured the material properties of Zylon. The Boeing results are included in part 3 of this comprehensive report.

The U.S. Army has also taken an interest in Zylon for body armor applications. Tests conducted at UC Berkeley, in collaboration with the U.S. Army, have investigated Zylon as a candidate for bulletproof vest applications [10 and 11].

1.4 THEORETICAL CONSIDERATIONS.

The mechanics of projectile impact on targets constitutes a complex phenomenon. Although numerical and analytical models exist for ideal conditions, experimental testing is necessary to validate any model and to gain a better understanding of the process. Before presenting the results of this experimental investigation, a review of past work in this field is presented.

Cunniff developed mathematical relations to assist in the design of efficient textile-based body armor systems [12-20]. With dimensionless parameters such as $(A_d A_p / m_p)$, where A_d is the system areal density, A_p is the projectile presented area, and m_p is the projectile mass, a designer can initially screen out materials and identify the candidate fibers with the most potential to be used as fabric barriers. In addition, Cunniff developed a design tool to estimate the ballistic behaviors of materials where no prior data exists [13]. Through the testing of right circular cylinders, chisel-nosed fragment simulators, and steel cubes, Cunniff derived results that can be used to estimate the ballistic limit, V_{50} , variability in V_{50} due to test conditions and procedures, and variability in the material system. With these findings, approximations can be made about the V_{50} and impact velocity-residual velocity curves for fabric barriers with limited data. Using the same impact testing techniques as in this investigation, Cunniff also analyzed the ballistic behavior of a number of fabric barriers [14]. PBO, Kevlar KM2, Kevlar 29/49/129, Nylon, Spectra 1000, M5, and Enka were some of the fabrics investigated for body armor applications.

Similar to Cunniff, Izdebski and Bryant conducted impact tests to determine the ballistic behavior of composite Kevlar 49 panels [21]. Like this experimental investigation, right circular cylinders were fired against the composite barrier and the ballistic performance was recorded. The study provided a preliminary database for the shielding capabilities of the Kevlar panels and identified potential panel materials with ballistic resistance.

Lim, Shim, and Ng created a numerical model to simulate ballistic impact on Twaron fabric [22]. By using the nonlinear, three-dimensional finite element code DYNA3D, the impact behavior of the fabric barrier is simulated and the ballistic limit, energy absorption, and deflection profiles are determined. Further, Walker developed a constitutive model to represent the deflection of fabric barriers based on elastic deformation [23 and 24]. Using this model, an analytic expression was derived to estimate the ballistic limit for various projectile weights and numbers of fabric plies. Walker also examined the effects of resin on the ballistic limit of fabric barriers. This study provided an equation that approximates the ballistic limit curve of a composite panel when the ballistic limit curve of a fabric is known.

Of all the material reviewed, the most significant and related studies were the results published by Shockey, Erlich, and Simmons, which were concerned with improved barriers against turbine engine fragments [2-9]. In synergy with the present investigation, Zylon was closely examined as a potential fabric barrier candidate. Large-scale impact tests involved a 76.2-mm (3-in.) by 5.59-mm (0.22-in.) by 101.6-mm (4-in.) sharp-edged fragment weighing about 160 g (0.35 lb.), fired at speeds in the range of 200 m/s (656 ft/sec) at Zylon fabric attached to a fuselage. Along with large-scale impact tests, detailed computational fabric models were developed to simulate the deformation and failure behaviors. From initial studies, the computational model was able to predict within a 20% margin the energy absorbed during penetration. In general, the experimental investigation contained in this report is an extension of the Shockey, Erlich, and Simmons' studies.

In addition to Shockey, Erlich, and Simmons, Zohdi developed a simulation technique to approximate the number of fabric sheets that were needed to stop an incoming projectile [25]. Zohdi also examined the degree of response uncertainty due to misalignment of fibers. A computational model was developed to solve the stochastic system in order to relate the effects of this uncertainty to the number of sheets required to stop an incoming projectile, as shown in appendix A. The experimental results of this investigation will be used to test the accuracy of Zohdi's computational model, which accounts for scatter in laboratory experiments.

1.5 EXPERIMENTAL OBJECTIVE.

In this experimental investigation, the perforation limits and response to projectile impact at normal incidence for a number of adjacent plies of Zylon AS, 500 Denier, 35x35 weave (a low-density and high-strength polymer, manufactured by Toyobo Corporation and woven by Lincoln Fabrics) and Kevlar 49, 600 Denier, 29x29 weave are determined for eight different test configurations. The two fabric architectures were chosen to yield a similar areal weight for both Zylon and Kevlar. Right circular steel 600 Deniers, cylinders, a 1.27 cm (1/2 inch) in diameter and 3.81 cm (1 1/2 inch) long are fired against a 25.4- by 25.4-cm (10- by 10-in.) window of fabric. Specifically, this study examines the effects of four different boundary conditions: (1) four clamped edges, (2) two clamped edges, (3) four corner pegs, and (4) eight pegs (4 corner/4 midway along target holder). The experimental investigation also considers the effects of three shot locations: (1) center shots, (2) diagonal shots (halfway from the center to the corner), and (3) midway shots (halfway from the center to the perpendicular boundary edge). In the course of the tests, miscellaneous information, which contributes to the design of aircraft shielding applications, are noted. Appendix B contains the original test plan written by Boeing that was the basis for the UC Berkley testing. The plan was somewhat modified due to the lack of time and funding to complete all the planned tests.

The tests should reveal the general ballistic characteristics of Zylon from impacts of small-scale projectiles and their performance relative to Kevlar.

2. EXPERIMENTAL SYSTEM AND PROCEDURE.

2.1 APPARATUS AND TEST ARRANGEMENT.

The experimental system, shown in figure 3, consisted of nine components:

1. powder gun
2. velocity instrumentation
3. projectiles
4. powder and cartridges
5. target fabric
6. target holder
7. target mount
8. blast shield, and
9. catcher box

The following sections, give a detailed description of the components.

2.1.1 Powder Gun.

The powder gun, shown in figures 4 through 7, is 1.6 m (5.3 ft) long and has a 20-mm (0.79-in.)-thick, high-strength SAE 5130 steel smooth bore barrel with an inner diameter of 12.93 mm (0.51 in.). The breech of the powder gun is configured to insert standard 0.50 caliber cartridges and uses an interlocking mechanism to load the powder gun. The breech of the gun, shown in figure 8, is electrically triggered outside the ballistics laboratory. A pin in the breech is designed to strike the primer of the 0.50 caliber cartridges when firing. As a result of the interlock mechanism used to prevent premature firing, the laboratory door must be completely closed before pressing the firing button next to the door. To adjust the firing distance from the intended target, the gun is mounted on a sliding support rail, which is bolted securely to one end of a 680-kilogram (1,499 lb) cast iron table, which in turn, is also bolted securely to the floor of the ballistics laboratory.

2.1.2 Velocity Measurement Techniques.

The first method used to measure the initial velocity of the projectile employed, two parallel helium-neon gas laser beams, manufactured by Uniphase (figure 9), passing at right angles through the path of the gun barrel centerline. The helium-neon gas laser beam that is closest to the powder gun is positioned 507 mm (20 in.) beyond the powder gun muzzle. The helium-neon gas laser beams are 165 mm (6.5 in.) apart and are mounted on a platform, which has no physical connection with the powder gun setup. The two helium-neon gas laser beams are focused on two custom-designed photodiodes (figure 9), which each produce a positive voltage pulse (rise time ~2 microsecond (μ s)) as the laser beams are successively broken by the projectile. The successive signals start and stop a Hewlett-Packard 5316 time interval counter. The counter records the time the projectile passes through the 165-mm (6.5-in.) separated laser beams. From the separation distance and the recorded time interval, the initial velocity was calculated.

The second method used to measure the initial velocity employed paper grids, shown in figures 10 and 11. The paper grids were comprised of two independent sets of interlocking conducting ink lines, as shown in figures 12 and 13. The paper grids were positioned centrally and orthogonal in the path of the powder gun barrel centerline. The first paper grid was positioned 380 mm (15 in.) away from the muzzle of the powder gun and secured to an aluminum frame by four standard 25.4-mm (1-in.) binder spring clips. As shown in figures 11 through 13, each paper grid consisted of two ink line connection points with two alligator clips attached at the bottom, which are then connected to a Hewlett-Packard 5316 time interval counter. The counter records the time the projectile passes through the 184-mm (7.2-in.) distance separating the two paper grids. Successive signals are generated when the projectile forms a make-circuit by touching two adjacent conducting ink lines. Similar to the helium-neon laser beams, the successive signals provide a recorded time interval, which was used to calculate the velocity.

The third method used to measure the initial velocity employed the Kodak Motion Corder Analyzer (digital video camera) SR series, which is manufactured by Imatron (figure 14). The digital video camera records at a maximum rate of 10,000 frames per second and a maximum

shutter speed of 1/20000 sec. The 25-mm camera lens has a 40.5-mm (1.6-in.) [F/0.95]. The maximum field of view of the camera is 50.8 mm (2 in.) perpendicular to the projectile trajectory direction and 152.4 mm (6 in.) in the projectile trajectory direction (34 by 128 pixels). A scale is also placed in the field of view. The camera lens was orthogonal to the powder gun table and positioned 4.6 m (15 ft) away from the table.

The camera was focused on a front side mirror, which was positioned at 45° relative to the powder gun table and mounted directly above the target (see figure 3). With this configuration, the camera recorded the motion of the projectile before impact, the deformation of the target fabric, and the motion of the projectile exiting the target, in the case of perforation, as shown in figures 15 and 16. The projectile entered the field of view at approximately 1.45 m (4.75 ft) away from the powder gun muzzle. One high-intensity lamp (650 watts) (manufactured by Mole-Richardson Co.) was focused on the area before impact and another was focused on the area after impact. The velocity of the projectile was determined by using the digital video camera to track the distance the projectile traveled over a number of frames. The control unit (figure 17) for the camera was connected to a monitor, which displayed the captured video. The control unit has two important settings: framing rate and shuttering speed. The control unit can also playback the video footage instantly, frame by frame. The reticle (cross hairs) feature of the camera can pinpoint the projectile position in each frame. The video footage was digitally stored on a Dell Inspiron laptop computer. From the distance traveled by the projectile and the time interval, both the initial and final velocities were calculated.

As in the second initial velocity measurement method, paper targets were also used to measure the final velocity of the projectile. Again, the paper targets were positioned directly in the path of the gun barrel centerline, but downstream of the target.

2.1.3 Projectiles.

The right circular cylindrical projectile used in this experimental investigation is shown in figure 18. The projectile was machined from drill rod, which was heat-treated to a Rockwell Hardness of R_C60 and then completely plated with a 0.0127-mm- (0.0005-in.) -thick layer of copper. The projectile was nominally 12.7 mm (0.5 in.) in diameter by 38.1 mm (1.5 in.) long and fits into a standard 0.50 caliber cartridge. The mass of the projectile was 37 grams (0.082 lb).

2.1.4 Powder and Cartridges.

The standard 0.50 caliber cartridges were loaded with 3031 smokeless gun powder (manufactured by IMR Powder Company). A designated amount of powder was weighed on a scale and filled into the 0.50 caliber cartridge. Tissue was used to tamp the powder into the cartridge.

2.1.5 Target Fabric.

The tests were performed on 330-by 330-mm (13- by 13-in.) and 508- by 508-mm (20- by 20-in.) plies of both Zylon AS-500 Denier 35x35 weave and Kevlar KM-2-600 Denier 29x29 weave. These two fabric configurations resulted in similar areal densities of the Zylon and

Kevlar. The 330- by 330-mm (13- by 13-in.) plies of Zylon were cut from a 330-mm by 91.4-m roll, (13 in. by 300 ft) while the 508- by 508-mm (20- by 20-in.) plies of Zylon, were cut from a 508-mm by 91.4 m (20-in. by 300-ft) roll. The 330- by 330-mm (13- by 13-in.) plies of Kevlar were cut from a 308-mm by 54.9-m (1-ft by 180-ft) roll, while the 330- by 330-mm (13- by 13-in.) plies of Kevlar were cut from a 1.1 m by 6.7-m (3.6 ft by 22 ft) roll.

2.1.6 Target Holder.

The target holder has outside dimensions of 350 by 350 mm (14 by 14 in.) and is 12.7 mm (0.5 in.) thick. It has a 254- by 254-mm (10- by 10-in.) centrally located window and uses a hexagonal tongue and groove clamping configuration to secure the fabric tightly, as shown in figures 19 through 21. Each side of the target holder has a mating clamping edge, as shown in figure 22, and fits nine equally spaced 9.5-mm (3/8-in.) grade 8 nuts and bolts. The target holder also accommodates four- or eight-peg configurations with equally spaced 9.5-mm (3/8-in.) holes, where the pegs are positioned around the 254- by 254-mm (10- by 10-in.) window. The torque limit for each bolt was 67.8 N-m (600 lb-in.). Aluminum spacers, 254 mm (10 in.) by 9.5 mm (3/8 in.) by 3.2 mm (1/8 in.), were used to ensure even clamping of the fabric inside the target holder.

2.1.7 Target Mount.

The cast iron target mount was securely attached to the powder gun table by four 9.5-mm (3/8-in.) bolts, as shown in figure 23. The vertical surface portion of the target mount, where the target holder was placed against, was located 136 cm (53.5 in.) from the powder gun muzzle. The target holder was fixed against the target mount by four heavy-duty C-clamps that were installed at the four corners of the target holder, as shown in figure 24.

2.1.8 Blast Shield.

A blast shield was mounted 220 mm (8.7 in.) in front of the muzzle of the powder gun (figure 25). The blast shield was made of 1.6-mm (1/16-in.)-thick sheet metal, which was attached to an aluminum stand. A 40-mm- (1.6-in.)-diameter hole was cut from the sheet metal for projectile passage. The aluminum stand was bolted to the powder gun table by two 6.35-mm (1/4-in.) bolts. Although some blast gases were not contained, the blast shield was installed to minimize firing debris from interfering or damaging the velocity measurement instruments.

2.1.9 Catcher Box.

A 508- by 508- by 508-mm (20- by 20- by 20-in.) cast iron box, lined with 25.4-mm- (1-in.)-thick wood, was placed in the firing path of the powder gun. The box was filled with old clothing, newspaper, and foam, as shown in figure 26. The catcher box was used to recover fired projectiles and prevent permanent damage to the projectile so they could be reused.

2.2 TEST PROCEDURES.

The following sections describe the test procedures for each of the four test configurations used in this experimental investigation.

2.2.1 Four-Clamp Configuration.

Using custom serrated scissors, the fabric was cut into 330- by 330-mm (13- by 13-in.) squares from the bulk fabric roll. The longitudinal dimension of the fabric was noted to ensure proper alignment in the target holder. The fabric was placed flat on top of the target holder so that the hexagonal groove was in contact with the fabric. The fabric was adjusted until properly aligned, with the edges of the fabric parallel to the target holder. A hexagonal rod was pressed into its respective groove on the target holder, causing the fabric to conform to the groove. The fabric was then folded around and over the hexagonal bar, leaving the nine through-holes exposed. The clamping edge, which had a mating hexagonal groove pattern, was placed on top of the fabric and aligned with the nine holes. With the target fabric locked between the target holder and the clamping edge, nine 9.5-mm (3/8-in.) grade 8 bolts and nuts and eighteen washers were inserted into the fixture, as shown in figure 27. An aluminum spacer was inserted at the bottom part of the clamping edge to ensure the tightening of the bolts would result in an even tightening of the clamping edge surface onto the target holder and fabric. Without the aluminum spacer, the clamping edge would be lopsided when tightened. With the bolts in place, nuts and washers are screwed in, but not yet tightened. After the first clamping edge was installed, the fabric was pulled tautly by hand into the target holder. In similar fashion as the first clamping edge installation, the opposite side of the first clamping edge was installed with the same fastening process. After the second clamping edge was installed, the serrated scissors were used to cut away a 38.1- by 38.1-mm (1.5- by 1.5-in.) square from the corners of the fabric. The fabric was cut at the corners to prevent fabric overlap which would obstruct the tightening of the clamping edges to the target holder. After all four clamps were in place, a torque wrench was used to tighten the bolts to their maximum torque rating of 67.8 N-m (600 lb-in.). Similar to tightening a car wheel, opposite sides were tightened to ensure distributed loading. Figures 28 through 30 show all four clamping edges installed on the target holder.

2.2.2 Two-Clamp Configuration.

This configuration installs two opposing clamp edges, as shown in figure 31. Two opposite sides of the target holder would be installed with clamping edges, while the other two opposing sides of the target holder are not fastened.

2.2.3 Four-Peg Configuration.

Similar to the four-clamp configuration, serrated scissors were used to cut the target fabric into 508- by 508-mm (20- by 20-in.) squares from the bulk fabric roll. The target holder was placed on top of the fabric and positioned so that the center of the target holder was aligned with the center of the fabric. The edges of the target holder were adjusted until they were parallel to the fabric edges. A black permanent marker was used to mark the positions of the four corner through-holes on the target fabric. The special arrowhead cutter, provided by SRI (figure 32), was used to cut the fabric at the four marked locations in the form of an “X”. Four 9.5-mm (3/8-in.) grade 8 bolts and nuts with eight 50.8-mm (2-in.) fender washers inserted into each hole and used to attach the fabric to the target holder. The nuts and bolts were hand-tightened so that the target fabric was pressed against the target holder in a loose manner. Figures 33 and 34 show the four-peg configuration.

2.2.4 Eight-Peg Configuration.

The eight-peg configuration followed the same procedure as the four-peg configuration, except an additional hole was created at the midpoint of each of the four sides and the fabric was placed over the corresponding holes (figure 35). The arrowhead cutter was used to make cuts at the eight marked locations on the fabric.

2.3 TEST SETUP.

With the fabric in place, a black permanent marker was used to pinpoint the shot location (center, diagonal, or midway) and outline the impact-side boundary of the fabric. A center shot strikes at the center of the target holder window. A diagonal shot strikes at the halfway point from the center to the corner of the target holder window. A midway shot strikes at the halfway point from the center to the perpendicular target boundary. The target holder was attached to the target mount using four C-clamps at the four corners of the target holder. The high-intensity lamps (650 W) were turned on to illuminate the front and back areas of the target. By looking down the barrel of the powder gun, adjustments were made to align the shot location with the center of the barrel. The four C-clamps were hand-tightened so that the load was distributed evenly. The velocity instruments were turned on and paper grids were installed. Each velocity instrument was examined to ensure proper function; the helium-neon gas laser beams were tested by waving a steel rod past the two laser beams. The initial and final paper grid setups were tested by touching a right circular cylindrical projectile against the respective grids. The camera was set to 10000 frames per second with a shutter speed of 1/20000 sec. As long as the camera's field of view was in its proper location, no camera position adjustments were necessary. Using a scale, a measured amount of 3031 smokeless gun powder, corresponding to the desired initial projectile velocity, was weighed and then loaded into an empty cartridge. A 76.2-mm (3-in.) by 152.4-mm (6-in.) tissue was crumpled and stuffed into the loaded 0.50 caliber cartridge to pack down the 3031 smokeless powder. A projectile was inserted into the 0.50 caliber cartridge and the unit was placed into a bracket in the breech of the powder gun. The breech was closed and tapped closed with a rubber mallet, engaging the interlocking mechanism of the breech. The electrical triggering line leading to the firing button was connected to the breech of the gun, and the camera was moved to a small porthole next to the ballistics laboratory door. The camera was triggered by hand, outside the ballistics laboratory, just before shooting the powder gun.

With the complete system in its ready condition, the personnel evacuated the laboratory, and the door was closed. The camera recording trigger switch was pressed, and then the firing switch (figure 36) was pressed. Immediately after the shot (~1 second), the camera-recording trigger switch was depressed to end the recording. After firing, the recorded time intervals from the velocity measurement equipment were recorded and used to calculate the initial and final velocities. The digital video footage was uploaded to the laptop computer. The digital video was used to calculate the initial and final velocities and was analyzed to determine projectile orientation and fabric deformation. The fabric and paper grids were visually inspected. The right circular cylindrical projectile was retrieved from the catcher box and the C-clamps were loosened so the target holder could be removed for examination. The shot location, fabric perforation, slip, or tear out was measured and recorded. The 0.50 caliber cartridge was removed from the breech of the powder gun. The nuts and bolts were removed from the target holder, and

the fabric was removed from the holder. Before storing the tested samples, the fabric was examined for tears along the edge boundaries or pegs and recorded.

3. RESULTS AND DISCUSSION.

Results for the following tests are discussed in sections 3.2 through 3.10.

- Four clamp/Center shot/Zylon/Kevlar (All four sides of fabric clamped)
- Two clamp/Center shot/Zylon/Kevlar (Two opposite sides of fabric clamped)
- Four-peg/Center shot/Zylon/Kevlar
- Eight-peg/Center shot/Zylon
- Two clamp/Diagonal shot/Zylon
- Two clamp/Midway shot/Zylon
- Four-peg/Diagonal shot/Zylon
- Eight-peg/Diagonal shot/Zylon
- Comparison of Nonperforation and Complete Perforation Shots

This section also discusses the accuracy of the results and the meaning of the results relative to experimental objectives. All the data sheets from this experimental investigation are included in appendix C. Appendix D contains the data reduction background and methods used in analyzing the results.

3.1 ACCURACY OF RESULTS.

In this experimental investigation, a number of factors emerged that influenced the accuracy of the results, all of which must be considered when evaluating the results. These factors were unknown at the beginning of the experimental investigation but became evident during the course of testing.

1. Clamping the target fabric to the target holder posed a dilemma. When the fabric is prepared for clamping, the operator pulls the material taut and then continues the clamping process. There is no guideline or means of measuring the amount of tension exerted on the fabric. In this study, slack in the material is a critical factor, which governs the ballistic performance. If held loosely, the target fabric will generally absorb more energy. If held extremely taut, the fabric will generally penetrate more easily and absorb less energy. Overall, any variation in the tension of the fabric in the target holder will result in a variation in the target resistance to perforation. In addition, the edge of the fabric along the target holder boundary tends to slip during impact testing. After a two- or four-clamp center or diagonal shot, a cross hair damage pattern is created on the fabric, which extends to the boundaries of the target holder. The damage pattern forms in a manner such that the cross hairs are always parallel to the boundaries of the target holder, as shown in figure 37. When the damage pattern meets the boundaries of the target holder, the black marker lines, which were initially parallel to the boundary, are no longer aligned properly, as shown in figure 38. Instead, the outer ply of the fabric seems to have slipped away from the target holder. The slip status of the other plies of fabric are undetermined, since the outer ply is the only one that can be examined without

affecting the position of the fabric in the target holder. In general, slip is difficult to quantify and define. The fabric could be plastically deforming or slipping from the target holder. Overall, the variation of slip in the fabric results in a variation of target resistance to perforations. (The maximum amount of slip is noted in the data sheets in appendix C for each test.)

2. The orientation of the projectile upon impact posed another problem. Initially, the projectile was thought to impact the fabric at normal incidence. Upon closer examination, certain cases existed where the projectile exhibited an initial yaw in the range from 1 to 22 degrees. In general, 15% of the impact tests involved yaw beyond 3 degrees. The yaw may be induced by aerodynamic effects. Since the front surface of the projectile is flat and not aerodynamically contoured like a bullet, the air flow at the front surface may have induced the yaw. Depending on the orientation of the projectile, the fabric will experience a different type of impact. If the right circular cylindrical projectile has 0 degree yaw, the entire flat front surface of the projectile strikes the fabric. Conversely, if the right circular cylindrical projectile is yawed at any angle, then the edge of the projectile will strike the fabric first. Hence, a sharper impact is experienced by the fabric, resulting in less resistance to perforations and less energy absorbed. The orientation of the projectile upon impact significantly influences the ballistic resistance of the fabric.
3. The precision of the velocity measurement instrumentation posed a problem concerning the validity of the data. During the tests, numerous initial and residual velocity measurements were made, but the velocity instrumentation did not give consistent readouts. During one test, a comparison of the measured velocities would result in a difference of ± 1 m/s (3.28 ft/sec). In other cases, the measured velocities would vary by ± 15 m/s (49.21 ft/sec). Despite system calibration tests and meticulous test setup control, a random variation in these measurements continued to exist throughout the study. Upon examination of the results, the maximum percentage in variation of the velocity measurements was calculated to be $\pm 10\%$. This particular variation then translates to a $\pm 19\%$ variation in the impact and absorbed energy. The imprecision of the velocity measurement instrumentation causes scatter in the data. As a result, the conclusions derived from this experimental investigation are meant to be used as an initial screening of the ballistic performance of Zylon and Kevlar fabrics. Further experimentation is needed to more accurately characterize the ballistic behavior of these two fabrics and to provide a better understanding of the process. Due to time constraints, only a limited amount of data was acquired.
4. Variation existed between the desired initial velocity and initial velocity generated in a number of tests. The initial velocity of the projectile depends significantly on the way the tissue is tamped into the 0.50 caliber cartridge. Hence, it was not possible to exactly obtain the desired initial velocities and, difficult to obtain data for specific velocity ranges.

3.2 FOUR-CLAMP CONFIGURATION/CENTER SHOT/ZYLON/KEVLAR.

Figure 39 shows that the perforation limit velocity for Zylon is similar to Kevlar, ranging from 110-115 m/s (360-377 ft/sec) for six plies of fabric. In test 14B, eight plies of fabric were used instead of the designated six plies, which accounts for the higher perforation limit velocity and resistance to impact without perforation. (Tests 10B, 11B, and 16B use two, four, and four plies respectively.) The data show an increasing linear trend, where the residual velocity increases as the initial velocity increases beyond the perforation limit. According to the initial versus residual velocity plot, Zylon and Kevlar behave similarly.

Figure 40 shows the curves of the impact and residual energy per ply for both Zylon and Kevlar. For Zylon, 100% energy absorption occurred at 58 J/ply (test 14B). This particular point does not represent the maximum energy value. Upon inspection, only one of the eight plies of Zylon was perforated; hence, the Zylon has more plies available to absorb more energy. Even though the energy curve is calculated on a per ply basis, tests 10B (two plies), 11B (four plies), 14B (eight plies), and 16B (four plies) cannot be used as credible data points due to the interaction effect of having a different number of plies that may contribute to a different absorbed energy behavior. Further testing is needed to determine if a per ply basis is a valid means of analyzing the ballistic performance.

Slightly beyond 58 J/ply, complete perforation occurred at ~62-63 J/ply (test 22B). Figure 40 shows that the maximum energy absorbed by Zylon in the four-clamp configuration lies in the range of ~55-60 J/ply. It should be noted that tests 15B and 21B exhibit a lower-energy absorption limit. By extrapolation, these three tests convey 100% energy absorption at 47 J/ply, which is an 11 J/ply reduction from the originally determined limit.

Kevlar possesses a lower energy absorption limit compared to Zylon, as shown in figure 40. For Kevlar, the largest value for 100% energy absorption occurred at 41 J/ply (test 37B). Similar to the Zylon argument, this particular value does not represent the maximum energy value due to incomplete perforation. Slightly beyond 41 J/ply, complete perforation occurred at ~48 J/ply (test 35B). More tests need to be performed to pinpoint the upper and lower energy absorption limit of Kevlar in the four-clamp configuration.

Zylon has a higher energy absorption range than Kevlar. Near 100% absorption energies, Zylon absorbs ~45-63 J/ply, while Kevlar absorbs ~32-45 J/ply. Beyond 25% energy absorption, the Zylon tapered to the ~45-52 J/ply range (~13% reduction), while Kevlar remained in the ~32-45 J/ply range. In general, the performance of Zylon fabric in these tests was marginally (~27%) better than the performance of equal areal density Kevlar fabric against the same right circular cylindrical projectile. In the nonperforation range, the Zylon was able to absorb more energy than Kevlar. In the complete perforation range, the Zylon absorbed only slightly more energy than Kevlar.

Using the derivation for force deflection, given in appendix E, the approximate force imposed on a single yarn of the fabric during a nonperforation shot was calculated to be 3276 N. This value was derived using a modulus of 180 GPa for Zylon, a deflection of 12.7 mm (0.5 in. ~typical for nonperforating shots), a length of 25.4 cm (10 in.), and a cross-sectional area of 3.65 mm² (5.6575E-5 in.²) [5]. This particular force value is only a rough approximation for a yarn of fiber

undergoing deflection, and does not represent the force to deflect the entire fabric in the target holder used in this study.

3.3 TWO-CLAMP CONFIGURATION/CENTER SHOT/ZYLON/KEVLAR.

For six plies of fabric, the perforation limit velocity for Zylon is slightly higher than Kevlar (19 m/s difference), as shown in figure 41. In test 84E, the Zylon fabric stopped the right circular cylindrical projectile, which was traveling at 145 m/s (475 ft/sec). As previously mentioned, this velocity value does not represent the perforation limit velocity due to incomplete perforation. In test 82E, all six plies of Kevlar were partially perforated and stopped the projectile, which was traveling at 126 m/s (413 ft/sec). Hence, the perforation limit velocity to ensure no residual velocity is 126 m/s (413 ft/sec) for Kevlar. In the two-clamp configuration, the initial and residual velocity curves of Zylon and Kevlar are comparable.

In addition, the two-clamp configuration has higher perforation limit velocities for both Zylon and Kevlar than the four-clamp configuration. The four-clamp configuration had a velocity range of 110-115 m/s (360-377 ft/sec), while the two-clamp configuration had a velocity range of 126-145 m/s (413-475 ft/sec). In these two configurations, the two-clamp setup was able to deflect more due to the lack of two additional boundary constraints, which permitted more impact energy to be absorbed.

In figure 42, the highest 100% energy absorption point for Zylon occurred at 65 J/ply (test 84E). (More results are needed to identify the limit 100% energy absorption.) The highest 100% energy absorption point for Kevlar occurred at 49 J/ply (test 82E). Compared to the four-clamp energy curve, the two-clamp configuration absorbed a marginally higher amount of energy (~58 versus 65 J/ply). Similarly, Kevlar seemed to exhibit a higher energy absorption in the two-clamp configuration than the four-clamp configuration (~41 versus 49 J/ply). However, this phenomenon may be due to the fact that complete perforation occurred in test 82E, which accounts for the additional absorbed energy. In general, Zylon possesses a higher energy absorption threshold than Kevlar.

Interestingly, the ballistic behavior of the Kevlar near the 100% energy absorption level behaved in an unexpected manner (test 59E). By increasing the impact energy slightly, the absorbed energy increased slightly. Ideally, the absorbed energy should stay constant or below the 100% absorbed energy limit. Most likely, system variability was the reason for the energy discrepancy.

In addition, Zylon had a higher energy absorption band than Kevlar. Beyond 25% energy absorption, the Zylon lies in the ~50-60 J/ply band, while Kevlar remained in the ~40-50 J/ply range. Relative to the four-clamp configuration, the two-clamp configuration exhibited marginally (~8%) higher Zylon and Kevlar energy absorption bands in the complete perforation region. The ballistic performance of Zylon fabric improved when the two-clamp configuration was used compared to the four-clamp energy curves.

3.4 FOUR-PEG CONFIGURATION/CENTER SHOT/ZYLON/KEVLAR.

In figure 43, the perforation limit velocity for Zylon and Kevlar is difficult to determine due to the lack of data points near the zero residual velocity range. By examining the general trend,

both Zylon and Kevlar began perforation in the initial velocity range of 190-225 m/s (623-738 ft/sec). Test 91P indicated that an initial velocity of 223 m/s (731 ft/sec) stopped the projectile.

The most significant factor that governed the impact and absorbed energy behavior was the rip at the pegs. As the amount of rip at the pegs increased, the amount of absorbed energy also increased. In figure 44, both tests 91P and 95P correspond to 100% absorbed energy. Besides the different initial velocities (223 and 175 m/s (731 and 575 ft/sec), respectively), each test had a different amount of maximum rip at the corners (199 and 12.7 mm (0.75 and 0.5 in.)). In these particular tests, identifying the exact energy level at which a four-peg configuration will absorb the impact energy of a projectile was a difficult process. Not only did the velocity need to be controlled, but the amount of rip at the corners also needed to be controlled. Overall, the initial velocity and rip interaction complicated the matter of characterizing the ballistic performance of Zylon and Kevlar in the four-peg configuration.

In test 110P, the projectile perforated all four plies but did not completely pass through. Hence, the amount of absorbed energy (124 J/ply) was the upper limit for energy absorbed for the special case where the maximum rip at the pegs was 12.7 mm (0.5 in.). Interestingly, test 111P had the same maximum rip as test 110P, but the ballistic performance was unexpected. In this case, the absorbed energy increased to 172 J/ply as the impact energy increased. Ideally, the amount of absorbed energy should be equal to or less than the upper limit of 124 J/ply of absorbed energy. Upon inspection, test 110P had an 8 degree yaw as opposed to test 111P, which had a 0 degree yaw. In general, the yaw may have caused the projectile to penetrate more easily, resulting in a lower measured absorbed energy per ply.

In general, the four-peg impact tests revealed a high level of 100% energy absorption compared to the four- and two-clamp configurations (approximately three times greater energy absorption). This particular trend was expected due to the large amount of slack imposed by the peg boundary conditions. Being held at the corners, the target fabric was hanging loosely when the projectile hit the target, which allowed significant deformation helping absorb the impact energy of the projectile. Instead of striking a wall of fabric, the right circular cylindrical projectile encountered a trampoline like effect (large deformation), resulting in a greater amount of energy absorbed. In addition to the trampoline effect, ripping at the corners resulted in greater energy absorption.

The difference between Zylon and Kevlar at 100% absorbed energy was difficult to distinguish. In the complete perforation region, a significant reduction in absorbed energy was apparent for both Zylon and Kevlar. For Zylon, the absorbed energy declined from the ~142-230 J/ply (100% energy absorption) range to ~40-100 J/ply (25% energy absorption) range.

Similarly, the Kevlar also experienced a loss in absorbed energy. Ignoring the scatter, the fabrics exhibited a significant loss in absorbed energy per ply as the impact energies increased. In general, this phenomenon might be explained by the different mechanisms by which energy is absorbed. In the four-clamp configuration, a small area of the fabric absorbed the majority of the impact energy. In other words, the impact was concentrated on a small portion of the fabric, representing the projected impact area. The surrounding fabric does not absorb much of the impact.

In the two-clamp configuration, the fabric was allowed to deflect more, so the majority of the impact energy was distributed to a larger portion of the fabric compared to the four-clamp configuration. Instead of being concentrated, the impact energy of the projectile was dissipated over a larger area of the fabric. In the four-peg configuration, the fabric was allowed to deflect significantly ~187 mm (~7 in.) so that the majority of the impact energy was distributed over the entire fabric. In addition, the ripping at the corner pegs absorbed substantially more energy. Interestingly, when the impact energies significantly increased (beyond 25% energy absorption), the ripping at the corner pegs was negligible. When the projectile was stopped, the maximum rip was ~19 mm (~0.75 in.) (test 91P). However, when the projectile completely perforated, the fabric rip was almost zero (test 93P). When the impact energy was large enough to result in complete perforation, the impact energy of the projectile was not dissipated by the ripping at the corner pegs.

In summary, the apparent loss of absorbed energy with increasing impact energies was a direct result of the amount of rip at the corner pegs. During nonperforation, the ripping at the pegs absorbed the majority of the impact energy. During complete perforation, the deflection of the fabric absorbed a small portion of the impact energy, while the fabric fibers absorbed a large portion of the impact energy. Instead of energy absorption at the corner pegs, this consumption occurred at the fabric level.

3.5 EIGHT-PEG CONFIGURATION/CENTER SHOT/ZYLON.

In figure 45, test 98P closely represents the perforation limit velocity. The maximum rip at the corner was 25.4 mm (1 in.) and three of the four plies were perforated at a velocity of 210 m/s (689 ft/sec). In general, the perforation limit velocity for the eight-peg configuration was comparable to the four-peg configuration. However, no comparison can be made with respect to the four and two clamp velocity curves, because of the difference in plies (six and four plies, respectively) used during the impact tests.

As shown in figure 46, the upper limit of 100% absorbed energy was 204 J/ply (test 98P). This particular point does not represent the maximum energy value due to incomplete perforation of all four plies. In general, the four-peg energy curve was marginally better than the eight-peg configuration. Since the fabric was held loosely in the target holder, it was allowed to deform significantly upon projectile impact. However, the fabric did not have as much slack in the eight-peg configuration due to the additional bolts along the edge that constrained the amount of deformation. In test 91P (four pegs), Zylon absorbed 230 J/ply with a maximum rip of 19.1 mm (0.75 in.) In test 98P (eight pegs), Zylon absorbed 204 J/ply with a maximum rip of 25.4 mm (1 in.) Hence, test 91P should have been able to absorb more energy for the same amount of maximum rip from the corner pegs. From the data, the four-peg configuration performed better than the eight-peg configuration during the impact tests.

Similar to the four-peg energy curve, an apparent drop in absorbed energy was observed. Unlike the four-peg energy curve, the eight-peg energy curve in the complete perforation region exhibited a more narrow range of ~38-64 J/ply. However, the rip at the corners was not negligible as in the four-peg case. In general, the fabric deformation and rip at the corners were the two mechanisms absorbing the majority of the impact energy. The ballistic behavior closely

mimics the two- and four-clamp trends, where the absorbed energy band lies in the 45-60 J/ply range.

3.6 FOUR-CLAMP CONFIGURATION/DIAGONAL SHOT/ZYLON.

Figures 39 and 47 show that the initial and residual velocity curves are comparable. Despite the different shot locations, no significant differences exist between the two velocity curves for Zylon. The perforation limit velocity range also seems to be similar (~100 m/s (328 ft/sec)). Although figure 47 lacks data points in the 0 residual velocity range, an extrapolation can be devised from the complete perforation results.

By shooting at the corner of the four-clamp configuration, the Zylon was not be able to deflect as much as when struck at the center. As a result, less energy was absorbed at the corner. Using the trampoline analogy, a diagonal shot on the Zylon fabric will not produce as much deflection as a center shot due to boundary constraints. As a result of smaller deflection, less energy will be absorbed during a diagonal shot, all other conditions being the same. Using the complete perforation results, an energy absorption band, in the range of ~30-50 J/ply, can be interpolated. (See figure 48.)

Both the center and corner results for the four-clamp configuration were plotted, as shown in figure 49. In general, the center shot results exhibit a marginally better ballistic performance than the diagonal shot.

3.7 TWO-CLAMP CONFIGURATION/MIDWAY SHOT/ZYLON.

Figures 41 and 50 show the initial versus residual velocity curves for both two-clamp center and diagonal shots are similar. Both velocity curves share the same increasing linear trend. Despite the different shot locations, no significant differences exist between the two velocity curves for Zylon. In figure 50, the perforation limit velocity can be interpolated from the trend, which is in the range of ~140-150 m/s (459-492 ft/sec).

Test 118E exhibited an unexpected behavior. Relative to test 119E, test 118E had a lower initial velocity and higher residual velocity. This particular point needs to be retested to verify behavior.

The upper limit on the 100% energy absorption line occurred at approximately 64 J/ply (test 115E), as shown in figure 51. Although this test resulted in complete perforation, the projectile was nearly stopped (residual velocity~14 m/s (46 ft/sec)). Relative to the two-clamp center shots, the 100% energy absorption range was comparable. Hence, the shot location (center versus midway) did not appear to have a significant effect on the impact versus absorbed energy curves.

Interestingly, the diagonal shot results exhibit a marginally better ballistic performance than the center shot results. In the complete perforation region, the energy absorption band lies consistently between 70-80 J/ply. This was slightly better than the two-clamp center shot, which lies in the 50-60 J/ply band. This particular result was counter-intuitive; if the Zylon's degree of deflection was restricted, less impact energy should be absorbed. Ideally, the midway shot

should absorb less energy than the center shot due to less deflection near the target holder boundary. Relative to the four-clamp configuration, the two-clamp configuration seems to have a slightly higher energy absorption band, which was in the range of 50-80 J/ply. (See figure 52.)

3.8 FOUR-PEG CONFIGURATION/DIAGONAL SHOT/ZYLON.

At 204 m/s (700 ft/sec), three of the four plies of fabric were perforated in test 129PC, as shown in figure 53. Hence, the perforation limit velocity was slightly higher than 204 m/s (700 ft/sec). Upon comparison, the four-peg center and diagonal shot velocity curves were similar. Hence, the shot location does not seem to greatly affect the velocity curves.

In figure 54, the highest 100% energy absorption point for Zylon occurred at 192 J/ply (test 129PC). In comparison with the four-peg center shot energy curve, the four-peg diagonal shot energy curve was somewhat lower (~192 versus 223 J/ply). This discrepancy may be due to the uneven rip at the corner pegs. Test 91P had an evenly distributed rip of 19.1 mm (0.75 in.) at the pegs due to the symmetry of the fabric. In this case, test 129PC had unsymmetrical ripping; the peg closest to the point of impact experiences the largest amount of rip. Unlike test 91P, test 129PC had a maximum rip of 33.4 mm (1.313 in.) and a minimum rip of 2 mm (0.0625 in.). In general, the Zylon's uneven ripping at the pegs may be the cause for the degraded ballistic performance when shot at the corner.

The ballistic behavior of Zylon was unexpected. Tests 126PC and 130PC both shared the same impact energy (204 J/ply), but different absorbed energies (202 and 224 J/ply, respectively) and different amounts of maximum rip (15.8 and 25.4 mm (0.625 and 1 in.), respectively). Overall, the intrinsic behavior of Zylon to rip caused variability in the amount of energy absorbed.

As shown in figure 55, a loss of absorbed energy was apparent in the complete perforation region of the four-peg diagonal shot configuration, which was similar to the four-peg center shot configuration. Beyond 25% energy absorption, test 132P exhibits an absorbed energy of 92 J/ply.

The approximate energy imposed on the fabric ripping at the corner was calculated to be 1032 J. This value was derived by multiplying the ultimate tensile strength by the cross-sectional area of four plies and the amount of ripping. An ultimate tensile strength of 5.6 GPa was used for Zylon, along with a cross-sectional area of 7.26 mm^2 (0.0113 in.^2) and a rip length of 25.4 mm (1 in.). This particular energy value was only a rough approximation for ripping at the corner.

3.9 EIGHT-PEG CONFIGURATION/DIAGONAL SHOT/ZYLON.

The right circular cylindrical projectile was stopped at 210 m/s (689 ft/sec) (test 139P), as shown in figure 56. All four plies of fabric were partially perforated, but they were able to stop the projectile. Upon comparison, the eight-peg center and diagonal perforation velocities are identical. The perforation limit velocity was similar regardless of shot location.

In figure 57, the maximum 100% energy absorption point for Zylon was 204 J/ply (test 139P). In test 139P, all four plies of Zylon were perforated, but the projectile did not pass through. Similar to the four-peg configuration, the eight-peg center and corner ballistic performance near

the 100% energy absorption region was comparable. The only difference was the amount of rip at the corner pegs. In the center shot case, a maximum rip of 25.4 mm (1 in.) resulted in 204 J/ply of absorbed energy. In the diagonal shot case, a maximum rip of 28.6 mm (1.125 in.) resulted in 204 J/ply of absorbed energy. Relative to the eight-peg diagonal shot, the eight-peg center shot configuration generally permits greater energy absorption for the least amount of rip from the pegs.

Similar to the eight-peg center shot configuration, a loss of absorbed energy is shown in figure 58 beyond the 25% energy absorption region. Tests 141P, 142P, and 143P exhibit absorbed energies in the range of 62-80 J/ply. The rip at the corner closest to the point of impact was comparable to the rip at the corner pegs for a center shot. For comparison, figure 59 compares impact versus absorbed energy for all diagonal shots.

3.10 COMPARISON OF NONPERFORATION AND COMPLETE PERFORATION SHOTS.

The objective of this investigation was to determine if Zylon possessed better ballistic performance than Kevlar. From figures 40, 42, 44, and 60, Zylon appears to be marginally better than Kevlar under the four-clamp (~27%), two-clamp (~27%), and four-peg (~33%) configurations. In general, Zylon appears to be a potential candidate for aircraft-shielding applications. Although Zylon's ballistic performance was only slightly better than Kevlar, it was lighter than Kevlar. If Zylon is used, there will be two benefits: (1) improved fragment barrier protection and (2) structural weight savings.

To absorb the greatest amount of energy without complete perforation, the four-peg or eight-peg configuration should be considered as potential fragment barrier boundaries due to the large degree of energy absorption, as indicated in figures 44 and 46. Regardless of shot location, these two configurations absorb three times the amount of energy compared to the two- and four-clamp configurations.

4. CONCLUSIONS AND RECOMMENDATIONS.

This report summarizes the results of an experimental study of the effects of ballistic impact on various numbers of adjacent Zylon AS-500 Denier 35x35 weave and Kevlar KM-2-600 Denier 29x29 weave sheets. The study is part of an effort to mitigate engine rotor burst fragment in commercial aircraft using a 37 g (0.08 lb) right circular cylindrical projectile fired against a 25.4-cm (10-in.) window of fabric. This study tested four different boundary conditions: (1) four clamped edges, (2) two clamped edges, (3) four corner plies, and (4) eight pegs. In this study it was found that:

1. In the two-clamp, four-clamp, and four-peg configurations, Zylon performed marginally better than Kevlar (~27%, ~27%, and ~33%, respectively). Although a fixed percentage cannot be placed on the performance, the energy curves indicated a higher band of energy absorption for Zylon over Kevlar.
2. As shown in table 1, Zylon absorbed more energy per ply than Kevlar for nonperforating shots.

3. The two-clamp midway shot exhibited improved ballistic performance compared to the two-clamp center shots.
4. In three of the four test configurations, shot location (center, midway, and diagonal) did not significantly affect the ballistic performance of Zylon. In the four-clamp configuration, a center shot exhibited marginally better performance than a diagonal shot.
5. For nonperforating shots, both the four-peg and eight-peg configurations absorbed the greatest amount of impact energy. The ripping at the pegs was an important factor, which governed the amount of energy absorbed by the fabric.
6. For perforating shots, the four-peg and eight-peg configurations experienced a drastic loss in absorbed energy as the impact energies increase; the amount of rip at the pegs decreased as the impact energy was increased.
7. For aircraft-shielding applications, high-strength fabrics are a potential candidate for lightweight fragment barrier use. The four-peg configuration should be examined further as the best candidate.
8. For future ballistic testing, the slip and yaw of the projectile should be carefully controlled to ensure consistent results. A better target holder was needed to control the tautness of the fabric and to improve control of fabric slippage at the boundaries.
9. New velocity measurement techniques need to be developed to ensure consistent and precise measurements. A more robust velocity measurement systems must be built, which was insensitive to any changes in the environment. A digital video camera lens with a larger field of view would more precisely determine the velocities.

5. REFERENCES.

1. Toyobo, PBO Fiber Zylon, Report of the Toyobo Corporation, LTD, www.toyobo.co.jp, 2001.
2. D.A. Shockey, D.C. Erlich, and J.W. Simmons, “ Lightweight Fragment Barriers for Commercial Aircraft,” *18th International Symposium on Ballistics*, v. 2, 1999, pp. 1192-1199.
3. D.A. Shockey, D.C. Erlich, and J.W. Simmons, “Improved Barriers to Turbine Engine Fragments: Interim Report III,” FAA report DOT/FAA/AR-99/8,III, May 2001.
4. D.A. Shockey, D.C. Erlich, and J.W. Simmons, “ Full-Scale Tests of Lightweight Fragment Barriers on Commercial Aircraft,” FAA report DOT/FAA/AR-99/71, November 1999.
5. D.A. Shockey, D.C. Erlich, and J.W. Simmons, “Improved Barriers to Turbine Engine Fragments: Interim Report IV,” FAA report DOT/FAA/AR-99/8,IV, June 2002.

6. D.A. Shockey, D.C. Erlich, and J.W. Simmons, "Improved Barriers to Turbine Engine Fragments: Final Report," FAA report DOT/FAA/AR-99/8,V, June 2002.
7. D.A. Shockey, D.C. Erlich, and J.W. Simmons, "Improved Barriers to Turbine Engine Fragments: Interim Report II," FAA report DOT/FAA/AR-99/8,II, July 1999.
8. D.A. Shockey, D.C. Erlich, and J.W. Simmons, "Improved Barriers to Turbine Engine Fragments: Interim Report I," FAA report DOT/FAA/AR-99/8,I, June 1999.
9. D.A. Shockey, D.C. Erlich, and J.W. Simmons, "Finite Element Design Model for Ballistic Response of Woven Fabrics," *18th International Symposium on Ballistics*, v. 2, 2001, pp. 1415-1422.
10. E. Pineda, C. Hogue, and W. Goldsmith, "Ballistic Properties of Zylon for Application to Firearm Projectile Protection," Initial Progress Report: Army Research Laboratory Aberdeen Proving Grounds, MD, 2002.
11. E. Pineda and W. Goldsmith, "Perforation Investigations of Zylon Sheets," Final Report: Army Research Laboratory Aberdeen Proving Grounds, MD, 2002.
12. P.M. Cunniff, "The Performance of Poly (para-phenylene benzobizoxazole) (PBO) Fabric for Fragmentation Protective Body Armor," *18th International Symposium on Ballistics*, v. 2, 1999, pp. 837-844.
13. P.M. Cunniff, "A Design Tool for the Development of Fragmentation Protective Body Armor," *18th International Symposium on Ballistics*, v. 2, 1999, pp. 1295-1302.
14. P.M. Cunniff, "Dimensionless Parameters for Optimization of Textile-Based Body Armor Systems," *18th International Symposium on Ballistics*, v. 2, 1999, pp. 1303-1310.
15. P.M. Cunniff, "Assessment of Small Arms (Ball Round) Body Armor Performance," U.S. Army Soldier and Biological Chemical Command Soldier Systems Center, Natick, Natick, MA 01760-5019, 1999.
16. P.M. Cunniff, "Decoupled Response of Textile Body Armor," U.S. Army Soldier and Biological Chemical Command Soldier Systems Center, Natick, Natick, MA 01760-5019, 1999.
17. P.M. Cunniff, "Development of a Numerical Model to Characterize the Ballistic Behavior of Fabrics," U.S. Army Soldier and Biological Chemical Command Soldier Systems Center, Natick, Natick, MA 01760-5019, 1999.
18. P.M. Cunniff, "The V_{50} Performance of Body Armor Under Oblique Impact," U.S. Army Soldier and Biological Chemical Command Soldier Systems Center, Natick, Natick, MA 01760-5019, 1999.

19. P.M. Cunniff, "The Probability of Penetration of Textile-Based Body Armor," U.S. Army Soldier and Biological Chemical Command Soldier Systems Center, Natick, MA 01760-5019, 1999.
20. P.M. Cunniff and M.A. Auerbach, "High Performance M5 Fiber for Ballistics/Structural Composites," U.S. Army Soldier and Biological Chemical Command Soldier Systems Center, Natick, MA 01760-5019, 2002.
21. Bernard J. Izdebski and Lowell K. Bryant, "Right Circular Cylinder Fragments Impacting Composite Kevlar 49 Panels," Memorandum Report ARBRL-MR-03167, U.S. Army Armament Research and Development Command Ballistic Research Laboratory, April 1982.
22. C.T. Lim, V.P.W. Shim, and Y.H. Ng, "Finite-Element Modeling of the Ballistic Impact of Fabric Armor," *International Journal of Impact Engineering*, v.28, 2003, pp. 13-31.
23. J.D. Walker, "Ballistic Limit of Fabrics with Resin," Mechanical and Materials Engineering, Southwest Research Institute, P.O. Drawer 28150, San Antonio, Texas, 78228-0510, USA, 1999.
24. J.D. Walker, "Constitutive Model for Fabrics with Explicit Static Solution and Ballistic Limit," *18th International Symposium on Ballistics*, v.2, 1231-1238, 1999.
25. T.I. Zohdi, "Modeling and Simulation of Progressive Penetration of Multilayered Ballistic Fabric Shielding," *Computational Mechanics*, 29, 2002, pp. 61-67.



FIGURE 1. A DC-10 AIRCRAFT
(The same type of aircraft involved in the Sioux City accident)

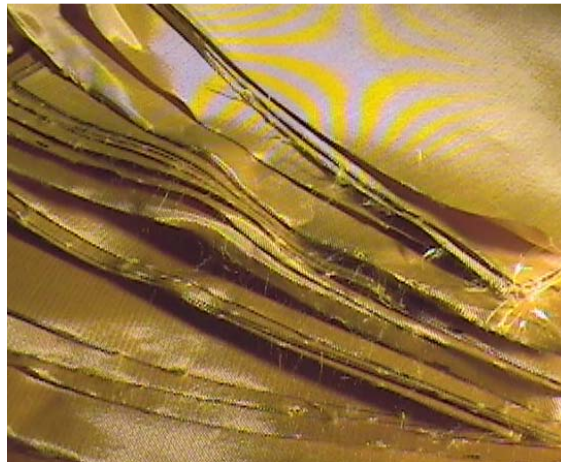


FIGURE 2. ZYLON 35x35 FABRIC USED IN THIS STUDY



FIGURE 3. EXPERIMENTAL SYSTEM IN THE BALLISTICS LABORATORY



FIGURE 4. THE POWDER GUN

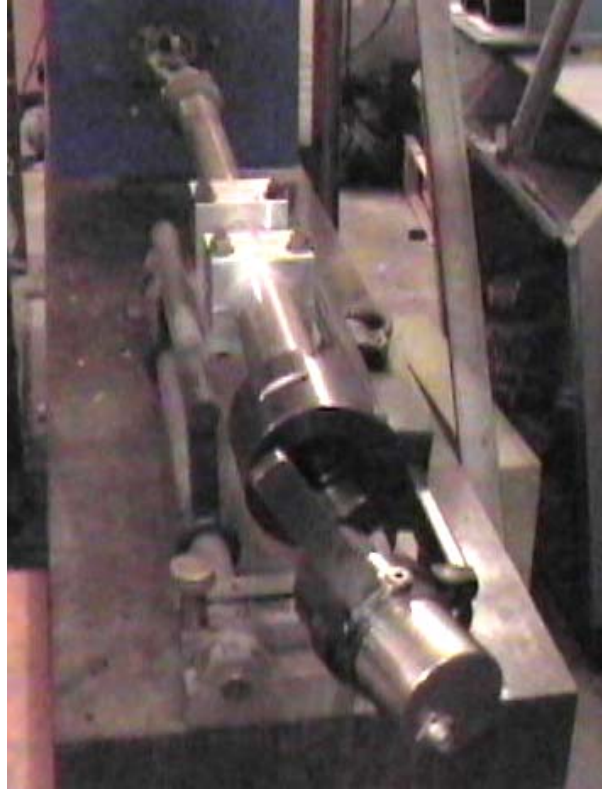


FIGURE 5. BACK VIEW OF THE POWDER GUN

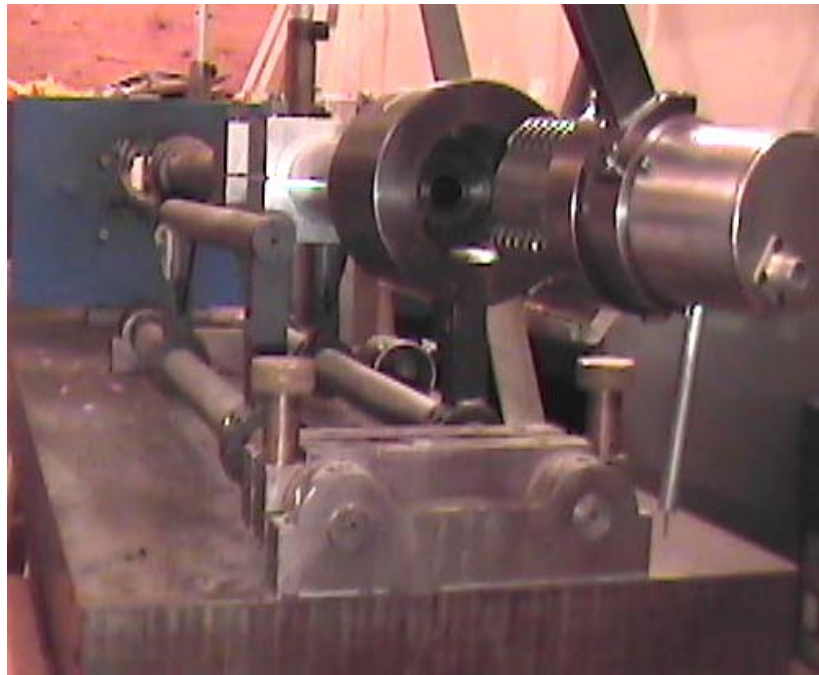


FIGURE 6. SIDE VIEW OF THE POWDER GUN



FIGURE 7. TOP VIEW OF THE POWDER GUN

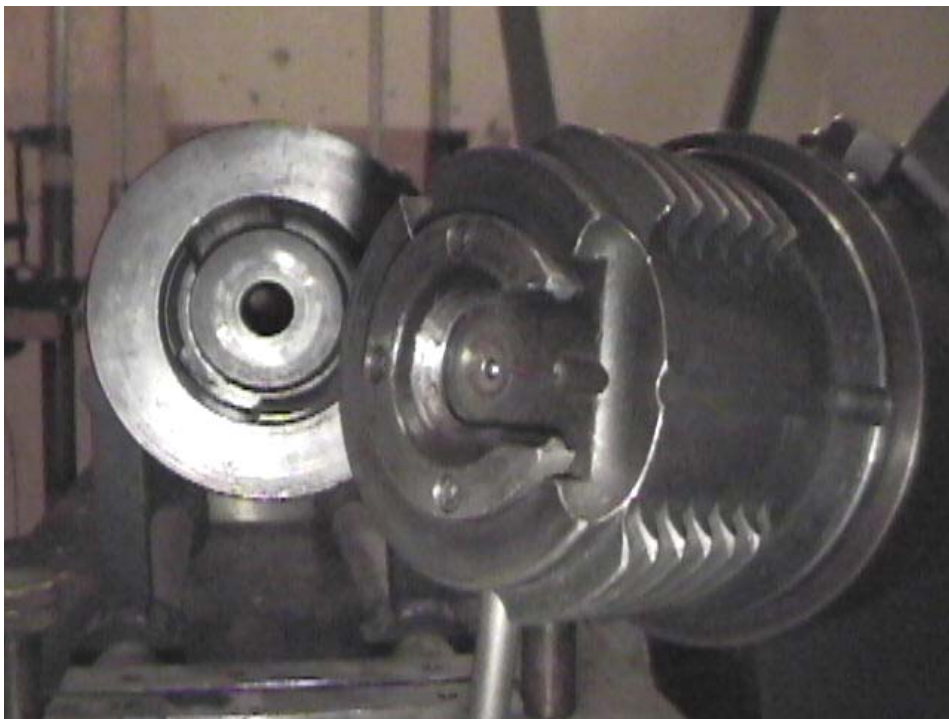


FIGURE 8. POWDER GUN BREECH



FIGURE 9. UNIPHASE HELIUM-NEON GAS LASER AND CUSTOM PHOTODIODE



FIGURE 10. PAPER GRID TARGETS WITH ALLIGATOR CLIPS ATTACHED AT THE BOTTOM



FIGURE 11. PAPER TARGETS AFTER PERFORATION



FIGURE 12. CLOSE-UP OF INTERLOCKING CONDUCTING INK LINES

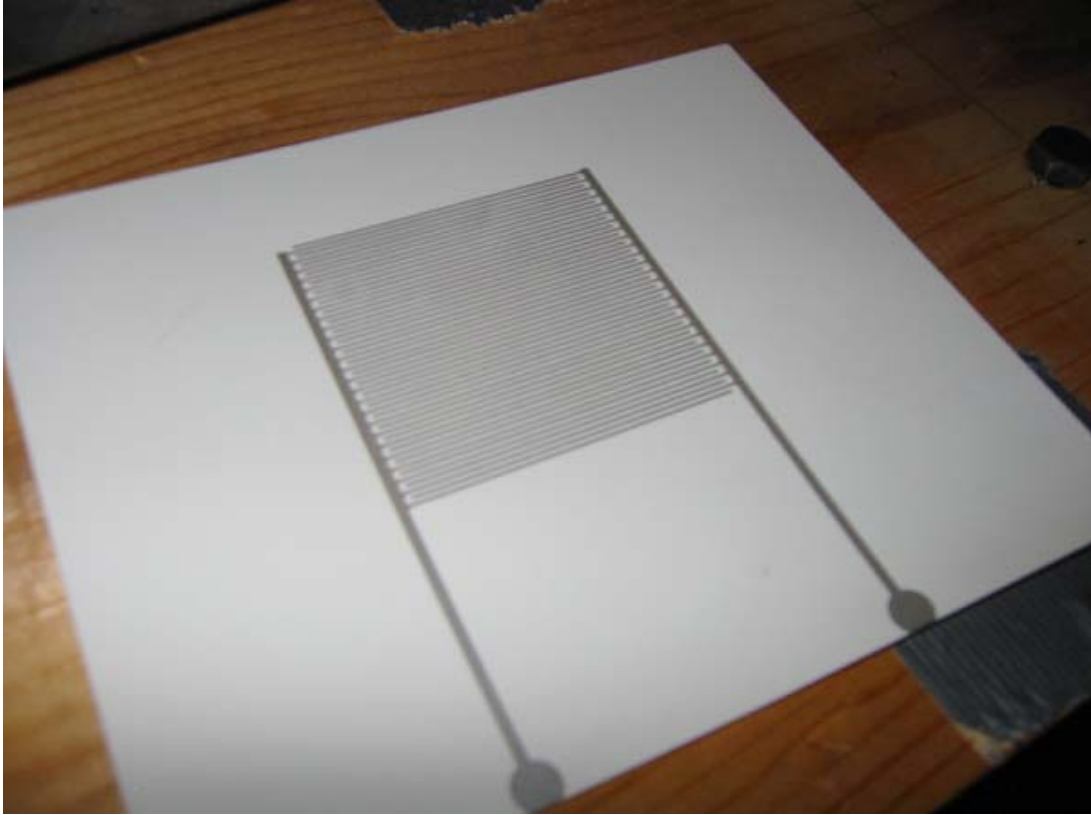


FIGURE 13. UNUSED PAPER GRID



FIGURE 14. DIGITAL VIDEO CAMERA UNIT

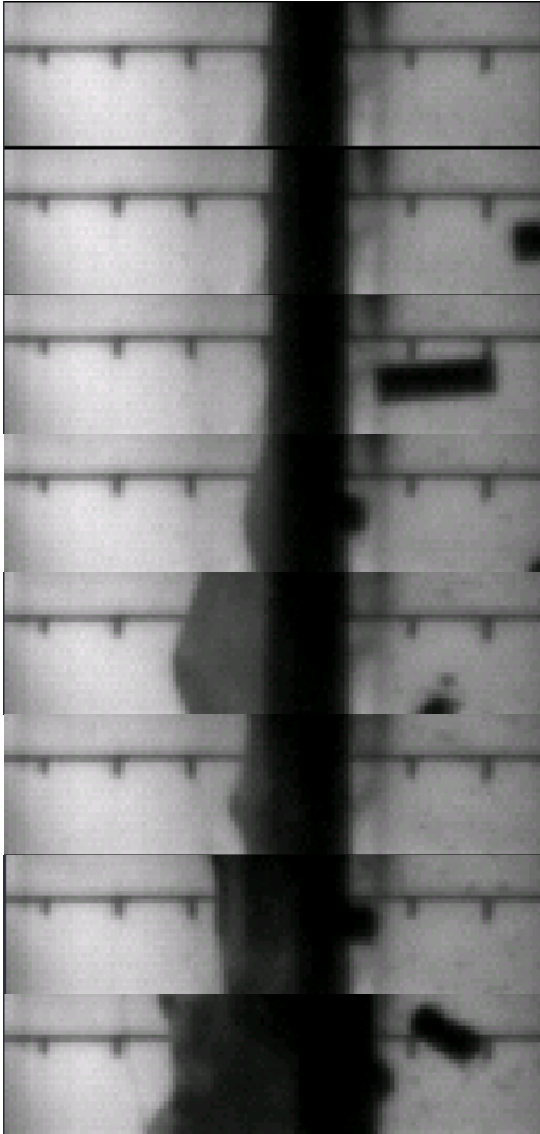


FIGURE 15. DIGITAL CAMERA
STILL OF TEST 64E
(The projectile was traveling at 79 m/s
(259 ft/sec) and no perforation
occurred on the Kevlar fabric.)

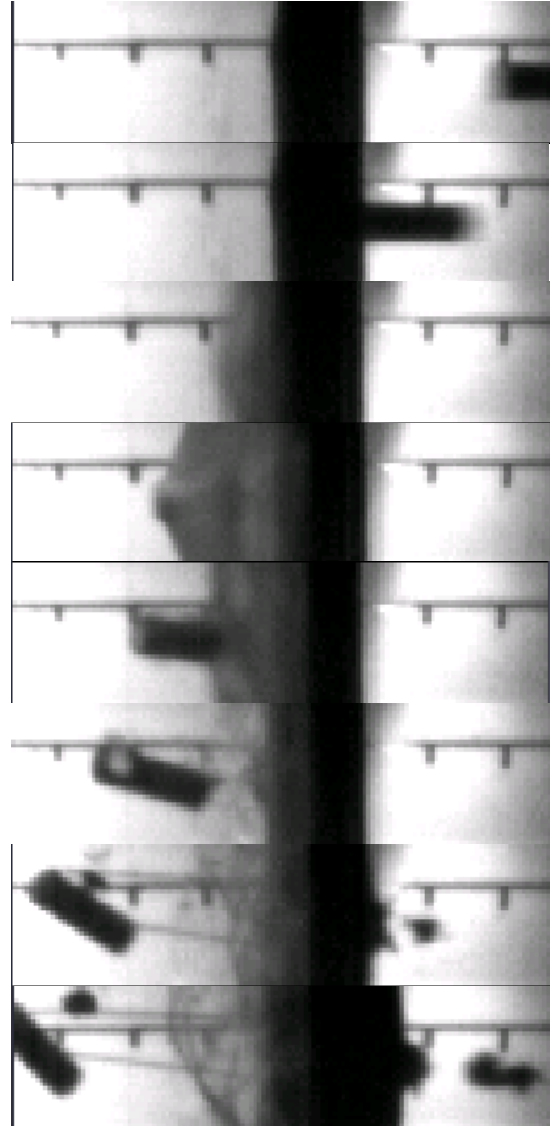


FIGURE 16. DIGITAL CAMERA
STILL OF TEST 55E
(The projectile traveled at 144 m/s
(472 ft/sec) and exited the Zylon at
30 m/s (98.4 ft/sec).)



FIGURE 17. CONTROL UNIT FOR THE DIGITAL VIDEO CAMERA



FIGURE 18. RIGHT CIRCULAR CYLINDRICAL PROJECTILE SHOWN WITH A .50 CALIBER CARTRIDGE

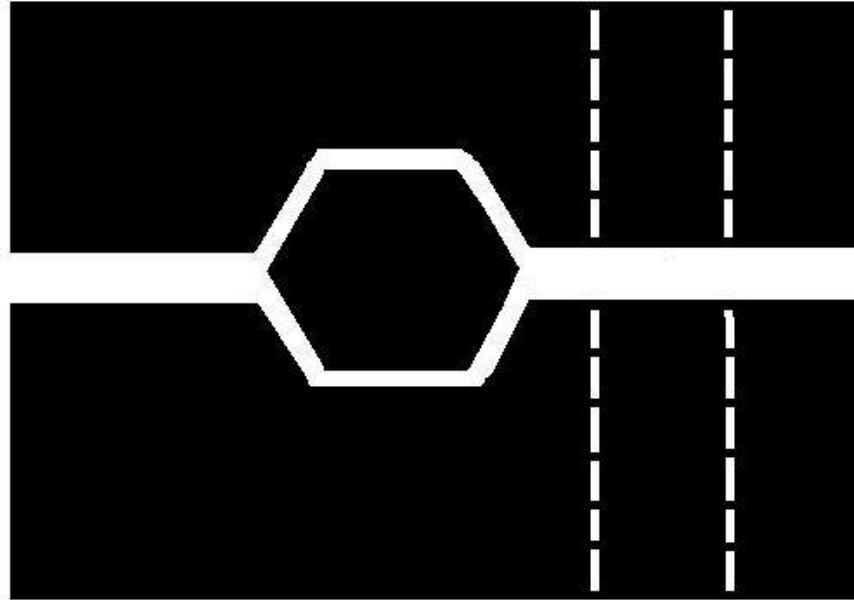


FIGURE 19. CROSS SECTION OF HEXAGONAL TONGUE AND GROOVE USED TO LOCK THE FABRIC IN THE TARGET HOLDER

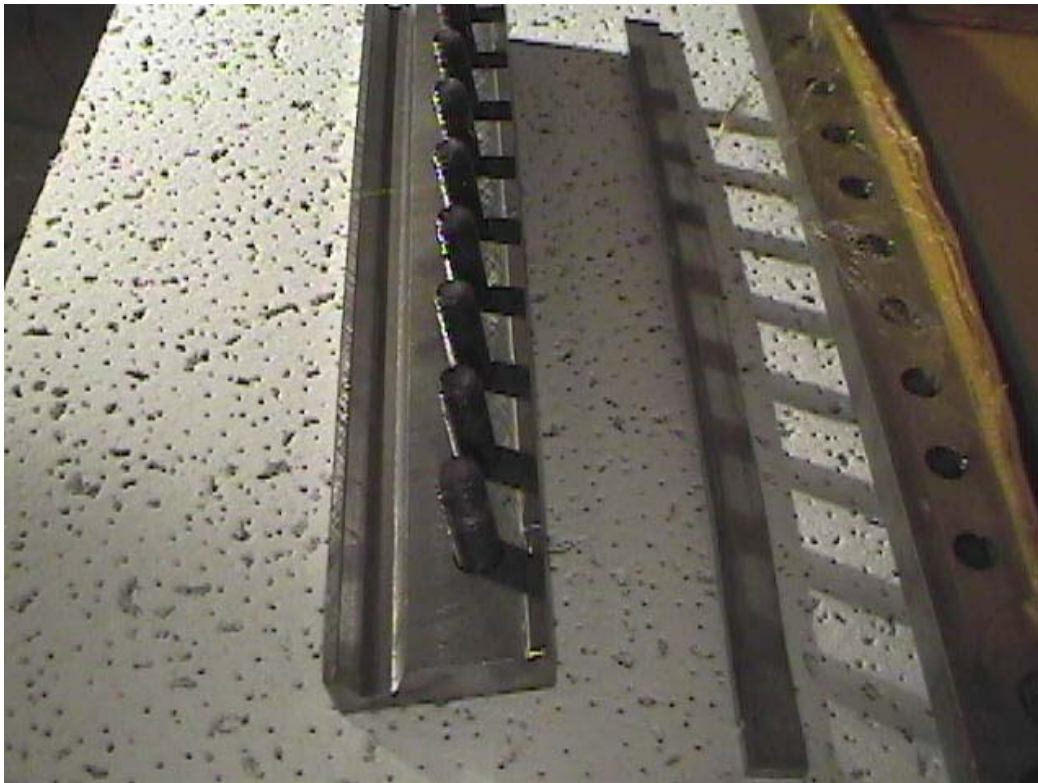


FIGURE 20. HEXAGON GROOVE ON THE CLAMPING EDGE

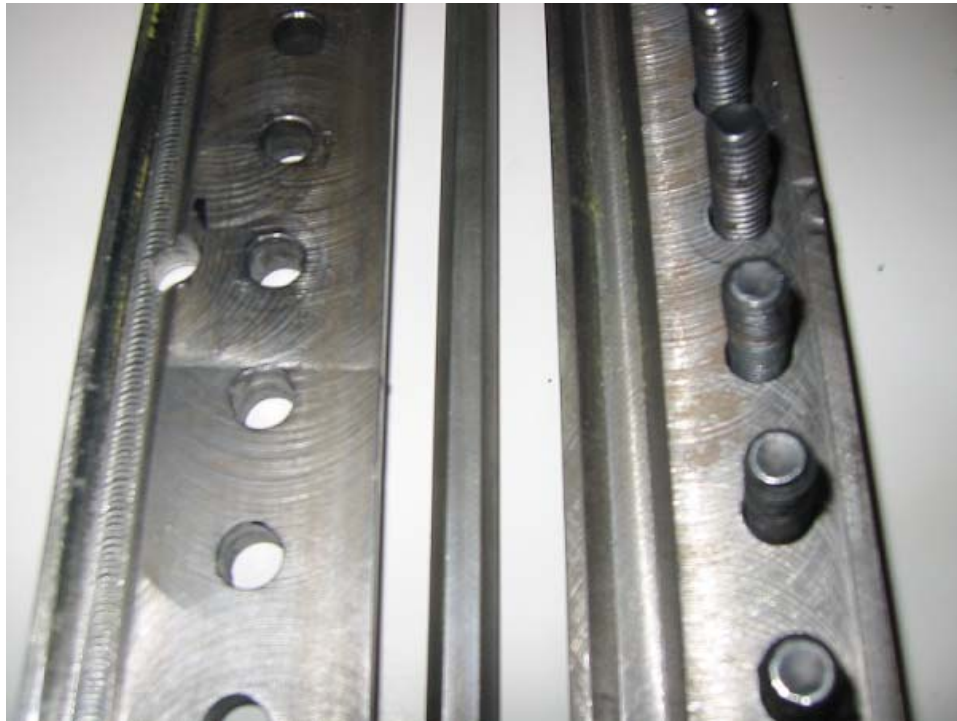


FIGURE 21. CLOSE-UP OF THE COMPLETE HEXAGONAL TONGUE AND GROOVE SYSTEM



FIGURE 22. COMPLETE TARGET HOLDER WITH ALL FOUR CLAMPS



FIGURE 23. TARGET MOUNT ATTACHED TO THE POWDER GUN TABLE

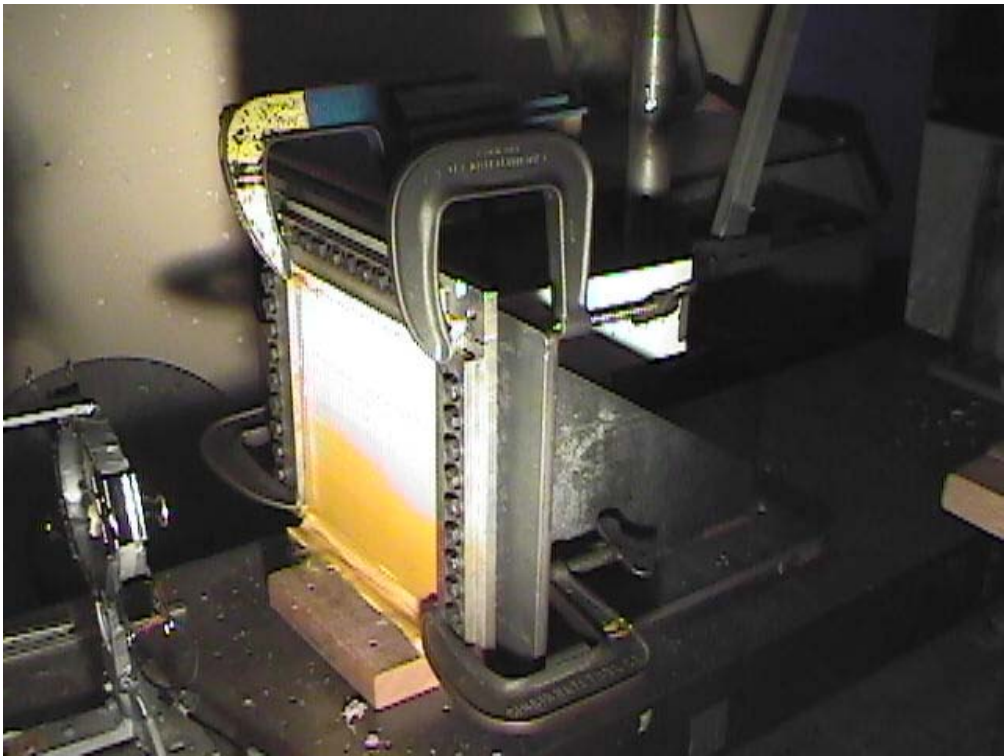


FIGURE 24. TARGET HOLDER ATTACHED TO THE TARGET MOUNT BY FOUR C-CLAMPS



FIGURE 25. BLAST SHIELD IN FRONT OF THE MUZZLE OF THE POWDER GUN



FIGURE 26. CATCHER BOX FILLED WITH RAGS, FOAM, AND NEWSPAPER



FIGURE 27. SIDE VIEW OF THE CLAMPING EDGE INSTALLED INTO THE TARGET HOLDER

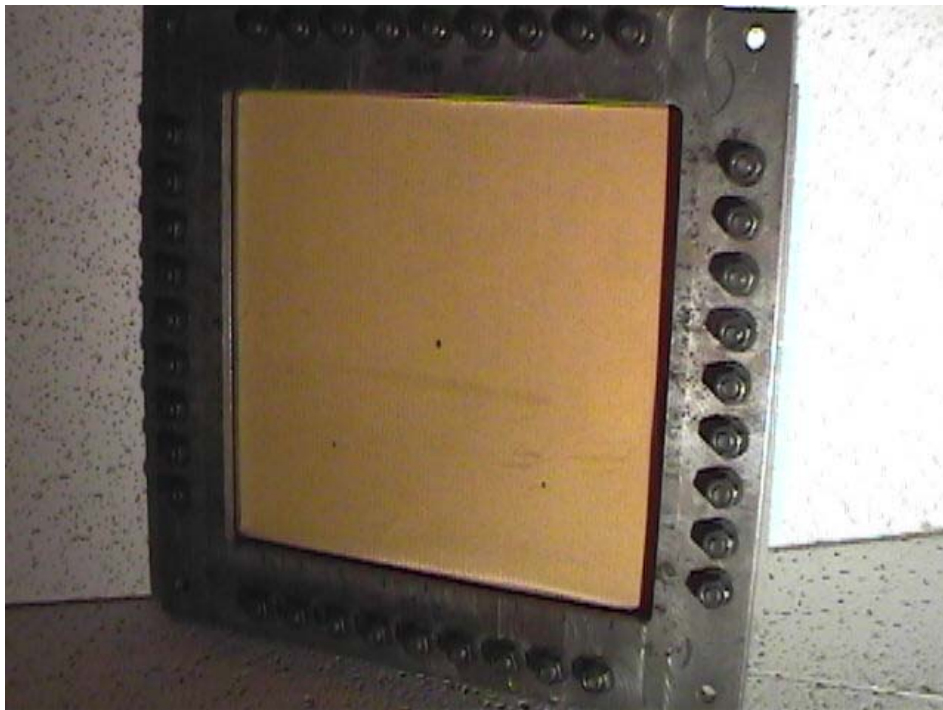


FIGURE 28. ALL FOUR CLAMPING EDGES INSTALLED WITH NUTS AND BOLTS TIGHTENED

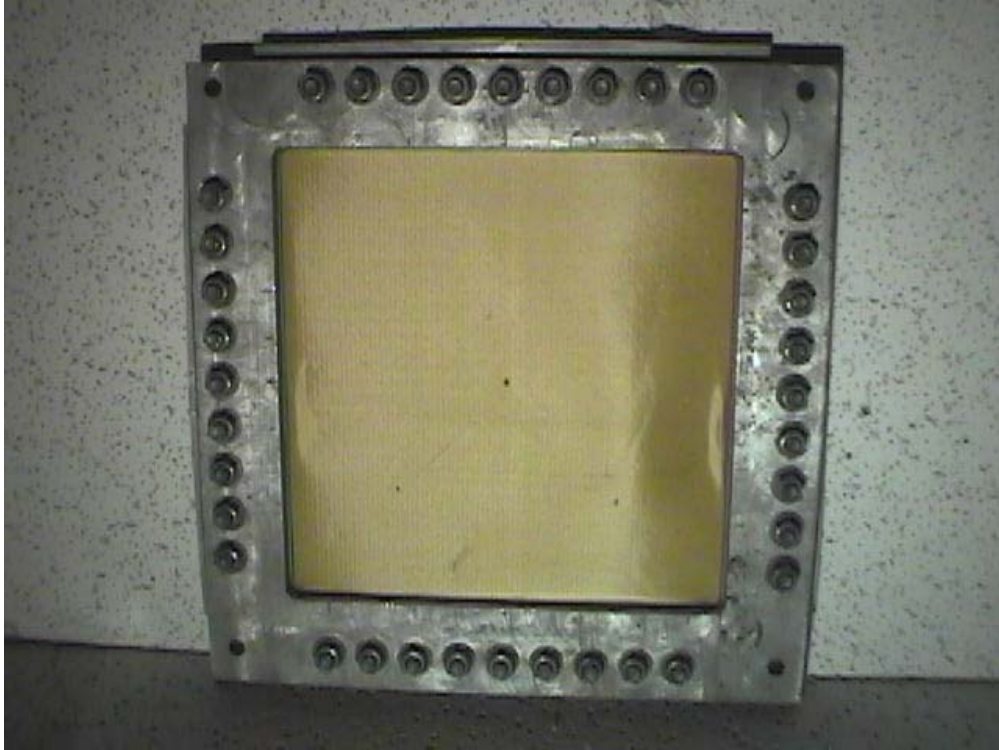


FIGURE 29. FRONT VIEW OF ALL FOUR CLAMPING EDGES

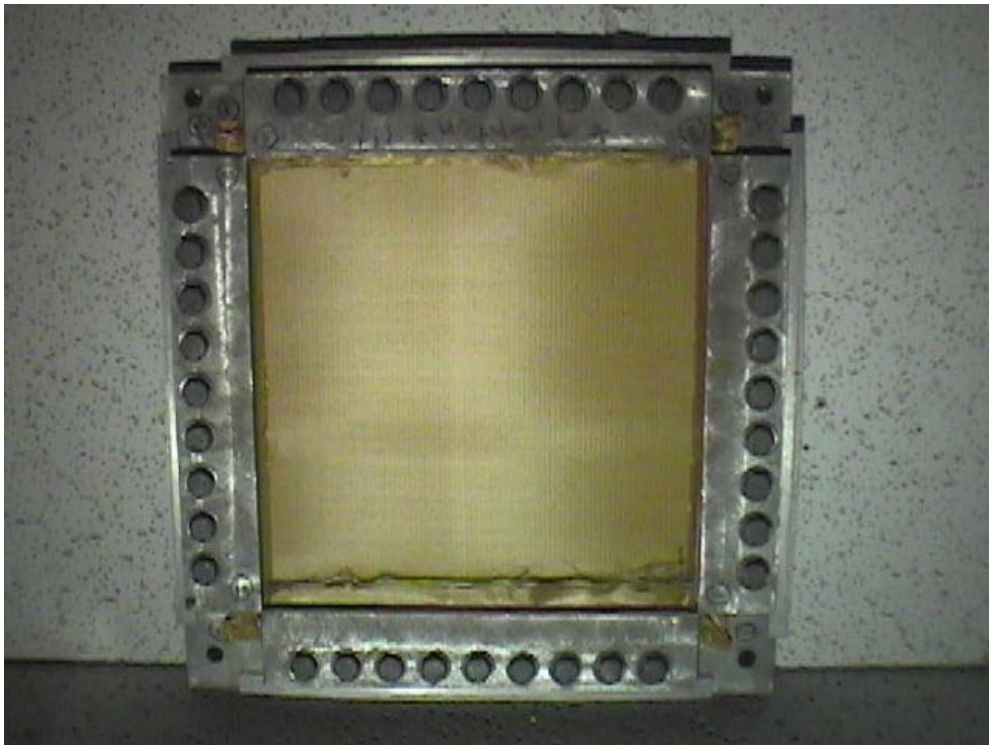


FIGURE 30. BACK VIEW OF ALL FOUR CLAMPING EDGES



FIGURE 31. TARGET HOLDER IN A TWO-CLAMP CONFIGURATION



FIGURE 32. ARROWHEAD CUTTER



FIGURE 33. THE FOUR-PEG CONFIGURATION

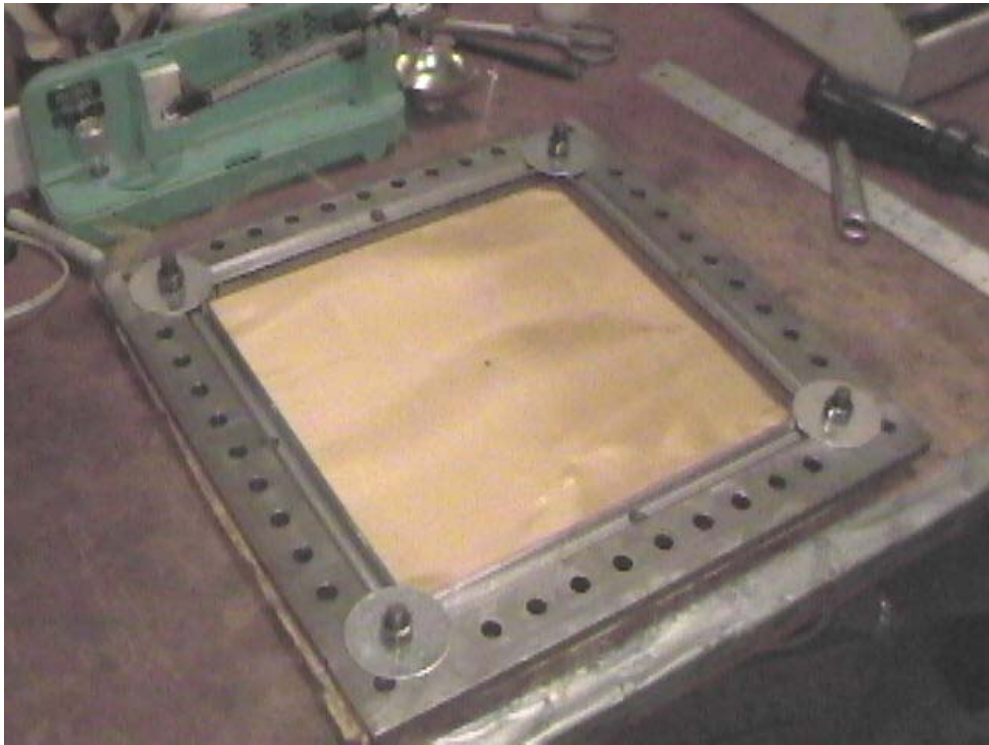


FIGURE 34. THE FOUR-PEG CONFIGURATION WITH ZYLON INSTALLED



FIGURE 35. THE EIGHT-PEG CONFIGURATION



FIGURE 36. THE FIRING SWITCH

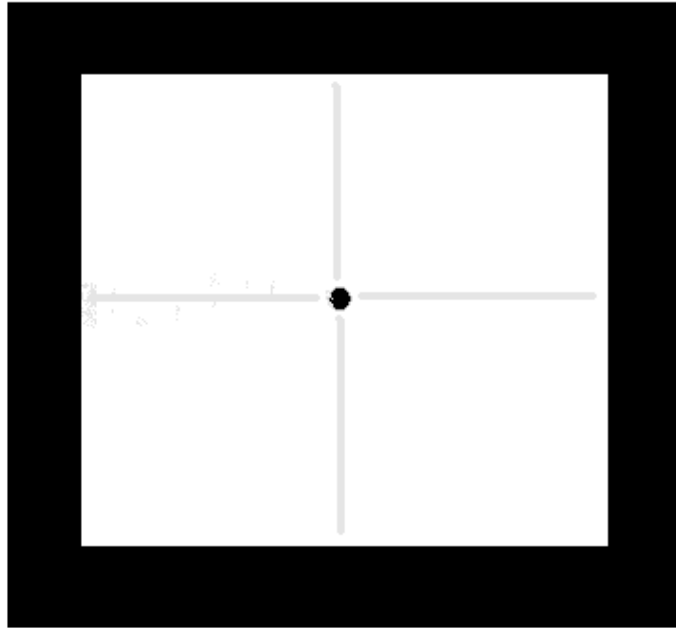


FIGURE 37. SKETCH OF THE DAMAGE PATTERN ON THE FABRIC IN THE TARGET HOLDER FROM A CENTER SHOT

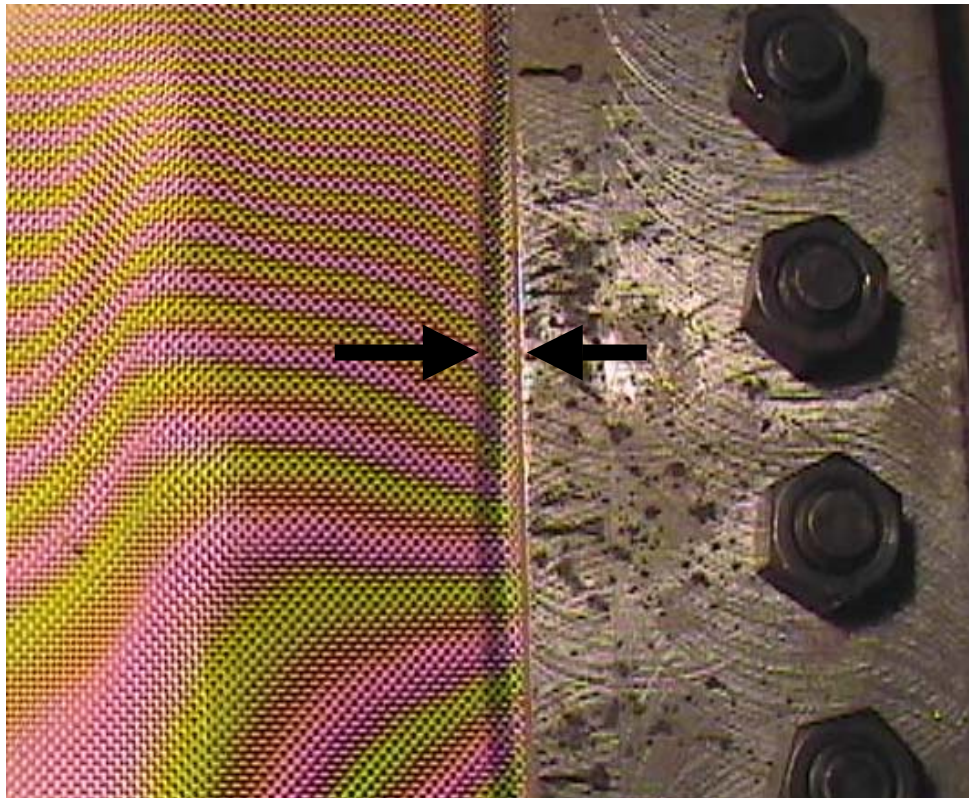


FIGURE 38. SLIP AT THE TARGET HOLDER BOUNDARY, INDICATED BY THE DISPLACEMENT OF THE BLACK MARKER LINE

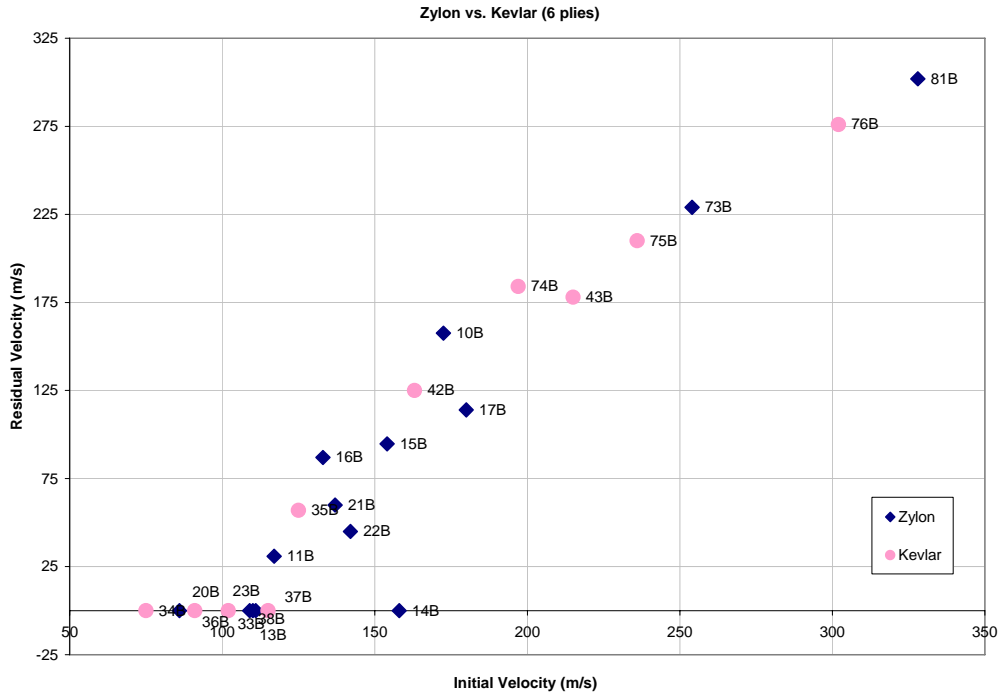


FIGURE 39. INITIAL VS RESIDUAL VELOCITY FOR ZYLON AND KEVLAR—FOUR-CLAMP CENTER SHOTS

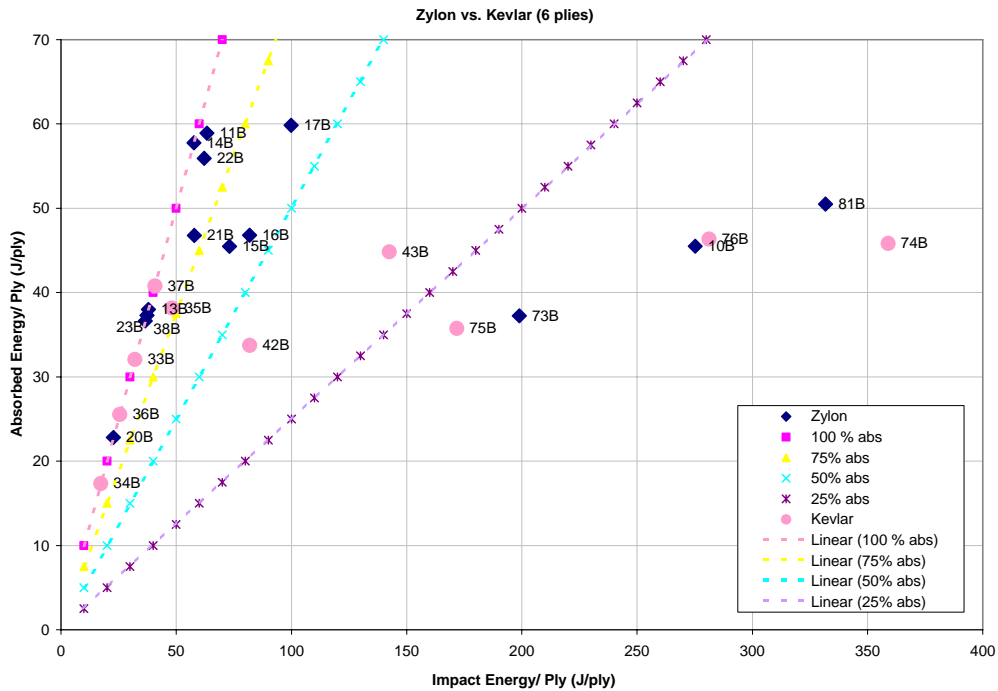


FIGURE 40. IMPACT ENERGY VS ABSORBED ENERGY FOR ZYLON AND KEVLAR—FOUR-CLAMP CENTER SHOTS

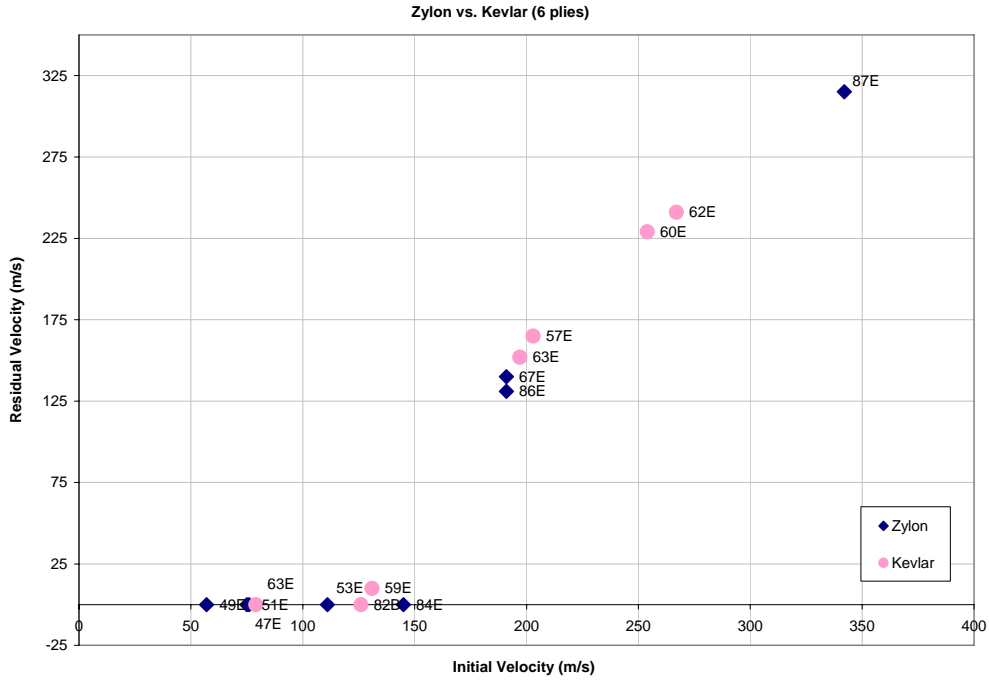


FIGURE 41. INITIAL VS RESIDUAL VELOCITY FOR ZYLON AND KEVLAR—TWO-CLAMP CENTER SHOTS

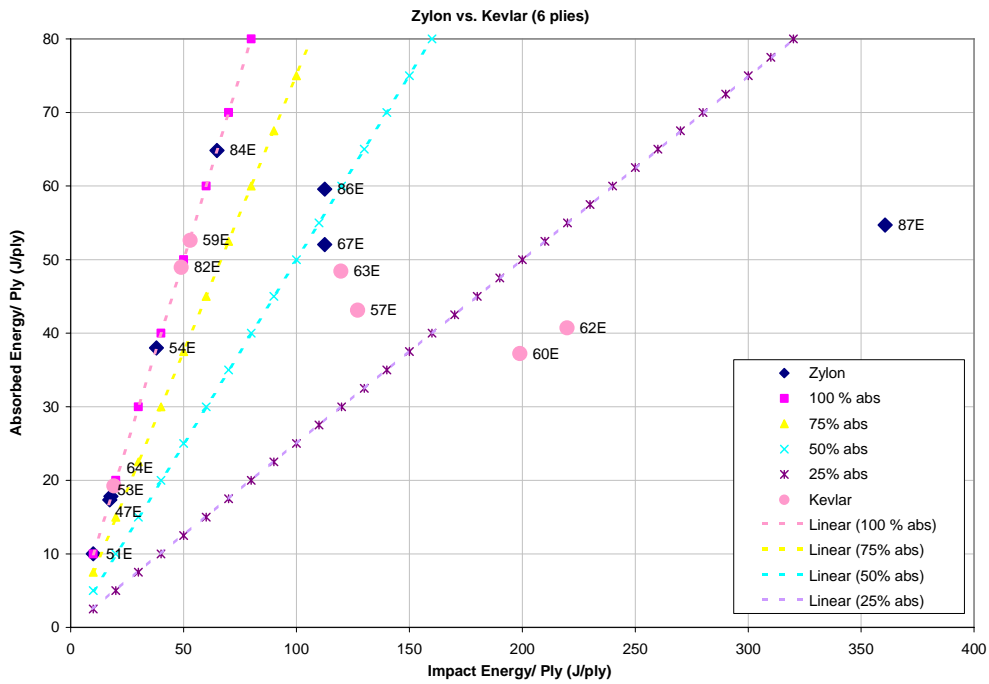


FIGURE 42. IMPACT ENERGY VS ABSORBED ENERGY FOR ZYLON AND KEVLAR—TWO-CLAMP CENTER SHOTS

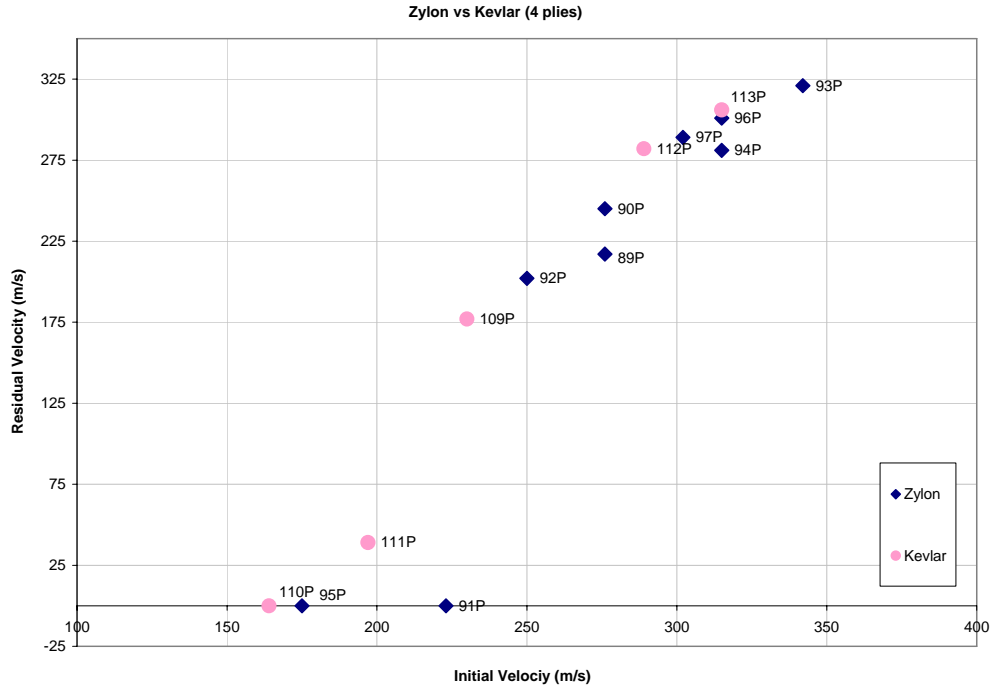


FIGURE 43. INITIAL VS RESIDUAL VELOCITY FOR ZYLON AND KEVLAR—FOUR-PEG CENTER SHOTS

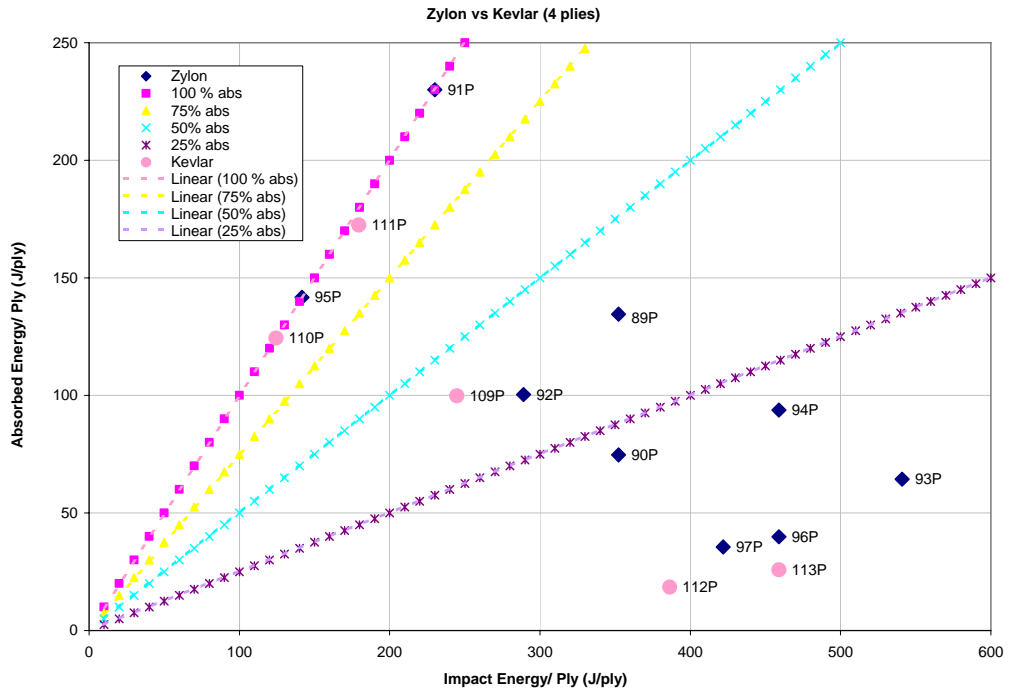


FIGURE 44. IMPACT ENERGY VS ABSORBED ENERGY FOR ZYLON AND KEVLAR—FOUR-PEG CENTER SHOTS

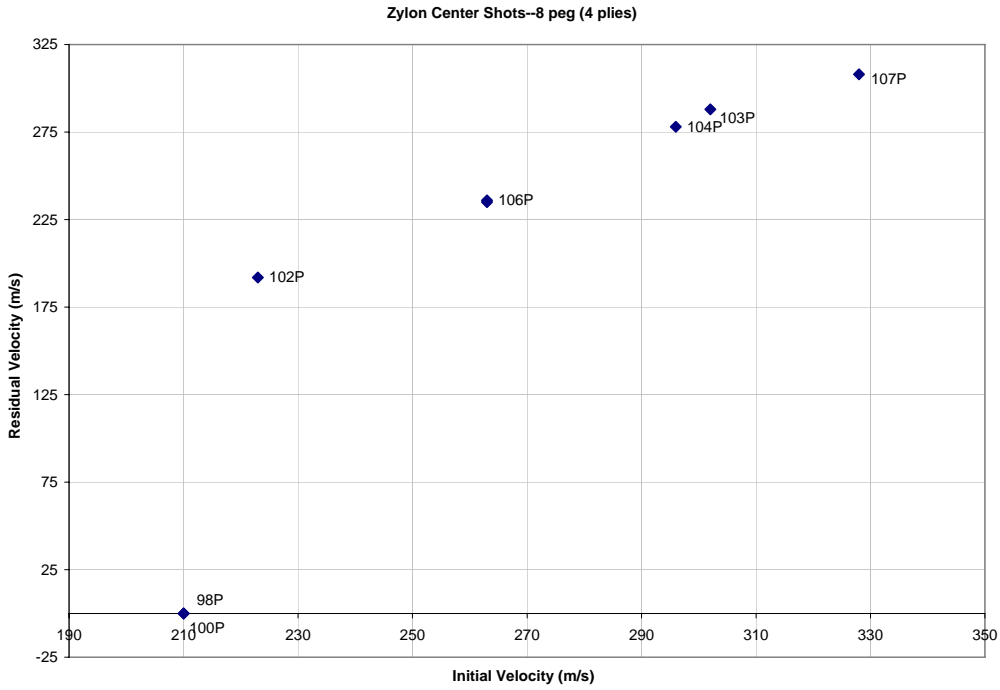


FIGURE 45. INITIAL VS RESIDUAL VELOCITY FOR ZYLON—EIGHT-PEG CENTER SHOTS

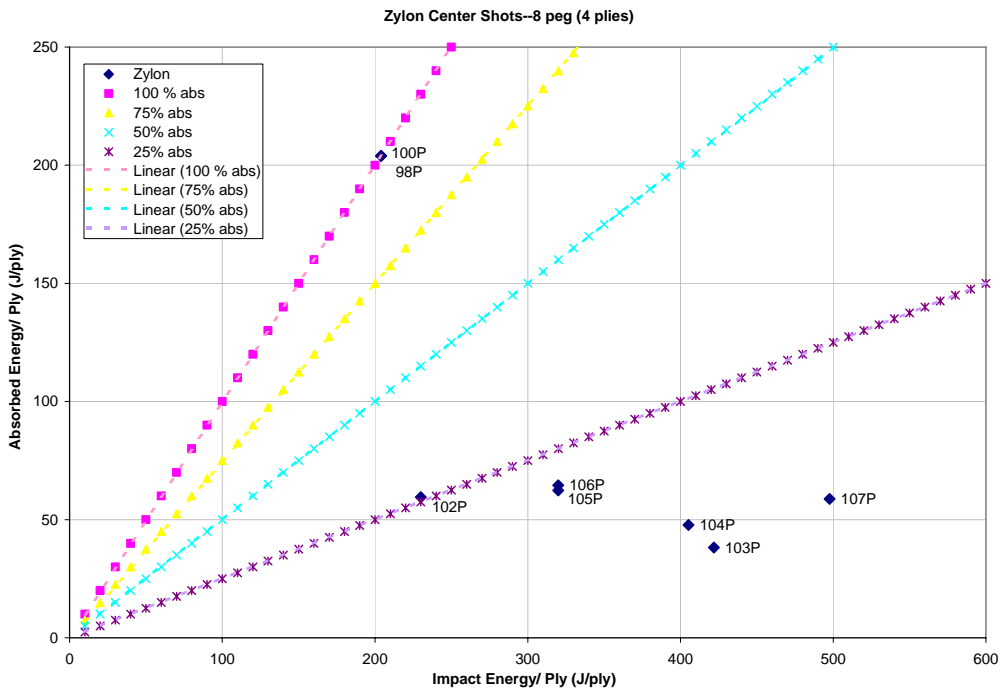


FIGURE 46. IMPACT ENERGY VS ABSORBED ENERGY FOR ZYLON—EIGHT-PEG CENTER SHOTS

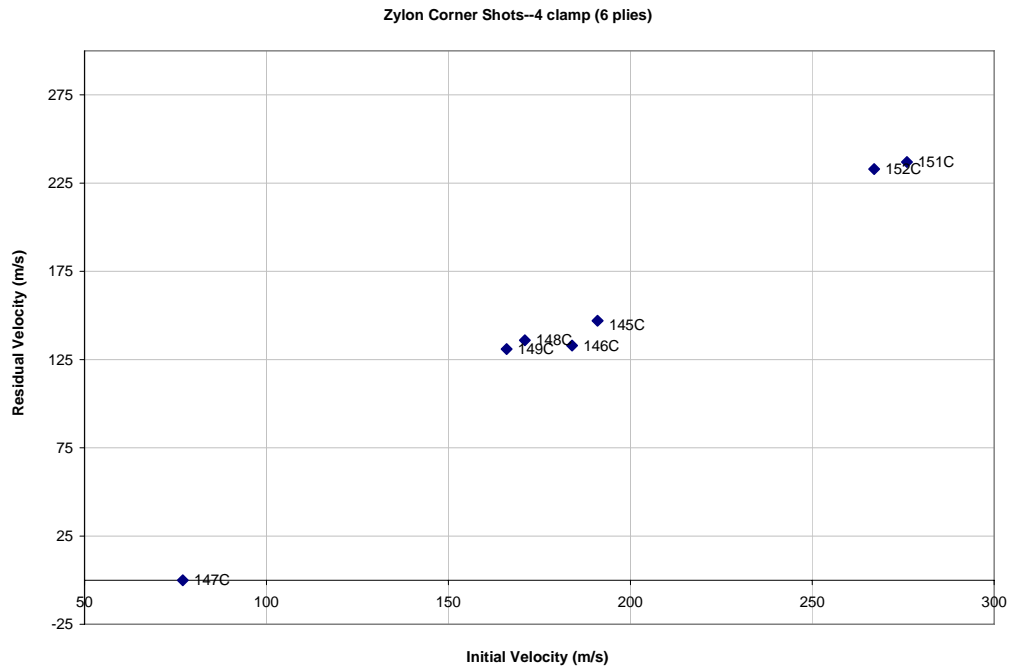


FIGURE 47. INITIAL VS RESIDUAL VELOCITY FOR ZYLON—
FOUR-CLAMP DIAGONAL SHOTS

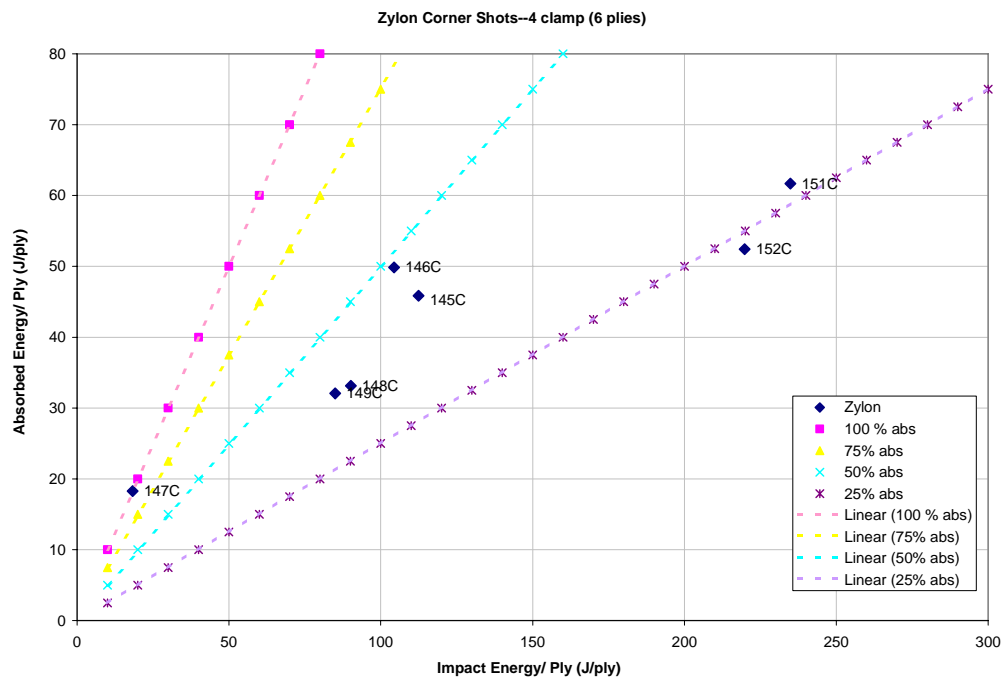


FIGURE 48. IMPACT ENERGY VS ABSORBED ENERGY FOR ZYLON—
FOUR-CLAMP DIAGONAL SHOTS

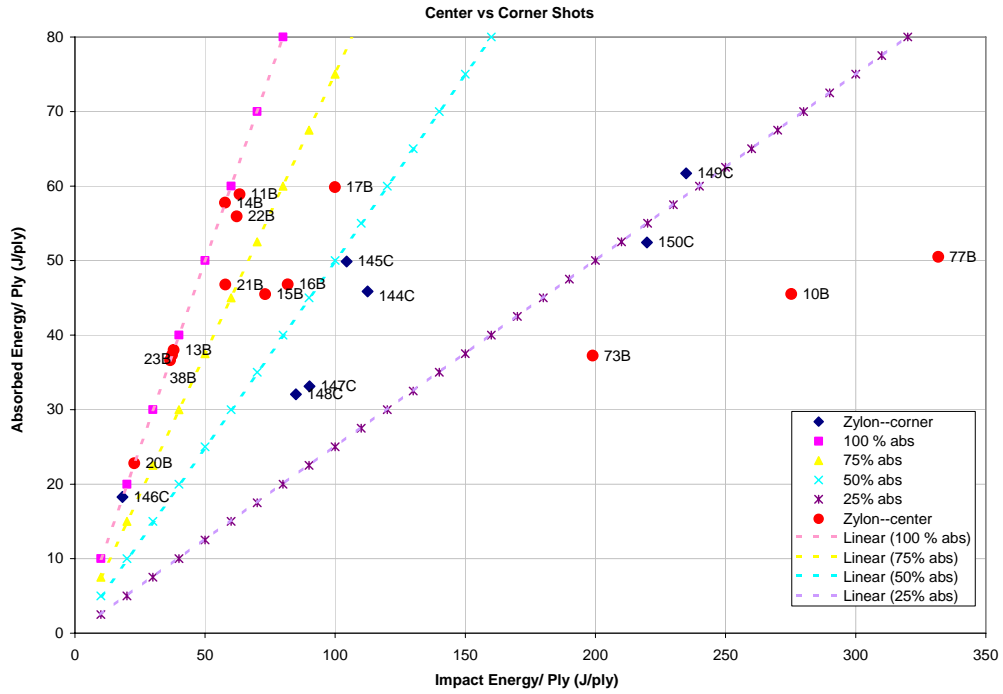


FIGURE 49. IMPACT ENERGY VS ABSORBED ENERGY FOR ZYLON—COMPARISON BETWEEN FOUR-CLAMP CENTER AND DIAGONAL SHOTS

Zylon Midway Shots--2 clamp (6 plies)

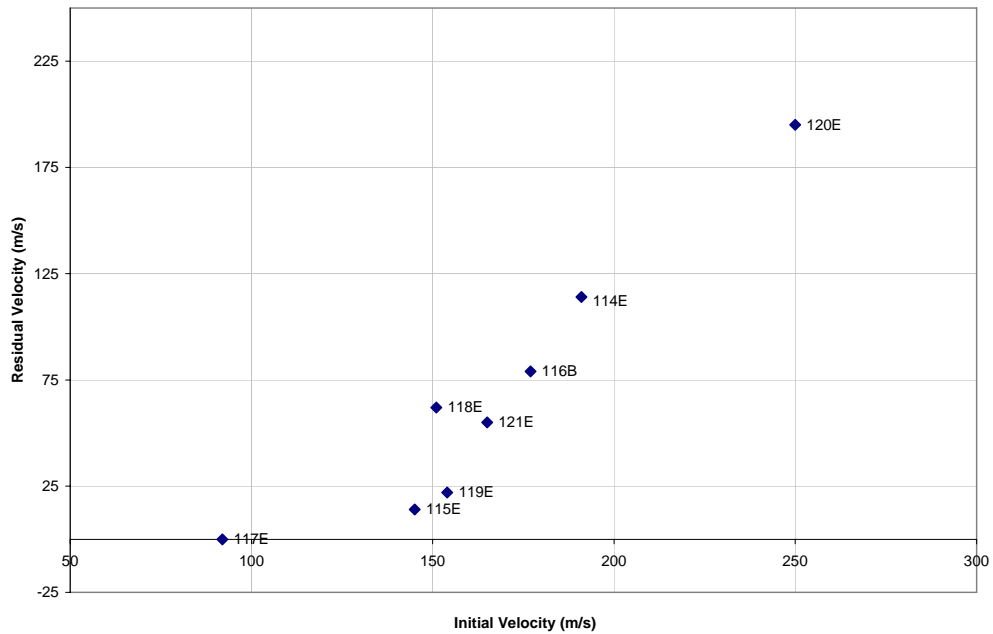


FIGURE 50. INITIAL VS RESIDUAL VELOCITY FOR ZYLON—TWO-CLAMP MIDWAY SHOTS

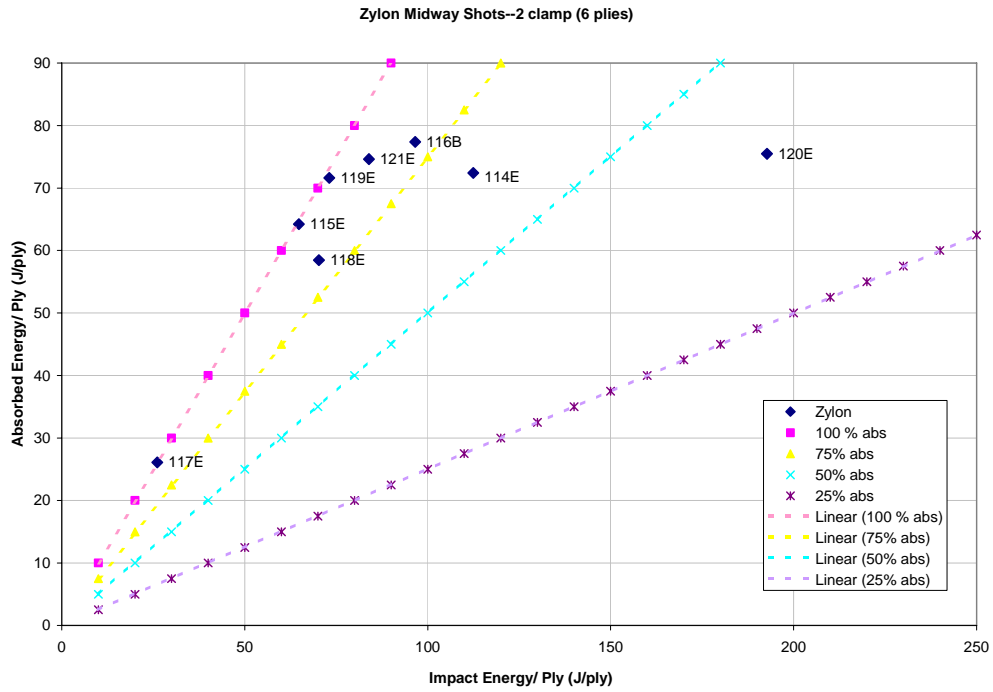


FIGURE 51. IMPACT ENERGY VS ABSORBED ENERGY FOR ZYLON—TWO-CLAMP MIDWAY SHOTS

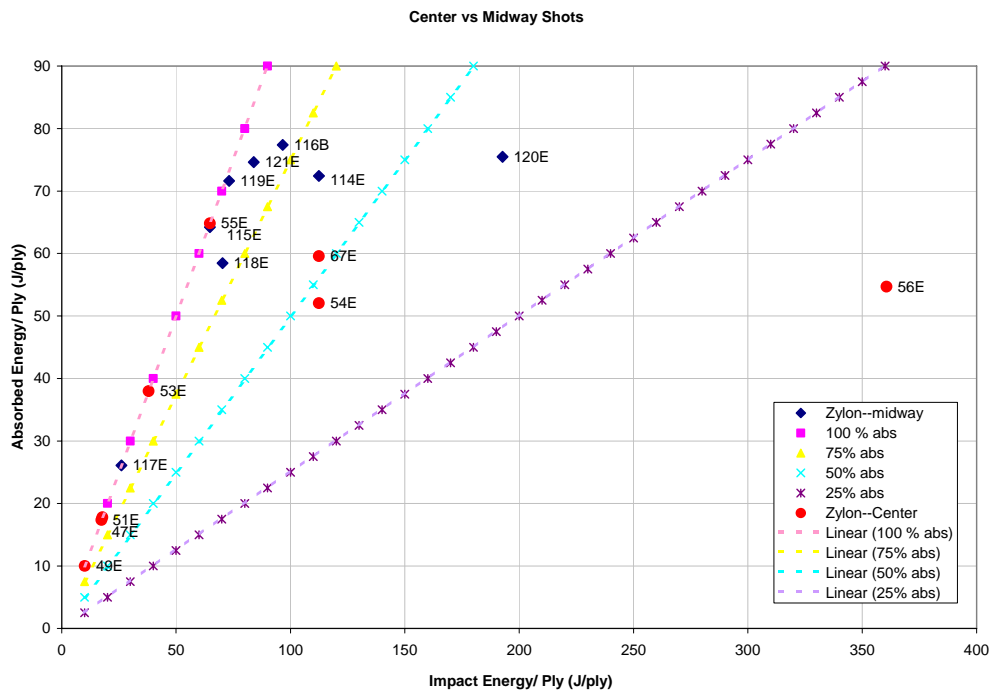


FIGURE 52. IMPACT ENERGY VS ABSORBED ENERGY FOR ZYLON—COMPARISON BETWEEN TWO-CLAMP CENTER AND MIDWAY SHOTS

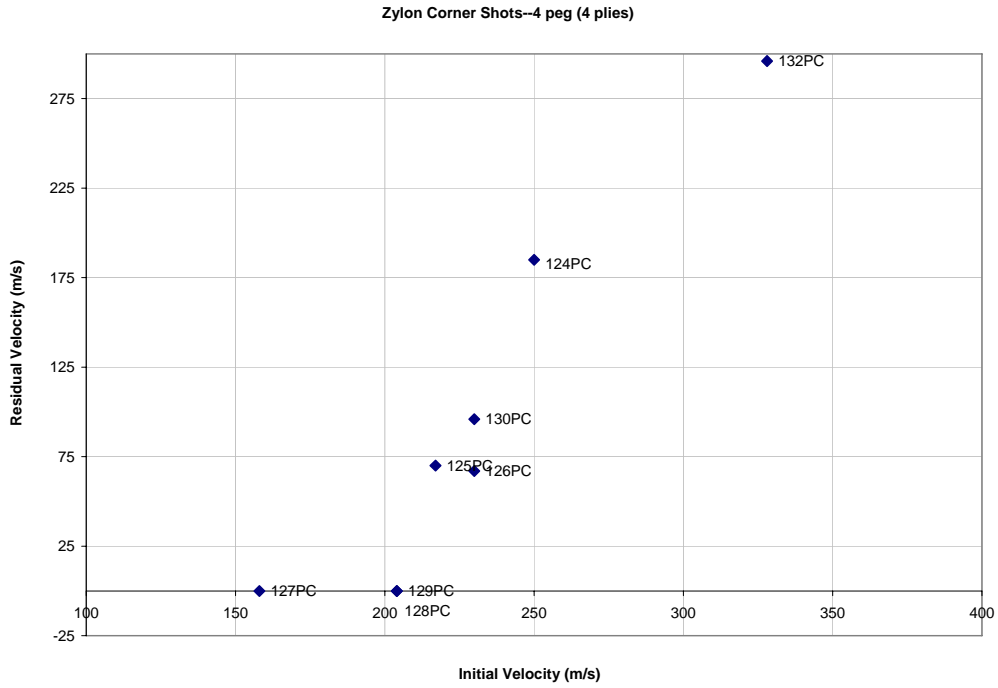


FIGURE 53. INITIAL VS RESIDUAL VELOCITY FOR ZYLON—
FOUR-PEG DIAGONAL SHOTS

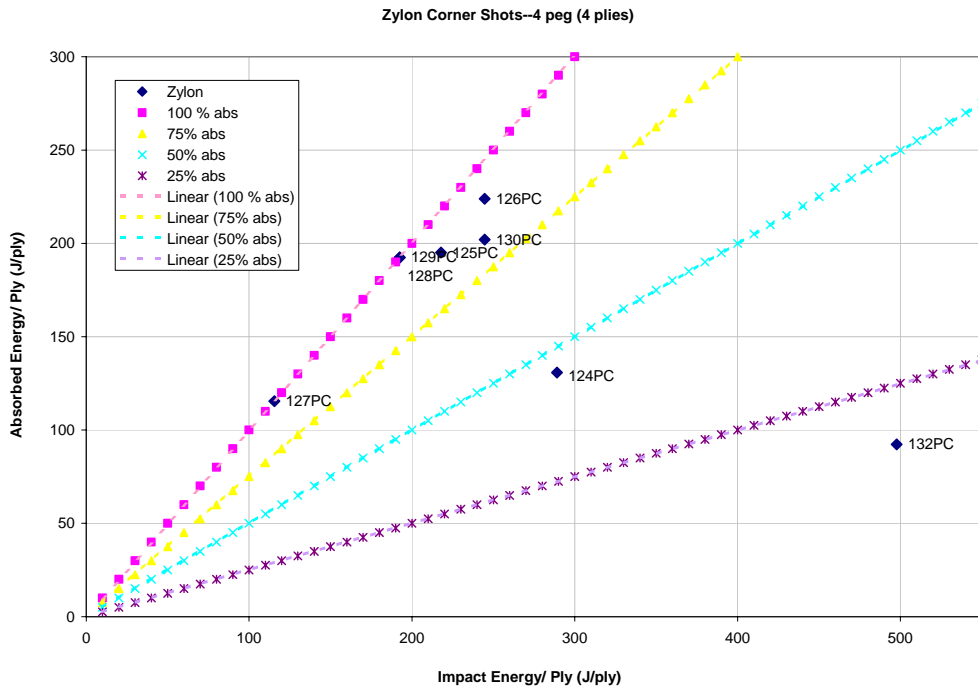


FIGURE 54. IMPACT ENERGY VS ABSORBED ENERGY FOR ZYLON—
FOUR-PEG DIAGONAL SHOTS

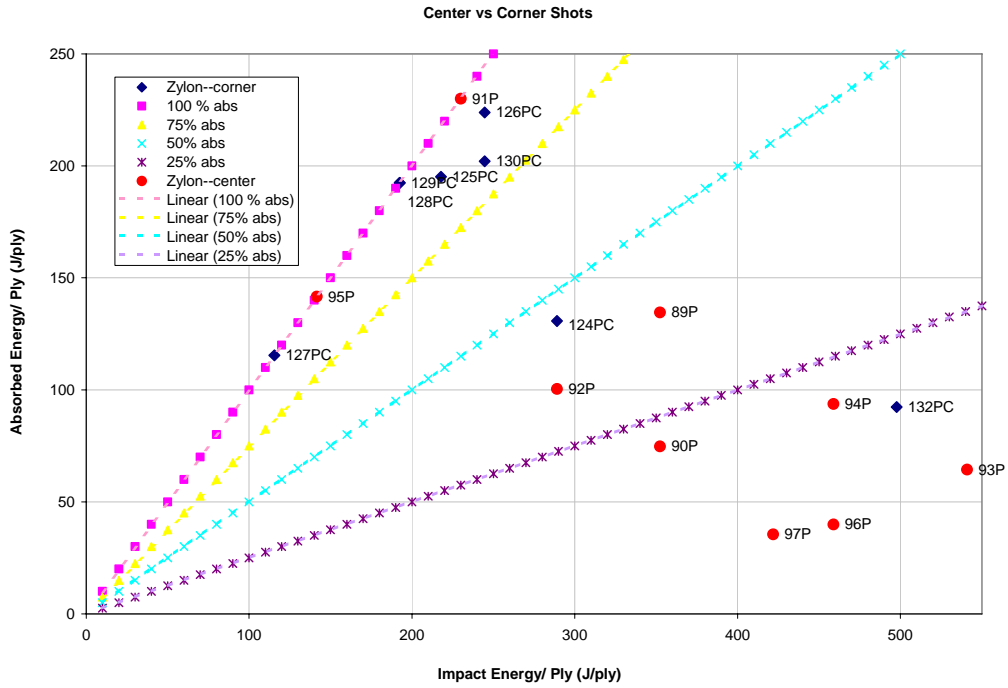


FIGURE 55. IMPACT ENERGY VS ABSORBED ENERGY FOR ZYLON—COMPARISON BETWEEN FOUR-PEG CENTER AND DIAGONAL SHOTS

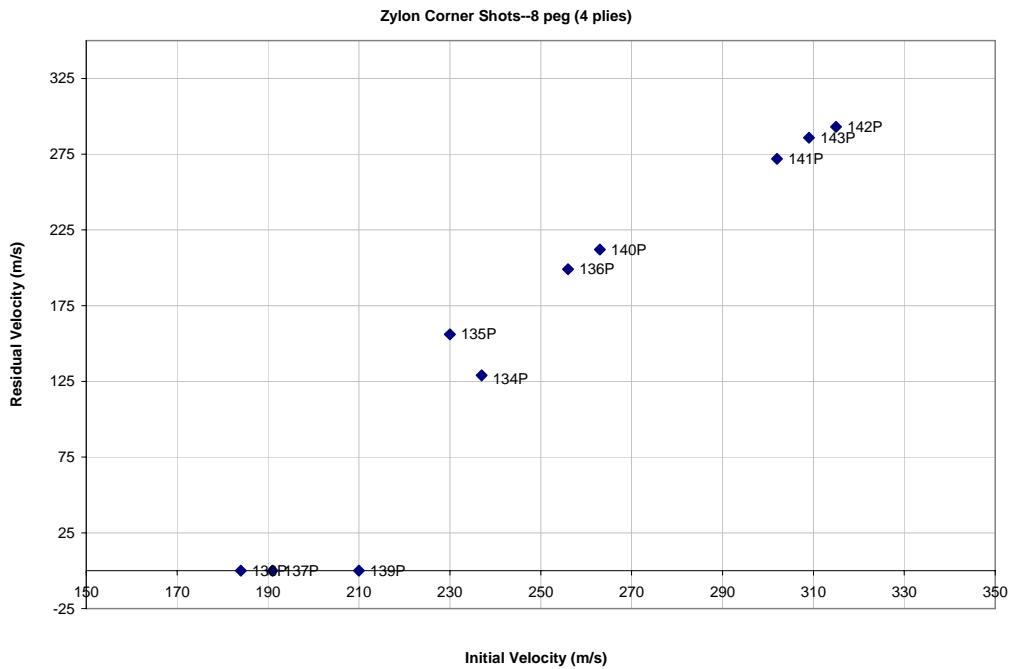


FIGURE 56. INITIAL VS RESIDUAL VELOCITY FOR ZYLON—EIGHT-PEG DIAGONAL SHOTS

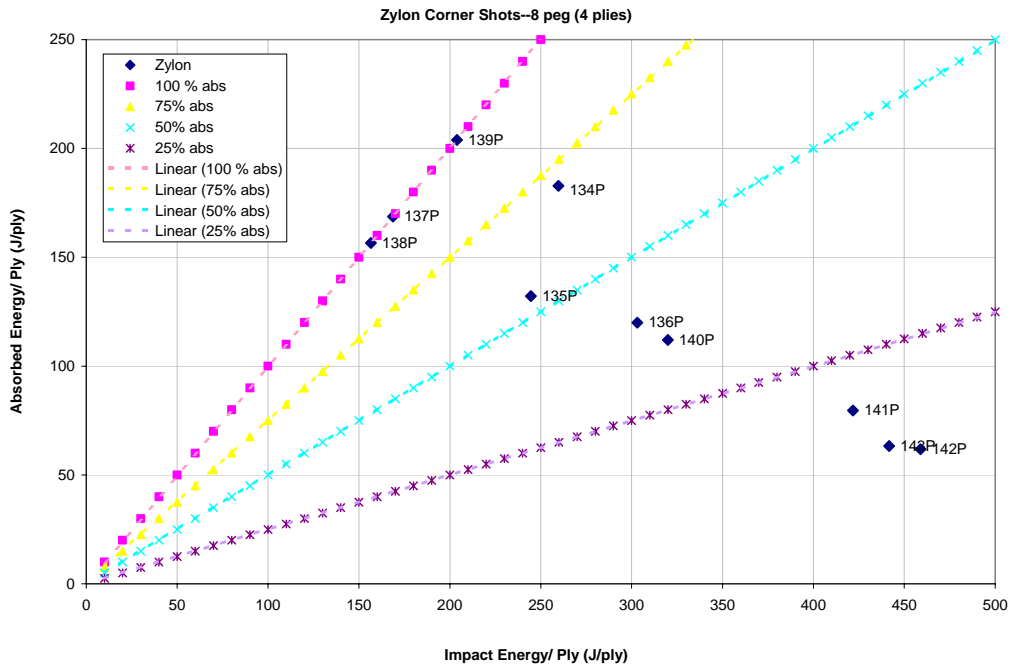


FIGURE 57. IMPACT ENERGY VS ABSORBED ENERGY FOR ZYLON—EIGHT-PEG DIAGONAL SHOTS

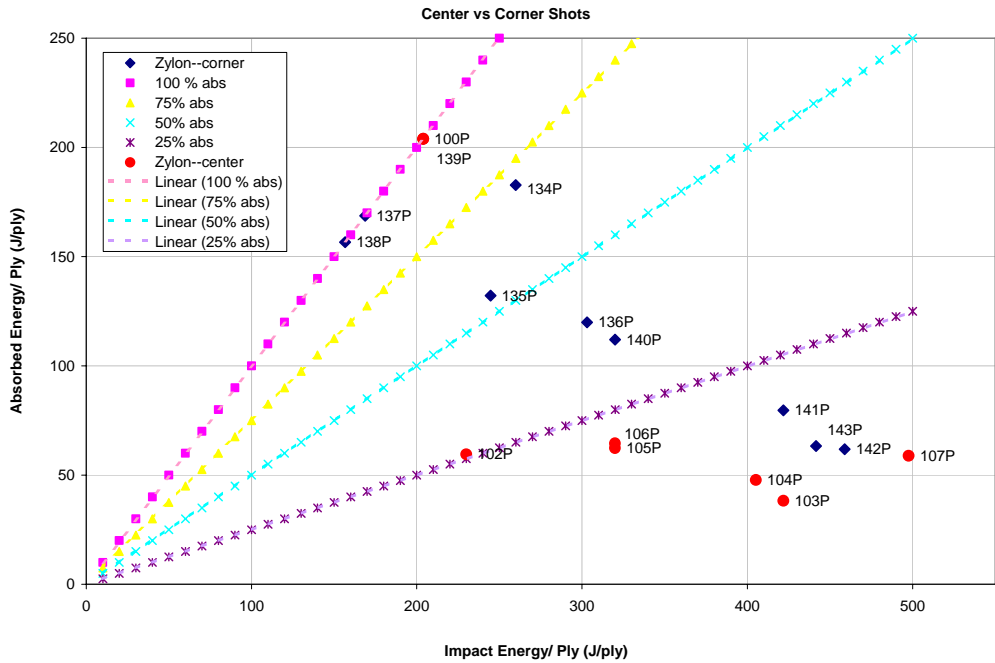


FIGURE 58. IMPACT ENERGY VS ABSORBED ENERGY FOR ZYLON—COMPARISON BETWEEN EIGHT-PEG CENTER AND DIAGONAL SHOTS

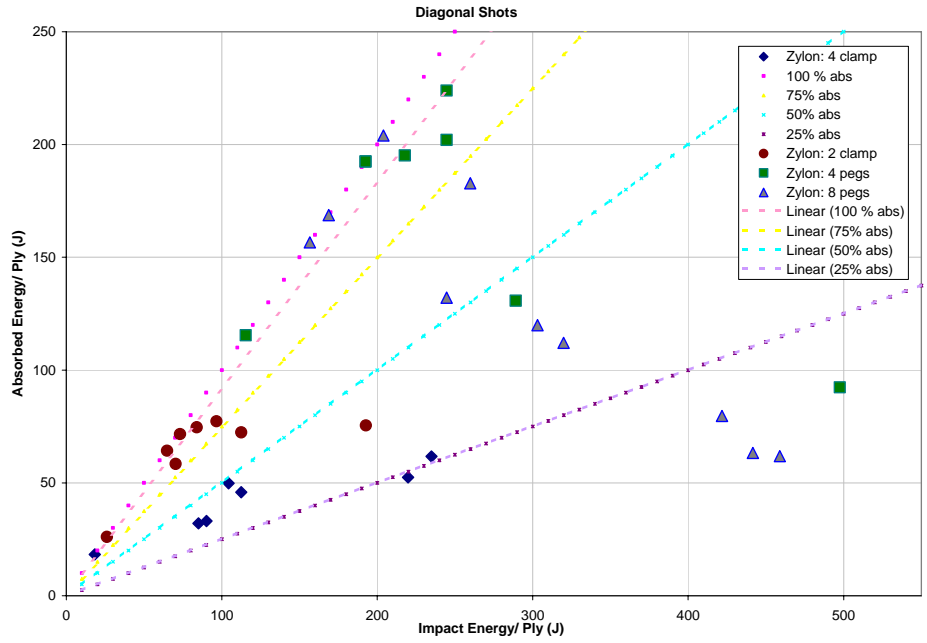


FIGURE 59. IMPACT ENERGY VS ABSORBED ENERGY FOR ZYLON—
ALL DIAGONAL SHOTS
(The two- and four-clamp (six plies) configurations, and the four- and eight-peg (four plies) configurations.)

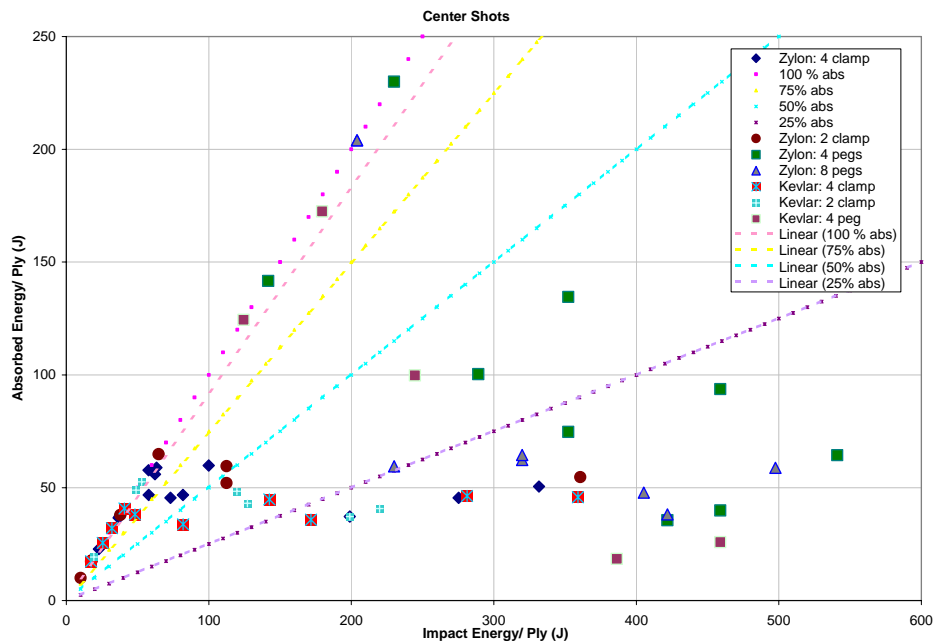


FIGURE 60. IMPACT ENERGY VS ABSORBED ENERGY FOR ZYLON AND KEVLAR—ALL CENTER SHOTS
(The two- and four-clamp (six plies) configurations and the four- and eight-peg (four plies) configurations)

TABLE 1. SUMMARY OF ABSORBED ENERGIES FOR NONPERFORATING SHOTS

Configuration	Upper Limit of Absorbed Energy for Nonperforation
4-Clamp—Zylon	~45-63 J/ply
4-Clamp—Kevlar	~32-45 J/ply
2-Clamp—Zylon	~65 J/ply
2-Clamp—Kevlar	~49 J/ply
4-Peg—Zylon	~230 J/ply
4-Peg—Kevlar	~172 J/ply
8-Peg—Zylon	~204 J/ply

APPENDIX A—MODELING OF THE BALLISTIC LIMIT OF MICRO-STOCHASTIC
FABRIC SHIELDING

Modeling of the ballistic limit of micro-stochastic fabric shielding

BY T. I. ZOHDI

Department of Mechanical Engineering, 6195 Etcheverry Hall, University of California, Berkeley, CA, 94720-1740, USA

Key words: ballistic fabric, micro-macro uncertainty

Abstract: In this work, a multiscale model is developed for ballistic fabric shielding. In the model, the degree of response uncertainty, from yarn to yarn, due to misalignment of the micro-fibers which comprise the yarn, is taken into account. A temporally implicit scheme is developed to solve the stochastic system. Large-scale numerical simulations are then given to illustrate the approach in determining the number of ballistic sheets needed to stop an incoming projectile. An important byproduct of this approach is that the model can reproduce scatter observed in laboratory experiments.

1. Introduction

There are a wide range of applications of lightweight ballistic fabric, including body armor, protection of mission-critical military and commercial structural components, etc. For example, one such fabric is Zylon (PBO), which is a synthetic material produced by the Toyobo Corporation (Toyobo [18]) constructed from woven PBO yarn, where each yarn is comprised of micro-fibers (Figure 1). Zylon appears to be far superior to Kevlar and other Aramids with regard to its mechanical properties and its resistance to heat, moisture and environmental degradation. The reader is referred to Roylance and Wang [14], Taylor and Vinson [17], Shim et al. [15], Johnson et al. [10], Tabiei and Jiang [16] Kollegal and Sridharan [11] and Walker [19] for overviews pertaining to ballistic fabric. Experimental ballistic tests on such materials are extremely expensive and time consuming. Therefore, it

is advantageous to employ computational simulations to serve as auxiliary tools to laboratory experiments needed in the evaluation of new types of ballistic fabric. In the forthcoming analysis, the specific material of interest is Zylon.

2. Experimental observations

The number of ballistic sheets of Zylon to be tested were cut with special scissors from a roll and clamped around a circular bar into a square holder. The two parts of this square frame, whose outside dimensions were 356 mm with a 254 mm square window, were secured by 9.5 mm diameter hard-steel bolts via an aluminum strip acting as a continuous washer. After assembly, this unit was clamped in a vertical position to a heavy triangular support mounted on a 700 kg steel table in such a manner that impact would be produced at a predetermined location on the target as determined by a laser beam mounted on the gun centerline. The tests were executed by means of custom-built 12.9 mm inside diameter powder gun with 20 mm thick high-strength steel barrel of 1.6 m length. This device was mounted by means of a rail frame on the same table as the target. The gun is capable of accommodating a 50 caliber shell into which the projectile is inserted. The striker consisted of a 12.7 mm diameter steel cylinder with a mass of 36 g, with an aspect ratio of 3:1, heat treated to a hardness of R_c 60, and copper-coated to a thickness of 0.5 mils to reduce barrel wear. A blast shield was placed in front of the muzzle to prevent interaction of the powder gases with target fibers. A projectile and fragment catcher consisting of a rag-filled box was positioned beyond all final velocity measuring units. All tests were conducted inside an enclosed chamber that was evacuated during firing. The initial velocity of the striker was determined from the time required to successively

break two parallel laser beams 156 mm apart that were focused on two photodiodes, located 1.5 m in front of the target. The signals from the diodes initiated the start and stop modes of a Hewlett-Packard 5316 time interval meter. Final velocities were determined in three ways: (1) By the use of a digital video recording camera operating at 10,000 frames/s, that captured the striker position at a number of instances after the perforation using the dimensions of the projectile or a scale for distance determination; (2) By means of two silver-coated paper make-circuit grids spaced 50.4 mm apart, whose voltage pulses were directed to a time-interval meter; and (3) two sets of 432 mm foils, with each pair separated by 12 mm and each set a distance of 12.7 mm apart, with the projectile contact providing a make circuit for each set, allowing the respective signals to start and stop a time interval meter. A calibration curve was established for initial velocity versus the amount of IMR 3031 powder placed in the shells. The number of desired plies were cut and inserted in the target holder and the bolts were tightened with a 306 N-m torque wrench. Our laboratory experiments indicate that between 11 and 12 ballistic sheets of Zylon were needed to stop a projectile with an incoming velocity of approximately 152 m/s (500 ft/s) that centrally impacts the target. In order to numerically simulate such tests, a multiscale model, which is amenable to direct computation, is developed in the next section.

3. Response of a single yarn

The axial strains in the mesoscale yarn comprising the fabric net (Figures 1 and 2) are expected to be in the range of 2 %-10 % before rupturing, therefore a Kirchhoff-St. Venant material model is considered, $\mathbf{S} = \mathbf{I}\mathbf{E}^Y : \mathbf{E}$, where \mathbf{S} is the second Piola-

Kirchhoff stress, $\mathbf{I}\mathbf{E}^Y$ is the elasticity tensor of a single yarn, $\mathbf{E} \stackrel{\text{def}}{=} \frac{1}{2}(\mathbf{C} - \mathbf{1})$ is the Green-Lagrange strain, $\mathbf{C} \stackrel{\text{def}}{=} \mathbf{F}^T \cdot \mathbf{F}$ is the right Cauchy-Green strain, $\mathbf{F} = \nabla_{\mathbf{X}} \mathbf{x}$ is the deformation gradient and where \mathbf{X} are referential and \mathbf{x} are current coordinates, respectively. The Cauchy stress, $\boldsymbol{\sigma}$, is related to the second Piola-Kirchhoff stress in the following manner, $\boldsymbol{\sigma} = \frac{1}{J} \mathbf{F} \cdot \mathbf{S} \cdot \mathbf{F}^T$, where J is the Jacobian of \mathbf{F} , $J = \det \mathbf{F}$. The yarn form a lattice by having individual yarn tied together at connecting nodes (Figure 2). † Since the yarn are quite thin, one may assume a plane uniaxial-stress type condition. For the analysis of a single yarn, one aligns the coordinate system with the undeformed axial (x_1) state, where C_{11} is the component of \mathbf{C} *along the length of the yarn*. Due to the assumption regarding the stress state, $S_{22} = S_{33} = 0$. Because the material is assumed to be isotropic, this implies that the Cauchy stress, written in terms of a coordinate system where one axis is aligned with the deformed axial direction of the yarn, also has only one nonzero (axial) component. By setting $S_{22} = S_{33} = 0$, one obtains relations for $C_{22} = C_{33}$ in terms of C_{11} . All other components of \mathbf{C} are zero. Since the yarn material is assumed to be isotropic, with a Young's modulus of E^Y and a Poisson ratio of ν , one has $E_{11} = \frac{S_{11}}{E^Y} - \nu(\frac{S_{22}+S_{33}}{E^Y})$, $E_{22} = \frac{S_{22}}{E^Y} - \nu(\frac{S_{11}+S_{33}}{E^Y})$ and $E_{33} = \frac{S_{33}}{E^Y} - \nu(\frac{S_{11}+S_{22}}{E^Y})$. Enforcing $S_{22} = S_{33} = 0$, one obtains $S_{11} = E^Y E_{11}$ and $E_{22} = E_{33} = -\nu E_{11}$, and consequently $C_{22} = -\nu(C_{11} - 1) + 1 = C_{33}$, implying

$$J = \sqrt{C_{11}C_{22}C_{33}} = \sqrt{C_{11}(-\nu(C_{11} - 1) + 1)^2}. \quad (3.1)$$

† In reality the yarn are tightly woven and the nodes are the criss-cross contact junctions between the warp and the fill of the weave. Later in the analysis, the nodes will also serve as locations of lumped masses.

One may decompose the deformation gradient into a rotation and stretch, $\mathbf{F} = \mathbf{R} \cdot \mathbf{U}$. For an individual yarn one has $U_{11} = U_I = \frac{L_I}{L_o}$, $U_{22} = \sqrt{C_{22}}$, $U_{33} = \sqrt{C_{33}}$, where L_I is the deformed length of the I th yarn, and L_o is its original length. Explicitly, the axial stretch of the I th yarn is $U_I = \frac{L_I}{L_o}$. The Cauchy stress is $\boldsymbol{\sigma} = \frac{1}{J} \mathbf{R} \cdot \mathbf{U} \cdot \mathbf{S} \cdot \mathbf{U}^T \cdot \mathbf{R}^T$. To determine the axial Cauchy stress one can simply re-write the stress tensor with respect to axes that are aligned with the deformed configuration, $\hat{\boldsymbol{\sigma}} = \mathbf{R}(-\gamma) \cdot \boldsymbol{\sigma} \cdot \mathbf{R}^T(-\gamma)$. All components of $\hat{\boldsymbol{\sigma}}$ are zero except for the axial component, which is simply $\sigma^a = \frac{1}{J} U_{11}^2 S_{11}$. This last expression, explicitly written out in terms of L_I and L_o , is

$$\sigma^a = \frac{\left(\frac{L_I}{L_o}\right) E^Y \frac{1}{2} \left(\left(\frac{L_I}{L_o}\right)^2 - 1\right)}{\left|(-\nu \left(\left(\frac{L_I}{L_o}\right)^2 - 1\right) + 1)\right|}. \quad (3.2)$$

For further details see Zohdi and Steigmann [20] and Zohdi [21].

The usual quantity of interest for fabrics used in structural applications is the global force-deflection (tensile) response, which is relatively insensitive to small local compressive and flexural responses. Therefore, analyses based on so-called relaxed theories of perfectly flexible solids are frequently used, which consist of enforcing a zero stress state for any compressive strains. Pipkin [13] appears to have been the first to have shown that such a model is compatible with the conventional theory of elastic surfaces by considering a minimizing sequence for an associated variational problem, and that such sequences have a structure similar to observed wrinkling in thin elastic sheets. These types of approaches have been adopted by numerous researchers for the elastostatic analysis of structural fibers; for example Buchholdt et. al [3], Pangiotopoulos [12], Bufler and Nguyen-Tuong [4] and Cannarozzi [5] and [6]. Steigmann and coworkers (Haseganu and Steigmann [7]-[9] and Atai and

Steigmann [1]-[2]) have developed a variety of theoretical results and elastostatic solution techniques based on pseudo-dynamic relaxation methods. A crucial theoretical result proven by Steigmann and coworkers is that a necessary condition for the existence of energy minimizers in elastostatics is for the yarn to carry no loading in compression. In the present work, this condition is adopted in the dynamic case as well, i.e. if $U_I \leq 1$, one enforces $\sigma^a = 0$.

4. Constitutive uncertainty

The rupture of most yarn used as shielding is not sudden, but rather gradual. This is attributed to inhomogeneous rupture of microscale fibers (micro-fibers) which comprise a single yarn (Figures 1 and 2). Due to the fact that the yarn are of finite (thin) thickness, with different random variations of the micro-fibers within the yarn, the material response is different from yarn to yarn. These differences can be quite large, in fact large enough to induce some scatter in macroscopic ballistic responses. In order to incorporate scatter into the macroscopic responses, consider a micro-fiber within a yarn. As in the case of the mesoscale yarn, a Kirchhoff-St. Venant model, $\mathbf{S} = \mathbf{I}\mathbf{E}_f^Y : \mathbf{E}$, is employed, where $\mathbf{I}\mathbf{E}_f^Y$ is the elasticity tensor of a single micro-fiber and where each micro-fiber is in a plane uniaxial-stress type condition. For the analysis of a single micro-fiber within a yarn, one aligns a coordinate system with the undeformed axial (x_1) state, where C_{11} is the component of \mathbf{C} along the length of the micro-fiber. As for the yarn, for the individual j th filament one has $U_{11} = U_j = \frac{L^j}{L_o^j}$, $U_{22} = \sqrt{C_{22}}$, $U_{33} = \sqrt{C_{33}}$, where L^j is the deformed length of the micro-fiber, and L_o^j is its original length. Explicitly, the axial stretch is (Figure 2)

$$U_j = \frac{L_j}{L_o^j} = \frac{\sqrt{(h_o + \Delta)^2 + d_j^2}}{\sqrt{h_o^2 + d_j^2}}, \quad (4.1)$$

where one denotes the initial nominal length between nodes by h_o , the length of misalignment for the j th micro-fiber within the yarn by d_j and where Δ is the displacement between two connected nodes (yarn connections). For the I th yarn (containing N_I micro-fibers), the effective axial second Piola-Kirchhoff response (per yarn) can be written in terms of the micro-fiber deformation and material properties

$$S_I = E_I^Y \frac{1}{2} \left(\frac{(h_o + \Delta)^2}{h_o^2} - 1 \right) = \frac{1}{N_I} \sum_{j=1}^{N_I} E_f^Y \frac{1}{2} \left(\frac{(h_o + \Delta)^2 + d_j^2}{h_o^2 + d_j^2} - 1 \right) \frac{h_o}{(h_o^2 + d_j^2)^{\frac{1}{2}}} \xi_j, \quad (4.2)$$

where E_f^Y is the Young's modulus of a micro-fiber and where (I) $d_j = d_o r_j$, $0 \leq r_j \leq 1$, (II) $\xi = 1$ if $U_j < U_{crit}$ and (III) $\xi = 0$ if $U_j \geq U_{crit}$ and where U_{crit} is a critical uniaxial stretch. This leads to

$$E_I^Y = \frac{E_f^Y h_o^3}{N_I} \sum_{j=1}^{N_I} \frac{1}{(h_o^2 + d_j^2)^{\frac{3}{2}}} \xi_j. \quad (4.3)$$

In the absence of damage ($\xi_j = 1 \forall j$), the effective modulus can be bounded from below by setting $r_j = 1 \forall j$ and above by setting $r_j = 0 \forall j$, resulting in

$$\frac{E_f^Y h_o^3}{(h_o^2 + d_o^2)^{\frac{3}{2}}} \leq E_I^Y \leq E_f^Y. \quad (4.4)$$

The upper bound is obvious, i. e. the overall yarn stiffness can never exceed the stiffness of perfectly aligned micro-fibers. The lower bound indicates the overall yarn stiffness decreases in a monotone fashion with increasing micro-fiber misalignment ($\mathcal{O}(d_o^{-3})$).

In order to illustrate the preceding results, the responses for 100 yarn of radii $r = 0.000185$ m and $h_o = 0.0007257$ m, each with a different random micro-fiber

realizations[†], are shown in Figure 3. In reality, the yarn are relatively flat, with an approximately elliptical cross-sectional area of aspect ratio of 4:1, which leads to a relatively large amount of misalignment. The mean, maximum and minimum for a population of 100 yarn, forming a constitutive “tube of uncertainty” is shown in Figure 4. Clearly, if one were to attempt to compute the response for an entire fabric represented by a network of yarn, typically having 35×35 yarn per square inch, by computing the relation in Equation 4.3 for each yarn, *each containing on the order of 350 micro-fibers*, the computations would be highly involved. *This is not necessary.* By first precomputing the mean, maximum and minimum for a population of yarn over the entire possible deformation range one can reconstruct a perturbed constitutive response “on the fly” for each yarn by a precomputed table lookup approach. One possible approach is to form a degradation function which not only takes into account the true modulus of the yarn due to misalignment, but also the progressive rupturing of the micro-fibers. The following degradation function is constructed

$$\begin{aligned}
 \theta_I \geq 0 &\Rightarrow \alpha_I(U) \stackrel{\text{def}}{=} \frac{E_I^Y(U)}{E_I^Y} = \frac{1}{E_I^Y} ((MAX(U) - MEAN(U)) \times \theta_I + MEAN(U)) \\
 \theta_I < 0 &\Rightarrow \alpha_I(U) \stackrel{\text{def}}{=} \frac{E_I^Y(U)}{E_I^Y} = \frac{1}{E_I^Y} ((MEAN(U) - MIN(U)) \times \theta_I + MEAN(U)),
 \end{aligned}
 \tag{4.5}$$

where $-1 \leq \theta_I \leq 1$ is a random variable, $MEAN(U)$ is the mean response of the tested population at stretch level U , $MAX(U)$ is the maximum response of the tested population at stretch level U and where $MIN(U)$ is the minimum response of

[†] According to the manufacturer (Toyobo [18]), each yarn contains 350 micro-fibers. Also, according to the manufacturer, for a micro-fiber, $U_{crit} = 1.03$.

the tested population at stretch level U . This construction insures that, statistically speaking, the mean response is $MEAN(U)$ (Figure 4).

(a) *Dynamics of the fiber net*

A lumped mass model is considered whereby at each node an equation for dynamic equilibrium is computed:

$$m\ddot{\mathbf{u}}_i = \sum_{I=1}^4 \mathbf{f}_I + \mathbf{P}_i, \quad (4.6)$$

where the four forces (\mathbf{f}_I) are the axial contributions of the four yarn intersecting at node i , m is the mass of a single lumped mass node (Figure 5), i.e. the total fabric mass divided by the total number of nodes and where \mathbf{P}_i is the contribution from the projectile (if the node is in contact with the projectile). The deformed cross-sectional area of a yarn is given by $J_I A_o L_o = A_I L_I \Rightarrow A_I = \frac{J_I A_o L_o}{L_I}$, and thus the forces in the current configuration can be computed by $\mathbf{f}_I = \sigma_I^a A_I \mathbf{a}_I = \frac{E_I^Y}{2} A_o (U_I^3 - U_I) \mathbf{a}_I$, where the axial yarn directions are given by $\mathbf{a}_I = \frac{\mathbf{r}_I^+ - \mathbf{r}_I^-}{\|\mathbf{r}_I^+ - \mathbf{r}_I^-\|}$, \mathbf{r}_I^+ and \mathbf{r}_I^- being the endpoints of the I th yarn.

(b) *Iterative solution procedure*

Consider the following iterative scheme for all nodes not in direct contact with the projectile $m\ddot{\mathbf{u}}_i^K = \sum_{I=1}^4 \mathbf{f}_I^{K-1}$, where i denotes the nodes, where I denotes the yarn and where $K = 1, 2, 3, \dots$ is an iteration counter. In other words, forces are first computed, then the displacements, then the forces are recomputed, etc. The case of nodes in direct contact with the projectile will be treated momentarily.

Using a finite difference approximation one has $\ddot{\mathbf{u}}_i^K(t + \delta t) \approx \frac{\mathbf{v}_i^K(t + \delta t) - \mathbf{v}_i^K(t)}{\delta t} \approx \frac{\mathbf{u}_i^K(t + \delta t) - \mathbf{u}_i^K(t)}{(\delta t)^2} - \frac{\mathbf{v}_i^K(t)}{\delta t}$, leading to

$$\mathbf{u}_i^K(t + \delta t) = \mathbf{u}_i(t) + \mathbf{v}_i(t)\delta t + \frac{(\delta t)^2}{m} \sum_{I=1}^4 \mathbf{f}_I^{K-1}. \quad (4.7)$$

For all nodes, at a given time step, the \mathbf{u}^K are computed until $\|\mathbf{u}_i^K(t + \delta t) - \mathbf{u}_i^{K-1}(t + \delta t)\| \leq TOL$.

(c) *Convergence*

Consider the general equation, $A(\mathbf{u}) = g(\mathbf{u})$. It is advantageous to write this in the form $A(\mathbf{u}) - g(\mathbf{u}) = G(\mathbf{u}) - \mathbf{u} + \mathbf{d} = \mathbf{0}$. A straightforward fixed point iterative scheme is to form

$$\mathbf{u}^K = G(\mathbf{u}^{K-1}) + \mathbf{d}. \quad (4.8)$$

The convergence of such a scheme is dependent on the characteristics of G . A sufficient condition for convergence is that G is a contraction mapping for all \mathbf{u}^K , $K = 1, 2, 3, \dots$. A necessary restriction for convergence is iterative self consistency, i. e. the exact solution must be reproduced by the scheme $G(\mathbf{u}) + \mathbf{d} = \mathbf{u}$. Defining the error vector as $\mathbf{e}^K = \mathbf{u}^K - \mathbf{u}$, and using the self consistency restriction, one has $\|\mathbf{e}^K\| = \|\mathbf{u}^K - \mathbf{u}\| = \|G(\mathbf{u}^{K-1}) - G(\mathbf{u})\| \leq \eta^K \|\mathbf{u}^{K-1} - \mathbf{u}\|$. Here, if $\eta^K < 1$ for each iteration K , then $\mathbf{e}^K \rightarrow \mathbf{0}$ for any arbitrary starting solution $\mathbf{u}^{K=0}$ as $K \rightarrow \infty$.

For the problem at hand, substituting Equation 4.8 to Equation 4.7, along with the fact that $\mathbf{f}_I = \frac{E_f^Y}{2} A_o (U_I^3 - U_I) \mathbf{a}_I$, one obtains $G(\mathbf{u}_i^K) \stackrel{\text{def}}{=} \frac{(\delta t)^2}{m} \sum_{I=1}^4 \mathbf{f}_I^K = \frac{E_f^Y A_o (\delta t)^2}{2m} \sum_{I=1}^4 \alpha_I^K ((U_I^K)^3 - U_I^K) \mathbf{a}_I^K$, and consequently

$$\eta^K \propto \frac{E_f^Y A_o (\delta t)^2}{2m}. \quad (4.9)$$

The rates of convergence of the iterative scheme are controlled by adapting the time step sizes in order to restrict η^K . This is discussed, in an algorithmic context, later.

(d) *Projectile/fabric interaction*

In order to simplify the problem somewhat, it is assumed that the projectile is rigid and has only one velocity component, orthogonal to the fabric in the z -direction (Figure 6). The velocity, directly after initial contact, can be computed from a balance of momentum in the z -direction, $m_p v^o = m_p v_{pz} + m_f^C v_f$, which implies $v_{pz} = \frac{m_p}{m_p + m_f^C} v^o$, where all external forces are zero due to the fact that, *initially*, the fabric is unstretched. Here m_p is the mass of the projectile, v^o is the incoming velocity of the projectile, v_{pz} is the velocity of the projectile directly after initial contact, v_f is the velocity of the fabric material in the contact zone directly after initial contact and m_f^C represents the mass of the fabric in the contact zone. All nodes that are underneath the projectile are restricted to have the same z -component of velocity as the projectile, however, they may slide, in a frictionless manner, in any other direction. As time progresses, when the projectile and fabric are in contact, one has a work-energy relation

$$\begin{aligned}
 & \underbrace{\frac{1}{2} m_p \mathbf{v}_p(t) \cdot \mathbf{v}_p(t)}_{\text{projectile kinetic energy}} + \underbrace{\sum_{i=1}^N \frac{1}{2} m \mathbf{v}_i(t) \cdot \mathbf{v}_i(t)}_{\text{fabric kinetic energy}} - \underbrace{\sum_{I=1}^F A_o L_o \int_{E_{I11}(t)}^{E_{I11}(t+\delta t)} E_I^Y(t+\delta t) E_{I11}(t+\delta t) dE_{I11}}_{\text{work done by yarn}} \\
 & = \underbrace{\frac{1}{2} m_p \mathbf{v}_p(t+\delta t) \cdot \mathbf{v}_p(t+\delta t)}_{\text{projectile kinetic energy}} + \underbrace{\sum_{i=1}^N \frac{1}{2} m \mathbf{v}_i(t+\delta t) \cdot \mathbf{v}_i(t+\delta t)}_{\text{fabric kinetic energy}}.
 \end{aligned} \tag{4.10}$$

Noting that $\mathbf{v}_p \cdot \mathbf{v}_p = v_{pz}^2$ and writing $v_{pz}(t+\delta t) = \frac{u_{pz}(t+\delta t) - u_{pz}(t)}{\delta t}$ one obtains the following

$$u_{pz}^K(t + \delta t) = u_{pz}(t) + \delta t(v_{pz}^2(t) - \frac{2}{m_p} \sum_{I=1}^F A_o L_o \int_{E_{I11}(t)}^{E_{I11}^{K-1}(t+\delta t)} E_I^{Y,K-1}(t + \delta t) E_{I11}^{K-1}(t + \delta t) dE_{I11} \quad (4.11)$$

$$+ \frac{m}{m_p} \sum_{i=1}^N \mathbf{v}_i(t) \cdot \mathbf{v}_i(t) - \frac{m}{m_p} \sum_{i=1}^N \mathbf{v}_i^{K-1}(t + \delta t) \cdot \mathbf{v}_i^{K-1}(t + \delta t)) \frac{1}{2}.$$

Furthermore, for all nodes in direct contact with the projectile, $u_{iz} = u_{pz}$ at all times. One obtains the solution of this problem with a fixed-point iteration, which is embedded into an overall solution process involving simultaneous nodal iteration, which is as follows:

(*) FOR A SHEET/PROJECTILE PAIR : $v_{pz} = \frac{m_p}{m_p + m_f} v^o$

STEP 0 : STARTING TIME STEP VALUE : $\delta t = \delta t_{DISCRETE}$

STEP I : SOLVE FOR DISPLACEMENTS VIA EQUILIBRIUM : ($K = K + 1$)

FOR NODES IN THE CONTACT ZONE :

$$\begin{aligned} u_{ix}^K(t + \delta t) &= u_{ix}(t) + v_{ix}(t)\delta t + \frac{(\delta t)^2}{m} \sum_{I=1}^4 f_{Ix}^{K-1} \\ u_{iy}^K(t + \delta t) &= u_{iy}(t) + v_{iy}(t)\delta t + \frac{(\delta t)^2}{m} \sum_{I=1}^4 f_{Iy}^{K-1} \\ u_{iz}^K(t + \delta t) &= u_{pz}^{K-1}(t + \delta t) \end{aligned}$$

FOR NODES NOT IN THE CONTACT ZONE : $\mathbf{u}_i^K(t + \delta t) = \mathbf{u}_i(t) + \mathbf{v}_i(t)\delta t + \frac{(\delta t)^2}{m} \sum_{I=1}^4 \mathbf{f}_I^{K-1}$

STEP II : SOLVE FOR AXIAL CAUCHY STRESSES : $\sigma_I^{a,K} = \frac{1}{J_I^K} (U_{I11}^K)^2 S_{I11}^K$

STEP III : COMPUTE DAMAGE IN EACH YARN AND THE SUBSEQUENT STIFFNESS : $E_I^{Y,K}$

STEP IV : COMPUTE PROJECTILE POSITION :

$$\begin{aligned} u_{pz}^K(t + \delta t) &= u_{pz}(t) + \delta t(v_{pz}^2(t) \\ &\quad - \frac{2}{m_p} \sum_{I=1}^F A_o L_o \int_{E_{I11}(t)}^{E_{I11}^{K-1}(t+\delta t)} E_I^{Y,K-1}(t + \delta t) E_{I11}^{K-1}(t + \delta t) dE_{I11} \quad (4.12) \\ &\quad + \frac{m}{m_p} \sum_{i=1}^N \mathbf{v}_i(t) \cdot \mathbf{v}_i(t) - \frac{m}{m_p} \sum_{i=1}^N \mathbf{v}_i^{K-1}(t + \delta t) \cdot \mathbf{v}_i^{K-1}(t + \delta t)) \frac{1}{2} \end{aligned}$$

STEP V : ERROR CHECK :

$$(1) \|e^K\| \stackrel{\text{def}}{=} \frac{\sum_{i=1}^n \|\mathbf{u}_i^K(t + \delta t) - \mathbf{u}_i^{K-1}(t + \delta t)\|}{\sum_{i=1}^n \|\mathbf{u}_i^K(t + \delta t)\|}$$

$$(2) \xi^K \stackrel{\text{def}}{=} \frac{\|e^K\|}{TOL}$$

IF TOLERANCE MET ($\xi^K \leq 1$) AND $K < K_d$ THEN :

- (1) IF PENETRATION OCCURS GO TO NEXT SHEET(*) WITH $v^o = v_{pz}(t + \delta t)$
- (2) STEP TIME : $t = t + \delta t$ AND GO TO STEP I WITH $K = 0$ AND $\delta t = \delta t_{DISCRETE}$

$(\delta t_{DISCRETE} = \text{UPPER TIME STEP DISCRETIZATION SIZE LIMIT})$

IF TOLERANCE NOT MET ($\xi^K > 1$) AND $K = K_d$ THEN :

- (1) STEP BACK : $t = t - \delta t$
- (2) CONSTRUCT NEW TIME STEP : $\delta t = \frac{\delta t}{\xi^K}$
- (3) RESTART AT TIME STEP t AND GO TO STEP I $K = 0$

The overall goal is to deliver accurate solutions where the temporal discretization accuracy dictates the upper limits on the time step size ($\delta t^{DISCRETE}$), while the strategy in Box 4.12 refines the step size further to control the iterative error, if needed. For a related treatment for non-stochastic models employing damage evolution laws see Zohdi [21].

5. Numerical simulations

As in the laboratory experiments, a 50 caliber, 0.0127 m (0.5 inch) in diameter, 0.036 kg cylindrical projectile initially traveling at 152 m/s which struck in the center of the (square) target, was considered. The fabric was square of dimensions 0.254×0.254 meters (10×10 inches) with 35×35 yarn per square inch, thus leading to 350×350 yarn. Consequently 350×350 lumped mass nodes and $3 \times 350 \times 350 = 367500$ degrees of freedom (unknowns) were needed for the computations. Penetration was said to occur if the material directly underneath the projectile (in the contact zone) degraded to 50% of its original stiffness (50% damage), $\langle \frac{E^Y(t)}{E^Y(t=0)} \rangle_{\omega_p} = 0.5 = \frac{1}{|\omega_p|} \int_{\omega_p} \frac{E^Y(t)}{E^Y(t=0)} d\omega_p$. The tests were repeatedly rerun for different realizations of the micro-fiber misalignment within the yarn until the ensemble average of the macroscopic responses (the number of ballistic sheets needed to stop the projectile) stabilized. Ten tests were initially carried out before a termination criteria was checked to ensure statistical representativeness. The termination criteria was that the ensemble average should not vary by more than one-half of a percent. For the various realizations, a maximum of 12 ballistic sheets and a minimum of 11 ballistic sheets were needed throughout the tests. A total of 13 realizations were needed until

the ensemble average stabilized (seven 12 sheet cases resulted and six 11 sheet cases resulted, Figure 7). The average was 11.538 ballistic sheets. It is interesting to note that the variation in the individual responses of the yarn shown in Figure 3 are on the order of nine percent, which in turn leads to approximately a nine percent variation in the ballistic limit. However, an expression for the amount of variation in the macroscopic ballistic limit of the fabric as a whole, as a function of the micro-fiber misalignment, is currently lacking and may be impossible to ascertain a-priori. The set of velocity-sheet curves (13 realizations) are shown in Figure 8 for the first 11 ballistic sheets. As indicated earlier, laboratory experiments indicate that between 11 and 12 ballistic sheets of Zylon are needed to stop a projectile.

6. Concluding remarks

A critical feature of the model is the incorporation of microscale uncertainty, due to micro-fiber misalignment, in the response function. The effects of the constitutive “noise”, which can be represented in a constitutive tube of uncertainty, automatically ascertain the limits of what can be measured (scatter) in actual laboratory experiments. This is a natural outcome of the multiscale model. Finally, we remark that for increasing incoming projectile speeds, the difference in the responses between various multilayered ballistic sheet realizations increases. However, from our ongoing experimental and numerical studies, at higher speeds, the percent of variation with respect to the mean seems to remain virtually constant. In other words, hypothetically, if it took an average of 110 sheets to stop a projectile at some higher speed, then the amount of variation would be approximately ± 10 sheets. However,

our tests at higher speeds are still under investigation, both experimentally and numerically, and such comments should be taken qualitatively.

7. References

1. Atai, A. A. and Steigmann, D. J. (1997). On the nonlinear mechanics of discrete networks. *Archive of Applied Mechanics*. **67**, 303-319.
2. Atai, A. A. and Steigmann, D. J. (1998). Coupled deformations of elastic curves and surfaces. *Int. J. Solids Structures*. **35**, No. 16, 1915-1952.
3. Buchholdt, H. A. Davies, M. Hussey, M. J. L. (1968). The analysis of cable nets. *J. Inst. Maths. Applics*. **4** 339-358.
4. Buler, H. and Nguyen-Tuong, B. (1980). On the work theorems in nonlinear network theory. *Ing. Arch*. **49** 275-286.
5. Cannarozzi, M. (1985). Stationary and extremum variational formulations for the elastostatics of cable networks. *Meccanica*. **20** 136-143.
6. Cannarozzi, M. (1987). A minimum principle for tractions in the elastostatics of cable networks. *Int. J. Solids Struct.* **23**, 551-568.
7. Haseganu, E. M. and Steigmann, D. J. (1994). Analysis of partly wrinkled membranes by the method of dynamic relaxation. *Computational Mechanics*. **14**, 596-614.
8. Haseganu, E. M. and Steigmann, D. J. (1994). Theoretical flexural response of a pressurized cylindrical membrane. *Int. J. Solids Struct.* **31** 27-50.
9. Haseganu, E. M. and Steigmann, D. J. (1996). Equilibrium analysis of finitely deformed elastic networks. *Computational Mechanics*. **17**, 359-373.
10. Johnson, G. R., Beissel, S. R., and Cunniff, P. M. (1999). A computational model for fabrics subjected to ballistic impact. In *Proceedings of the 18th international symposium on ballistics*, San Antonio, TX, 962-969.
11. Kollegal, M. G. and Sridharan, S. (2000). Strength prediction of plain woven fabrics. *Journal of Composite Materials*. **34**, 240-257.
12. Pangiotopoulos, P. D. (1976). A variational inequality approach to the inelastic stress-unilateral analysis of cable structures. *Comput. Struct.* 1976, **6** 133-139.
13. Pipkin, A. C. (1986). The relaxed energy density for isotropic elastic membranes. *IMA Journal of Applied Mathematics*. **36**, 297-308.
14. Roylance, D. and Wang, S. S. (1980). *Penetration mechanics of textile structures, ballistic materials and penetration mechanics*, 273-293, Elsevier.
15. Shim, V. P., Tan, V. B. C. and Tay, T. E. (1995). Modelling deformation and damage characteristics of woven fabric under small projectile impact. *Int. J. Impact Engng*. **16**, 585-605.

16. Tabiei, A. and Jiang, Y. (1999). Woven fabric composite material model with material nonlinearity for finite element simulation. *Int. J. of Solids and Structures*. **36**, 2757-2771.
17. Taylor, W. J. and Vinson J. R. (1990). Modelling ballistic impact into flexible materials. *AIAA Journal*, **28**, 2098-2103.
18. Toyobo. (2001). PBO fiber ZYLON. Report of the Toyobo Corporation, LTD, www.toyobo.co.jp.
19. Walker, J. D. (1999). Constitutive model for fabrics with explicit static solution and ballistic limit. In *Proceedings of the 18th international symposium on ballistics*, San Antonio, TX, 1231-1238.
20. Zohdi, T. I. and Steigmann, D. J. (2002). The toughening effect of microscopic filament misalignment on macroscopic fabric response. *The International Journal of Fracture*. **115**, L9-L14.
21. Zohdi, T. I. (2002). Modeling and simulation of progressive penetration of multilayered ballistic fabric shielding. *Computational Mechanics*. **29**, 61-67.

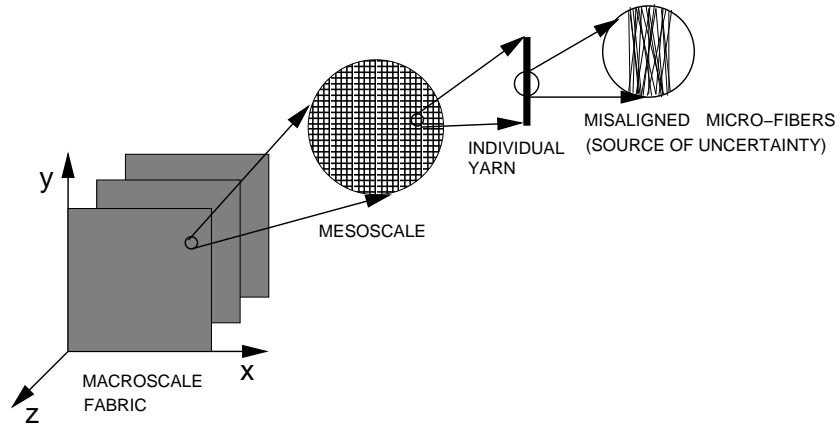


Figure 1. Multiple scales in a ballistic fabric.

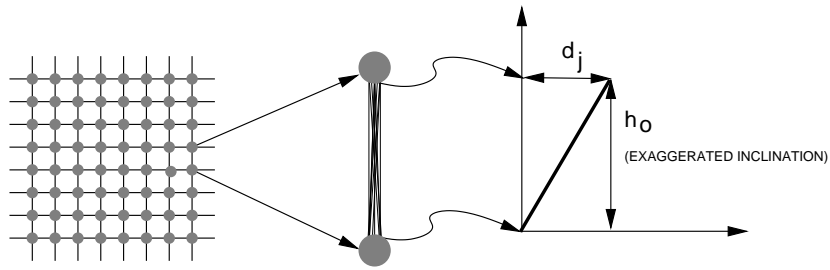


Figure 2. A zoom on an individual misaligned micro-fiber.

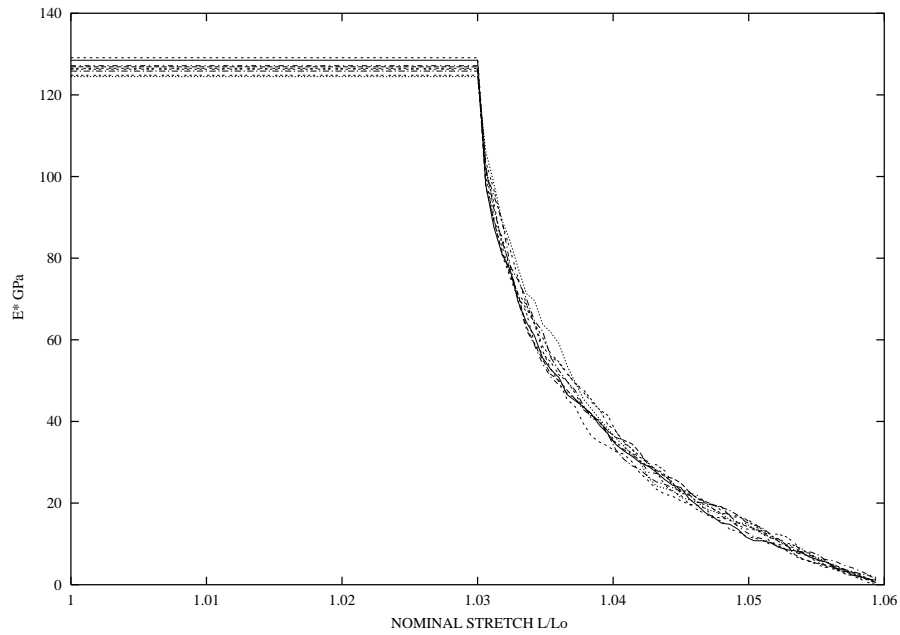
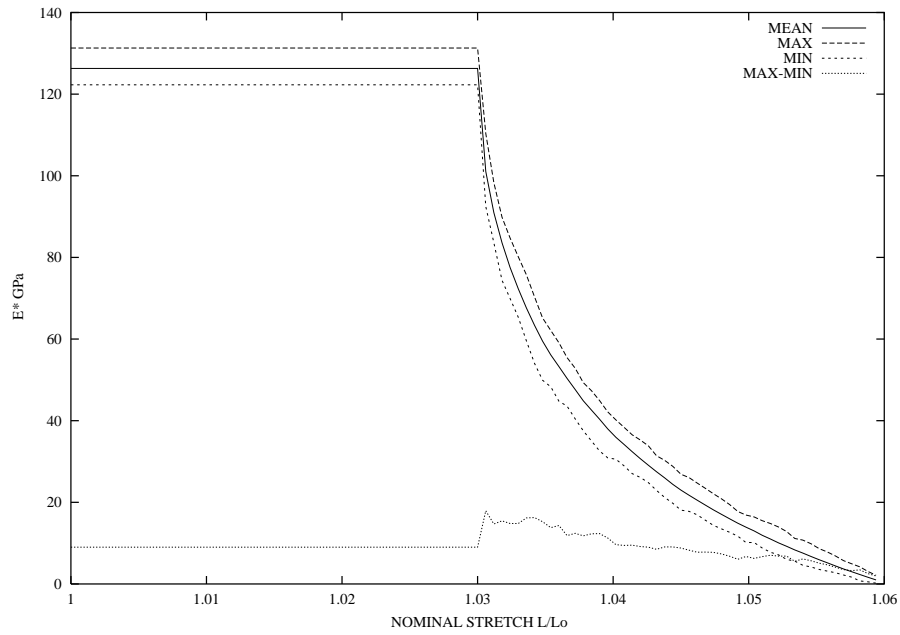


Figure 3. TOP: A tube of constitutive variation in the degradation of 100 different yarn responses. BOTTOM: The degrading material moduli for 10 of the 100 different yarn.

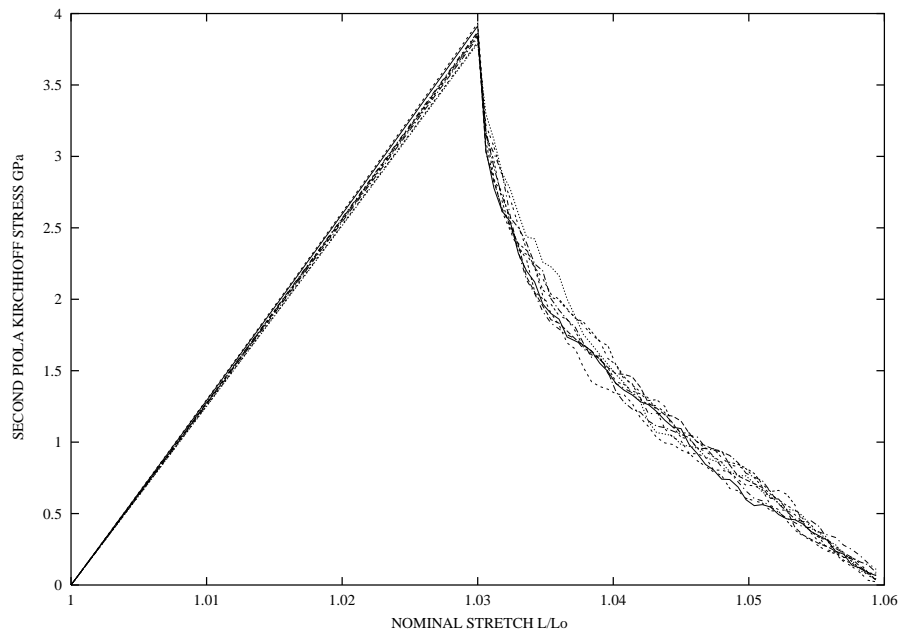
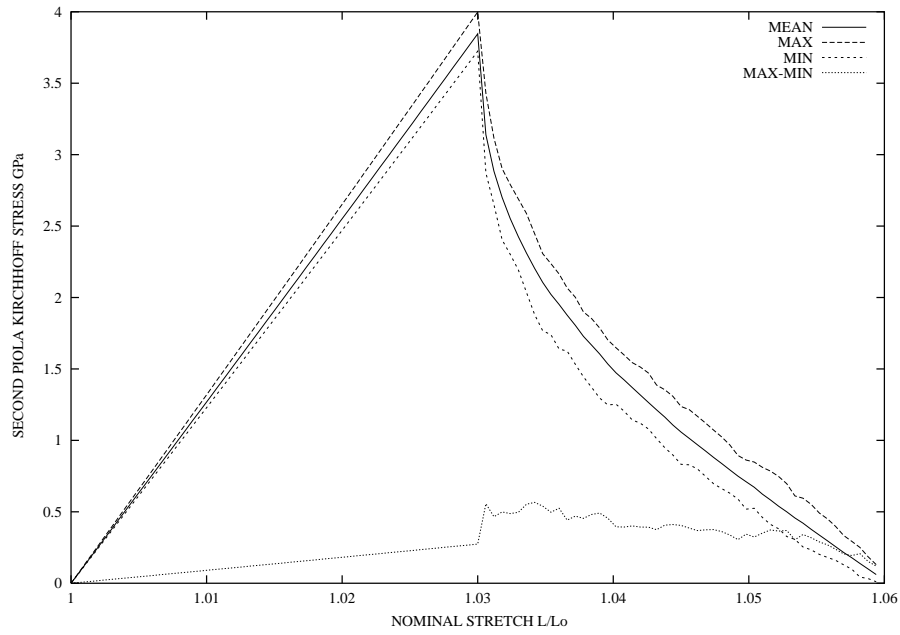


Figure 4. TOP: A tube of constitutive variation in the second Piola-Kirchhoff stress responses of 100 different yarn. BOTTOM: The second Piola-Kirchhoff stress responses for 10 of the 100 different yarn.

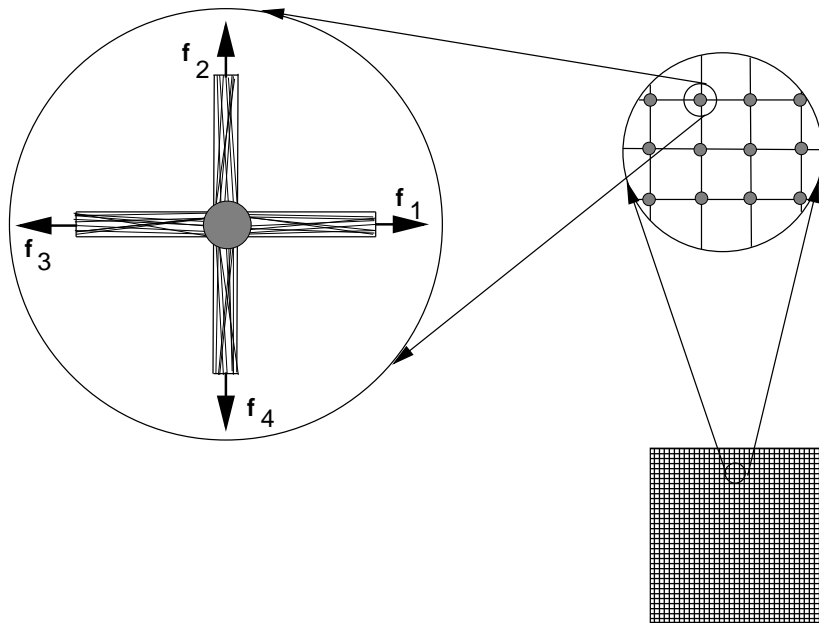


Figure 5. Four yarn intersecting at a lumped mass.

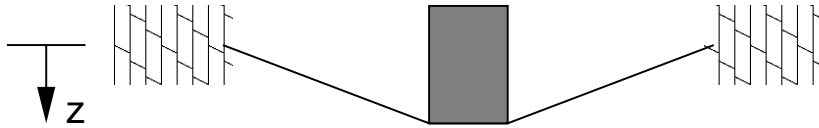


Figure 6. A side view of a projectile-fabric pair.

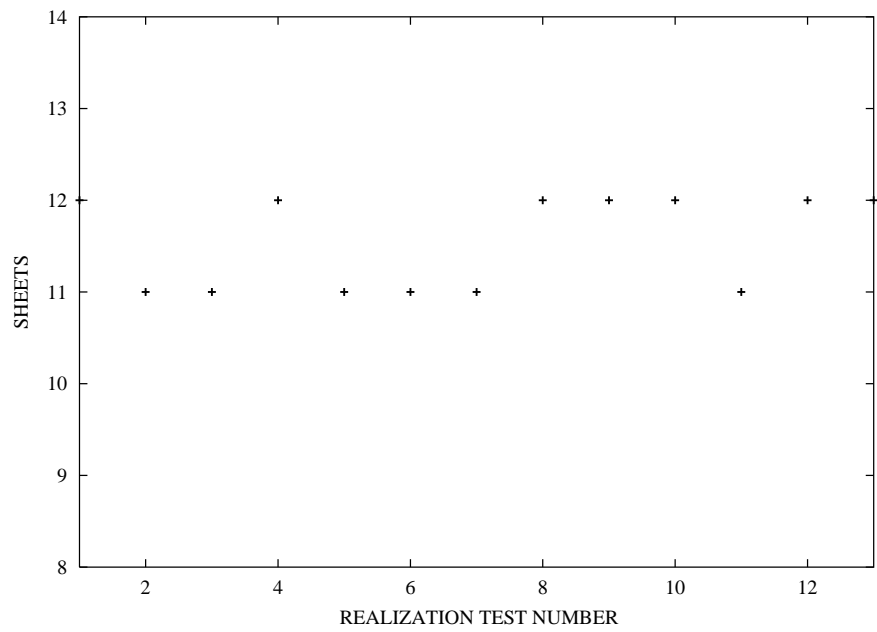


Figure 7. The number of ballistic sheets needed to stop a projectile for 13 different realizations.

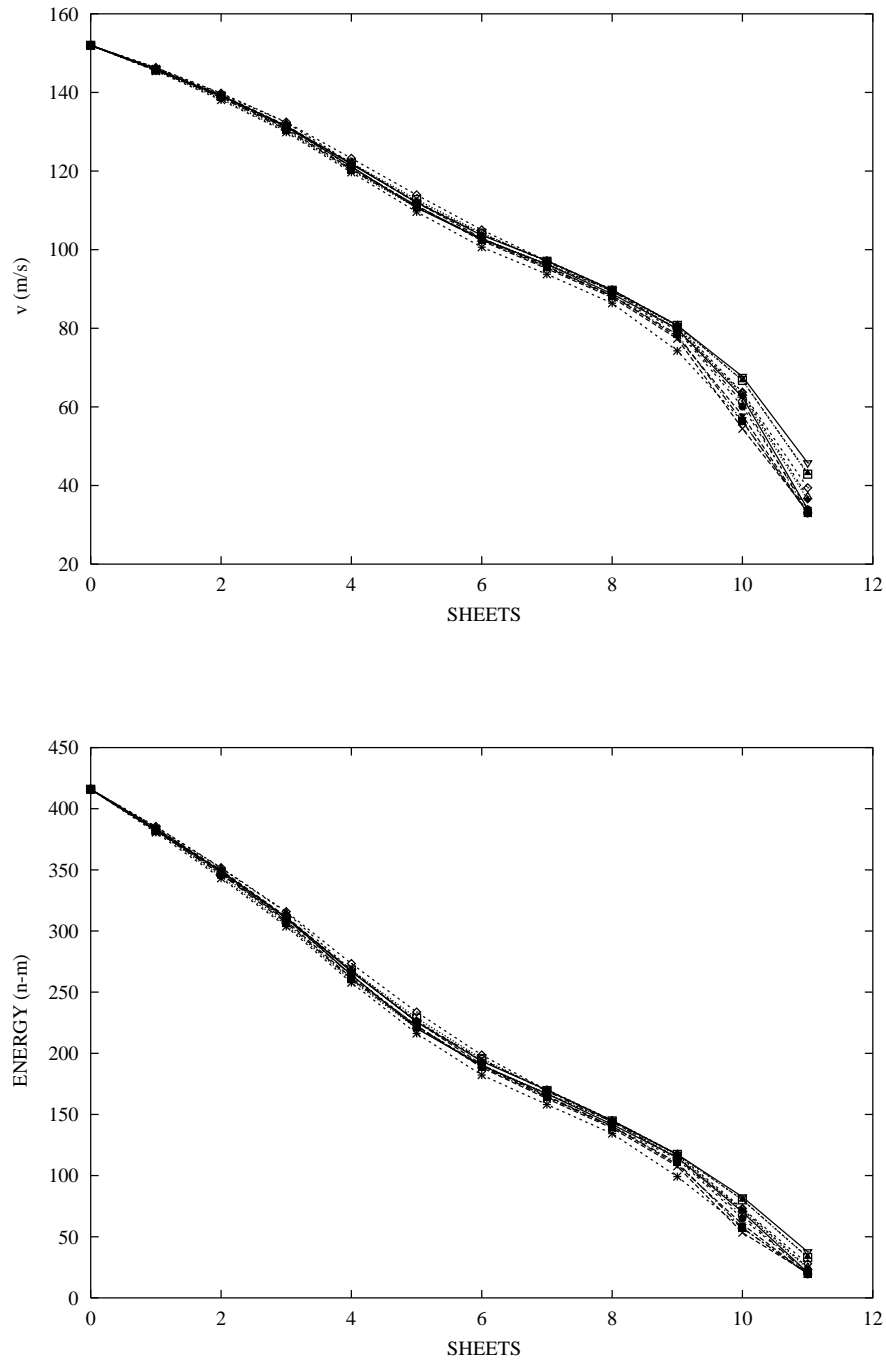


Figure 8. TOP: The projectile velocities as a function of the number of ballistic sheets penetrated for 13 different realizations. BOTTOM: The projectile energy as a function of the number of ballistic sheets penetrated.

APPENDIX B—LIGHTWEIGHT BALLISTIC PROTECTION OF FLIGHT-CRITICAL
COMPONENTS ON COMMERCIAL AIRCRAFT

PLAN FOR BALLISTIC TESTING OF ZYLON FABRIC

Written by

Jerry Farstad and Jennifer Zielinski
The Boeing Company
Seattle, WA 98124

TABLE OF CONTENTS

	Page
EXECUTIVE SUMMARY	v
B1. INTRODUCTION AND BACKGROUND.	1
B2. SMALL-SCALE LABORATORY TESTS OF ZYLON FABRIC BALLISTIC PERFORMANCE	1
B3. LARGE SCALE (AIRPLANE SIZE) TESTS OF ZYLON FABRIC BALLISTIC PERFORMANCE.	7
B4. CONCLUSION	10

LIST OF FIGURES

Figure	Page
FIGURE B1.	Schematic for small scale laboratory test of Zylon fabric ballistic properties: bare fabric targets with clamped edge conditions.
FIGURE B2.	Schematic for small-scale laboratory test of Zylon fabric ballistic properties: bare fabric targets with edges constrained by discrete fasteners.
FIGURE B3.	Schematic for small-scale laboratory test of Zylon fabric ballistic properties: aluminum sheet and Zylon fabric targets with clamped edge conditions.
FIGURE B4.	Schematic for small scale laboratory test of Zylon fabric ballistic properties: Multiple simultaneous projectiles with clamped edge conditions.
FIGURE B5.	Schematic for airplane scale test of Zylon fabric ballistic properties: aluminum sheet and zylon fabric targets attached to ladder frame similar to commercial airplane fuselage structure.
FIGURE B6.	Schematic for airplane scale test of Zylon fabric ballistic properties: aluminum sheet and zylon fabric targets attached to steel frame similar to commercial airplane fan cowl structure.
FIGURE B7.	Schematic for airplane scale test of Zylon fabric ballistic properties: Zylon fabric shield installed of salvaged transport airplane fuselage section.

EXECUTIVE SUMMARY

In support of the joint effort among The University of California, Boeing, and SRI International to evaluate the use of Zylon fabric for engine rotor burst debris shields on commercial transport aircraft, Boeing designed a series of ballistic tests intended to evaluate the ballistic performance of Zylon fabric for airplane engine rotor burst shielding. The tests were executed by the University of California (small-scale laboratory tests) and SRI International (large-scale (airplane size) tests). This appendix contains the initial test plan for both of these tests. This part of the FAA report contains the results of the airplane scale tests.

Two series of tests were designed. One series focused on small-scale tests intended to provide a significant number data points for relatively simple test configurations conducted in a laboratory environment. In these tests 10 in. x 10 in. (254 mm x 254 mm) Zylon targets and 0.50 in. (12.7 mm) diameter cylindrical projectiles were used. Several different attachment conditions at the edges of the targets were considered. Projectile velocities in the range of 500-1000 ft/sec (153-305 m/sec) were specified. Results of the small-scale tests are included in this part of this FAA report.

The second set of tests focused on test articles on the scale of commercial airplane structure and rotor burst shields. Targets consisted of Zylon fabric and aluminum sheets of thickness similar to commercial airplane skins. The targets were mounted on relatively rigid steel frame structures with spacing between members similar to that of frames and stringers in modern commercial airplanes. Projectiles were designed to be representative of engine debris liberated by a rotor burst event. Two fragments were used. The smaller was a 2.0 in. x 2.0 in. x 0.25 in. (50.8 mm x 50.8 mm x 6.4 mm) rectangular parallelepiped made from steel and intended to be similar in size and mass to a high pressure turbine blade. The larger fragment was a 4.0 in. x 4.0 in. x 0.50 in. (101.6 mm x 101.6 mm x 12.7 mm) rectangular parallelepiped made from steel which was intended to be similar in size and mass to a partial fan blade fragment. The smaller projectiles were specified to have incident velocities in the range of 500-1000 ft/sec (153-305 m/sec), and the larger fragments were specified to have velocities in the range of 400-700 ft/sec (122 – 214 m/sec). These velocities are typical of engine rotor burst debris fragments. Results of the large-scale aircraft size ballistic tests are included in part 2 of this FAA report.

B1. INTRODUCTION AND BACKGROUND.

The overall purpose of this effort was to evaluate the use of Zylon fabric for engine rotor burst debris shields on commercial transport aircraft. The Boeing effort was to independently evaluate Zylon material properties and to determine the effect of typical aircraft environments on Zylon fibers and to design a series of tests to evaluate the ballistic performance of Zylon fabric for airplane engine rotor burst shielding. This appendix describes the series of ballistic experiments designed. The results of the Zylon material property evaluation conducted by Boeing appear in part 3 of this FAA report.

B2. SMALL-SCALE LABORATORY TESTS OF ZYLON FABRIC BALLISTIC PERFORMANCE.

Two sets of tests were designed to experimentally evaluate the ballistic performance of Zylon fabric for transport airplane rotor burst shielding applications, one of which was described in this Section. Small-scale ballistic tests were designed to permit the ballistic properties of Zylon fabric targets to be evaluated from a relatively large number of experiments in a controlled laboratory setting. This series of experiments was designed to be conducted in the Gun Laboratory of the Department of Mechanical Engineering of the University of California at Berkeley, and the experiments were designed to make use of existing equipment in the laboratory. For this reason, 0.50 in. (12.7 mm) cylindrical projectiles used in this series of tests, as a smooth barrel 0.50 caliber powder gun was available. The projectiles were machined from steel and clad with copper to avoid damage to the gun barrel. Their mass was 0.083 lb (37.2 g). The projectiles were incident upon the targets with velocities of 500-1000 ft/sec (153-305 m/sec), which are typical of debris fragments liberated by transport airplane engine rotor burst events. Normal and oblique angles of incidence were specified.

Four series of targets were proposed. The first series consisted of square 10 in. x 10 in. (254 mm x 254 mm) bare fabric targets as indicated in figure B1. The fabric targets were to be held in a frame-like fixture that would ensure that all four edges of the target remained nearly fixed during impact with the projectiles. Targets were to be installed without slack in the fabric. The projectiles were to impact the target at locations in the center of the targets and at locations closer to a corner, as indicated in figure B1. Several thicknesses of Zylon fabric were to be tested as targets. It was intended that for each target thickness projectiles with a range of incident velocities would be used, so that performance of the target at projectile velocities above and below the ballistic limit for that target/projectile pair could be measured. In addition, targets of Kevlar fabric were to be tested as well to provide an indication of the relative ballistic performance of Zylon and Kevlar fabrics.

The second series of laboratory tests is shown schematically in figure B2. This series of tests was designed to be similar to those of figure B1 except for the way that the fabric targets were to be attached to the target holders. In this series of tests, the fabric target was to be attached to the target holder at discrete locations by bolts and washers. Cases of four attachment points at the corners of the target holder and eight attachment points at the corners and mid points of the sides of the target holder were specified, as indicated in figure B2. The targets in this series of tests were to be bare Zylon fabric. Impact points at the center of the target and near one of its corners are specified, as indicated in figure B2. The projectile and incident velocities specified are similar to those specified for the previous test series with clamped fabric edge conditions.

The third series of laboratory tests specified is shown in figure B3. This series of tests is similar to those shown in figure B1 except that the target consists of aluminum sheet in addition to Zylon fabric. The objective of this test series is to determine if the reinforcement of the aluminum sheet by the Zylon fabric would result in greater shielding performance than one would expect from the aluminum sheet and the Zylon fabric without any interaction. For this reason, the spacing between the aluminum sheet and the Zylon fabric is variable, as indicated in figure A3. Like the test series of figure B1, clamped edge conditions were to be imposed on the

fabric and aluminum sheet by the target holder. The projectile and incidence conditions specified were similar to those of the previous two small-scale test series.

The fourth series of small-scale ballistic tests was intended to determine the ballistic performance of Zylon fabric under simultaneous impacts by multiple projectiles. The test configuration is shown in figure B4. Targets were specified to be 10 in. x 10 in. (254 mm x 254 mm) bare Zylon fabric held in target holders imposing clamped edge conditions similar to those used in the test series of figure B1. Projectiles were specified to be spherical buckshot fired simultaneously from a shotgun arrangement. Projectile velocities in the range of 500-1000 ft/sec (153-305 m/sec) were specified. Incidence was specified to be normal to the target with the centroid of the projectile group nominally located at the target center.

For all cases of target configuration and projectile incidence conditions it was expected that experiments would be repeated one time or more to permit some measure of uncertainty in the experimental results. In this case test configurations of figures B3 and B4 were not completed due to resource limitations, and an additional test series with clamped conditions on two sides similar to that of figure B1 was conducted.

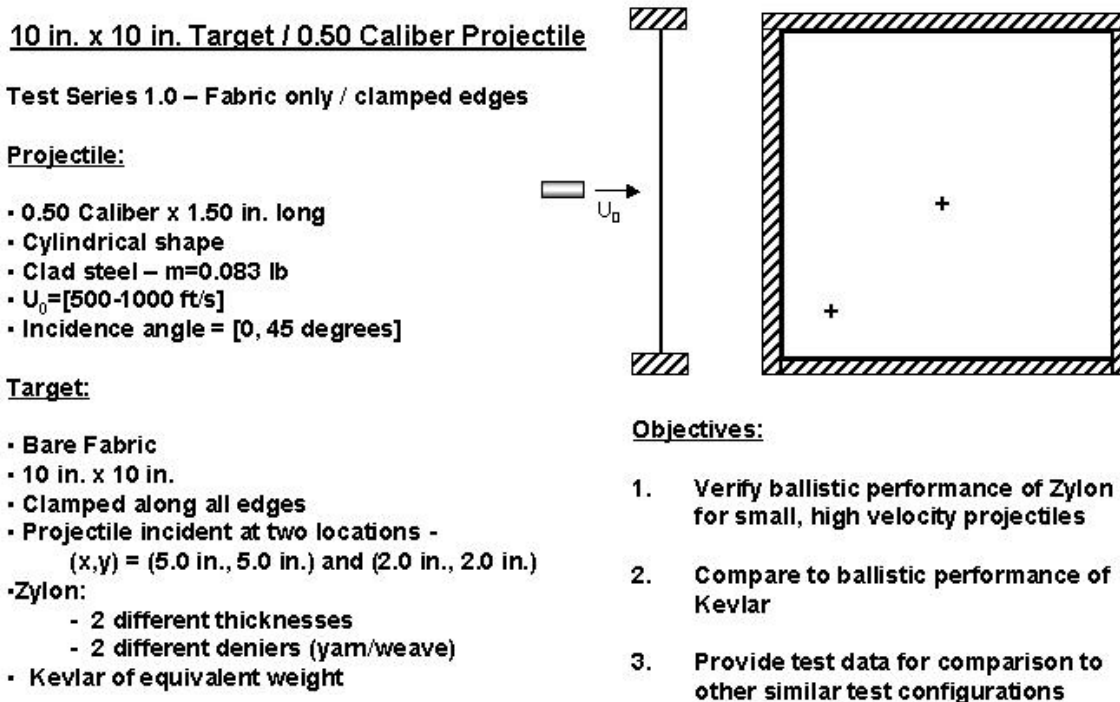


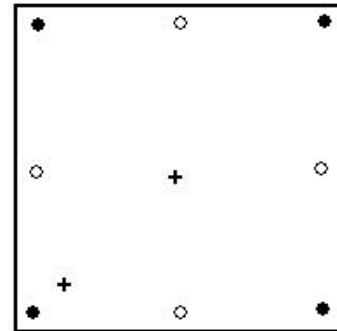
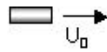
Figure B1. Schematic for small-scale laboratory test of Zylon fabric ballistic properties: bare fabric targets with clamped edge conditions.

10 in. x 10 in. Target / 0.50 Caliber Projectile

Test Series 2.0 – Fabric only / bolted edges

Projectile:

- 0.50 Caliber x 1.50 in. long
- Cylindrical shape
- Clad steel – $m=0.083$ lb
- $U_0=[500-1000$ ft/s]
- Incidence angle = [0, 45 degrees]



Target:

- Bare Fabric
- 10 in. x 10 in.
- Bolted at 4 – 8 discrete locations (with washers)
- Projectile incident at two locations -
(x,y) = (5.0 in., 5.0 in.) and (2.0 in., 2.0 in.)
- Zylon:
 - 2 different thicknesses

Objectives:

1. Determine effect of fabric edge conditions on relative ballistic performance of Zylon shields

Figure B2. Schematic for small-scale laboratory test of Zylon fabric ballistic properties: bare fabric targets with edges constrained by discrete fasteners.

10 in. x 10 in. Target / 0.50 Caliber Projectile

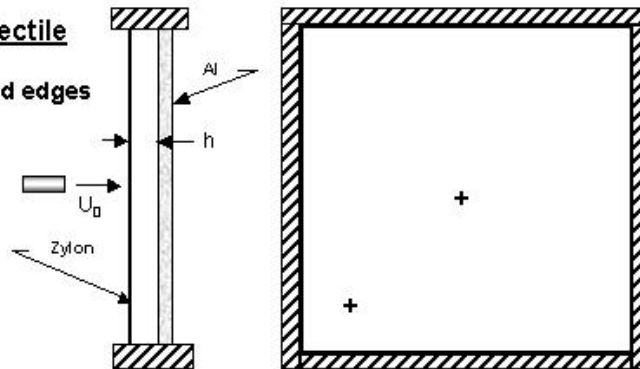
Test Series 3.0 – Aluminum + Zylon / clamped edges

Projectile:

- 0.50 Caliber x 1.50 in. long
- Cylindrical shape
- Clad steel – $m=0.083$ lb
- $U_0=[500-1000$ ft/s]
- Incidence angle = $[0, 45$ degrees]

Target:

- Aluminum (2024-T4) sheet / Zylon fabric shield
- 10 in. x 10 in. - Clamped along all edges
- Cases of Zylon before Al and Zylon after Al to be considered
- Projectile incident at two locations - $(x,y) = (5.0$ in., 5.0 in.) and $(2.0$ in., 2.0 in.)
- Zylon - 2 different thicknesses
- Aluminum – 2 different thicknesses
- Spacing $h = [0, 0.5$ in.]



Objectives:

1. Determine effect of interaction of Zylon with adjacent metal structure on ballistic performance of Zylon fabric shields – small, high velocity projectiles
2. Investigate both shielding and containment configurations

Figure B3. Schematic for small-scale laboratory test of Zylon fabric ballistic properties: aluminum sheet and Zylon fabric targets with clamped edge conditions.

10 in. x 10 in. Target / Multiple Small Projectiles

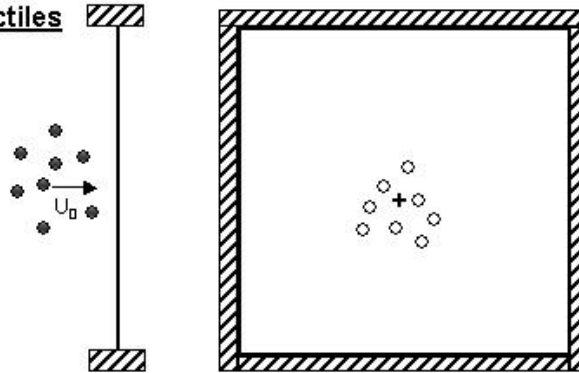
Test Series 4.0 – Multiple fragment study

Projectiles:

- Buckshot – size?
- Spherical shape
- Clad lead – m=? lb
- U_0 =[500-1000 ft/s]
- Normal incidence
- Single and multiple shot cases for each U_0

Target:

- Bare Zylon Fabric
- 10 in. x 10 in.
- Clamped along all edges
- Projectile group incident on center of target
- 2-3 different fabric thicknesses



Objectives:

1. Determine ballistic performance of Zylon for multiple impact by small, high velocity projectiles
2. Provide verification for LS-DYNA3D analysis of multiple impact events with HPT/HPC blade fragments

Figure B4. Schematic for small-scale laboratory test of Zylon fabric ballistic properties: Multiple simultaneous projectiles with clamped edge conditions.

B3. LARGE SCALE (AIRPLANE SIZE) TESTS OF ZYLON FABRIC BALLISTIC PERFORMANCE.

The set of tests described in this Section was intended to resemble possible installations of Zylon fabric on transport airplanes for rotor burst debris shielding. These experiments were designed to be conducted by SRI International at their 6 in. (152.4 mm) gas gun range. Two projectiles were specified for use in these tests. The smaller was a 2.0 in. x 2.0 in. x 0.25 in. (50.8 mm x 50.8 mm x 6.4 mm) rectangular parallelepiped made from steel and intended to be similar in size and mass to a high pressure turbine blade. The larger fragment was a 4.0 in. x 4.0 in. x 0.50 in. (101.6 mm x 101.6 mm x 12.7 mm) rectangular parallelepiped made from steel which was intended to be similar in size and mass to a partial fan blade fragment. The smaller projectiles were specified to have incident velocities in the range of 500-1000 ft/sec (153-305 m/sec), and the larger fragments were specified to have velocities in the range of 400-700 ft/sec (122 – 214 m/sec). Only normal incidence conditions were specified for the airplane-scale tests.

The configuration specified for the first series of airplane-scale experiments is indicated in figure B5. The targets for these tests consisted of Zylon fabric and aluminum sheet metal attached to a steel ladder frame by bolts and washers. The ladder frame arrangement was intended to have spacing between horizontal and vertical members similar to the spacing between frames and stringers in typical commercial airplane fuselage structures. The ladder frame was to be designed such that it would not yield under the loads imposed by impact with the projectiles so that it could be re-used in subsequent tests. The aluminum sheet was to be placed in front of the Zylon fabric, like the small-scale experiments of figure B3. Unlike those experiments, test cases involving targets with Zylon fabric only were specified. Cases of projectile velocities resulting in penetration and non-penetration were specified for both projectiles.

The configuration for another series of airplane-scale tests is shown in figure B6. These tests were intended to be similar to a possible installation of Zylon fabric on the interior of an airplane engine fan cowl. The test configuration involved Zylon fabric and aluminum sheet attached to vertical steel frame sections by bolts and washers. In addition, bolts and washers between the fabric and aluminum sheet were specified at a grid of so-called “field” points between the support frames. Like the ladder frame test series, the steel support members were specified to be such that they would not experience plastic deformation during the tests. Again, cases of projectile velocities resulting in penetration and non-penetration were specified for both projectiles. More than one impact location on the target was specified.

The final series of airplane-scale tests is shown in figure B7. These tests involved Zylon fabric installed on a section of Boeing airplane fuselage structure. The tests were intended to permit evaluation of the ballistic performance of Zylon fabric interacting with insulation blankets, trim panels, and other airplane fuselage components. It was anticipated that sections salvaged from a Boeing 727 airplane would be used for this test, as they were available to SRI International. Impact by both projectiles for the airplane series tests were specified, with incidence conditions resulting in penetration and non-penetration for each.

For all cases of target configuration and projectile incidence conditions, it was expected that experiments would be repeated one time or more to permit some measure of uncertainty in the experimental results.

The tests actually performed by SRI deviated somewhat from the plan originally proposed. The most significant change was the deletion of the test series of figure B7 due to resource limitations.

Generic Fuselage Target / Large “Fragments”

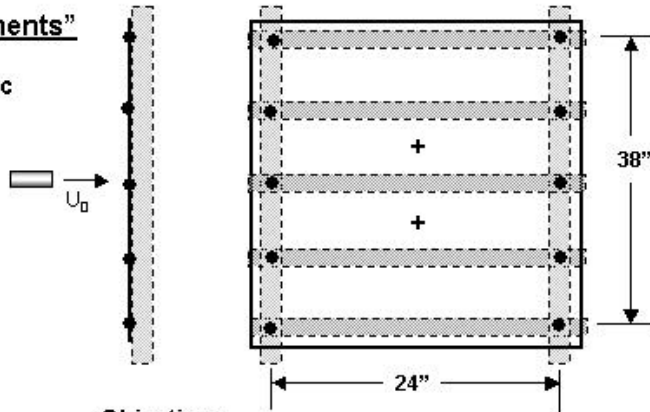
SRI Tests 1-10 – Alum. sheet with Zylon Fabric with 0.090 in. Al Skin

Projectiles:

- 4”W x 4”L x 0.50”t rubber
- $U_0 = 400$ ft/sec
- 2”W x 2”L x 0.25”t (~ 0.25 lb steel)
- 4”W x 4”L x 0.5”t (~ 2+ lb steel)
- $U_0 = [400 - 900]$ ft/sec
- Incidence angle = 90 degrees

Target:

- Aluminum sheet (2024-T4, 0.090”thickness)
- Zylon shield on front of skin, no separation
- Zylon - ply thickness to allow/not allow penetration
- 2 vertical “frames” with 5 horizontal “stringers” made from steel or aluminum beams
- Al and zylon bolted with washers at 5 discrete locations at frame/stringer intersections



Objectives:

1. Determine Zylon performance with Zylon shield in front of aluminum skin on .
2. Investigate the effects of larger fragments more representative of actual engine fragments.

Figure B5. Schematic for airplane scale test of Zylon fabric ballistic properties: aluminum sheet and Zylon fabric targets attached to ladder frame similar to commercial airplane structure.

41 in. x 41 in. Target / Large "Fragments"

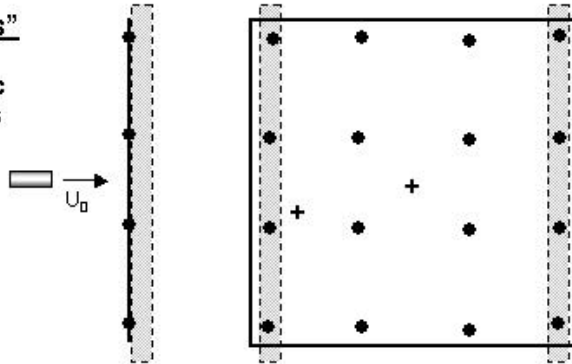
SRI Tests 11-20 – Aluminum sheet with Fabric / bolted side edges to frames & field bolts to skin

Projectiles:

- 2"x2"x0.25" and 4"x4"x0.5"
- Rectangular shape
- Steel 0.25 lb and 2 lb
- U_0 =[400-900 ft/s]
- Incidence angle = 0 degrees

Target:

- Aluminum sheet w/Zylon Fabric
- 41 in. x 41 in.
- Bolted at 16 discrete locations
- Projectile incident at two locations - center of panel & near edge attachment
- Zylon:
 - Ply thicknesses which do & do not allow fabric penetration



Objectives:

1. Determine Zylon performance in a cowling type application
2. Investigate the effects of impact proximity to attachment points

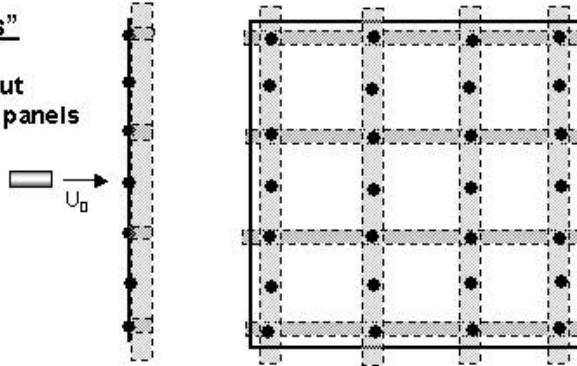
Figure B6. Schematic for airplane scale test of Zylon fabric ballistic properties: aluminum sheet and Zylon fabric targets attached to steel frame similar to commercial airplane fan cowl structure.

727 Fuselage Target / Large "Fragments"

Test Series 9.0 – 727 Fuselage with and without insulation blankets and trim panels

Projectiles:

- 2"x2"x0.25" and 4"x4"x0.5"
- rectangular shape
- Rubber and Steel 0.25 lb and 2 lb
- U_0 =[400-1000 ft/s]
- Incidence angle = [0, 45 degrees]



Target:

- Aluminum skin w/Zylon Fabric with and without insulation blankets and trim panels
- Bolted at discrete locations on frames (with washers)
- Projectile incident at various locations
- Zylon:
 - 20 ply and 40 ply thicknesses

Objectives:

1. Determine Zylon performance in a fuselage application
2. Investigate the effect of insulation blankets and trim panels

Figure B7. Schematic for airplane scale test of Zylon fabric ballistic properties: Zylon fabric shield installed of salvaged transport airplane fuselage section.

B4. CONCLUSION

Two series of tests have been designed to permit evaluation of the ballistic performance of Zylon fabric for use as engine rotor burst debris shield material in commercial airplanes. This report describes the sets of experiments as originally specified by Boeing. As The University of California and SRI International pursued their respective ballistic test programs, deviations from this test plan were chosen. In some cases tests series were eliminated due to lack of time and resources available to complete them, in other cases additional target configurations were added in attempts to improve the degree to which conditions of the targets and projectiles could be controlled.

APPENDIX C—RESULTS OF SMALL-SCALE IMPACT TESTS

Test No.	Target		Impactor			Impact			Residual Vel.		Pene.	K.E. Abs. (J)	SEA		Max. Slip (in.)	Impact Energy per Ply (J/ply)	Abs. Energy per Ply (J/ply)	Plies Perf. (# plies)	Yaw (degrees)					
	Matl	Mesh	No. of Edges Gripped	Areal Density (g/cm ²)	Type	Mass (g)	Distance from Center (in.)	Impact Vel. (m/s)	K.E. (ft-lb)	(m/s)			(ft/s)	(J/g/cm ³)						(ft-lb/ft ²)				
1A	Z	35x35	8	4	0.126	C	37	4.7	2.9	NA	NA	NA	NA	NA	0.93	NA	NA							
2A	Z	35x35	9	4	0.1418	C	37	NA	NA	40	131	22	none	none	0	3	3							
3A	Z	35x35	9	4	0.1418	C	37	3.65	5.4	109	358	220	162	NA	NA	NA	NA	0.24	NA					
4A	Z	35x35	9	4	0.1418	C	37	6.5	2.1	124	405	283	208	71	234	Y	189	139	1330	492	0.24	31	21	
5A	Z	35x35	9	4	0.1418	C	37	2.25	7	119	390	262	193	88	289	Y	119	88	837	310	0.24	29	13	
6A	Z	35x35	9	4	0.1418	C	37	8.25	9.25	154	505	439	324	NA	NA	Y	NA	NA	NA	NA	0.24	49	NA	
7A	Z	35x35	9	4	0.1418	C	37	2.25	0.75	160	524	473	349	NA	NA	Y	NA	NA	NA	NA	0.24	53	NA	
8A	Z	35x35	11	4	0.1733	C	37	4.75	4.5	138	452	352	259	none	none	N	352	260	2032	752	0.55	32	32	
9A	Z	35x35	11	4	0.1733	C	37	8.5	2.25	150	493	418	308	NA	NA	Y	NA	NA	NA	NA	0.8	38	NA	
10B	Z	35x35	2	4	0.0315	C	37	0.25	0.25	173	566	550	406	158	518	Y	89	65	2814	1041	0	275	44	2
11B	Z	35x35	4	4	0.063	C	37	0	0.25	117	384	253	187	31	101	Y	236	174	3739	1384	0.125	63	59	4
12B	Z	35x35	4	4	0.063	C	37	0.75	0.25	NA	NA	NA	NA	88	287	Y	NA	NA	NA	NA	0.063	NA	NA	4
13B	Z	35x35	6	4	0.0945	C	37	0.25	0.25	111	364	228	168	0	0	N	228	168	2413	893	0.063	38	38	1
14B	Z	35x35	8	4	0.126	C	37	0	0.25	158	518	462	341	0	0	N	462	341	3667	1357	0.063	58	58	1
15B	Z	35x35	6	4	0.0945	C	37	0	0	154	505	439	324	95	311	Y	273	201	2887	1068	0.063	73	45	6
16B	Z	35x35	4	4	0.063	C	37	0	0.25	133	436	327	241	87	285	Y	187	138	2972	1100	0.063	82	47	4
17B	Z	35x35	6	4	0.0945	C	37	0	0	180	590	599	442	114	374	Y	359	265	3799	1406	0.125	100	60	6
18B	Z	35x35	6	4	0.0945	C	37	0.25	0	0	0	0	0	117	384	Y	NA	NA	NA	NA	0.063	NA	NA	6
19B	Z	35x35	6	4	0.0945	C	37	0	0	NA	NA	NA	NA	37	121	Y	Y	Y	0	0	0.063	NA	0	6
20B	Z	35x35	6	4	0.0945	C	37	0.13	0.25	86	282	137	101	0	0	N	137	101	1448	536	0.125	23	23	0
21B	Z	35x35	6	4	0.0945	C	37	0.25	0	137	449	347	256	60	197	Y	281	207	2970	1099	0.063	58	47	6
22B	Z	35x35	6	4	0.0945	C	37	0	0	142	466	373	275	45	148	Y	336	248	3551	1314	0.063	62	56	6
23B	Z	35x35	6	4	0.0945	C	37	0.25	0.125	109	358	220	162	0	0	N	220	162	2326	861	0.063	37	37	0
24C	Z	35x35	6	4	0.0945	C	37	0.25 ^c	0.25 ^c	159	522	468	345	NA	NA	Y	Y	Y	Y	Y	0.125	78	6	6
25C	Z	35x35	6	4	0.0945	C	37	0.25 ^c	0.25 ^c	141	462	368	271	97	318	Y	194	143	2050	759	0.063	61	32	6
26B	Z	35x35	10	4	0.1575	C	37	0	0	154	505	439	324	86	282	Y	302	223	1917	709	0.188	44	30	10
27C	Z	35x35	6	4	0.0945	C	37	0.25 ^c	0 ^c	216	708	863	637	NA	NA	Y	Y	Y	Y	Y	0.063	144	6	6
28C	Z	35x35	6	4	0.0945	C	37	0.25 ^c	0 ^c	175	574	567	418	139	456	Y	209	154	2213	819	0.125	94	35	6
29C	Z	35x35	6	4	0.0945	C	37	0 ^c	0 ^c	117	384	253	187	NA	NA	Y	Y	Y	Y	Y	0.125	42	6	6
30C	Z	35x35	6	4	0.0945	C	37	0 ^c	0 ^c	130	426	313	231	NA	NA	Y	Y	Y	Y	Y	0.063	52	6	6
31C	Z	35x35	6	4	0.0945	C	37	0 ^c	0 ^c	107	351	212	156	36	118	Y	188	139	1988	735	0.063	35	31	6
32B	K	29x29	6	4	0.0928	C	37	0	0	119	390	262	193	NA	NA	Y	Y	Y	Y	Y	0.031	44	6	6
33B	K	29x29	6	4	0.0928	C	37	0	0	102	335	192	142	0	0	N	192	142	2075	768	0.063	32	32	0
34B	K	29x29	6	4	0.0928	C	37	0	0	77	253	110	81	0	0	N	110	81	1182	438	0.031	18	18	0
35B	K	29x29	6	4	0.0928	C	37	0	0	125	410	289	213	57	187	Y	229	169	2468	913	0.031	48	38	6
36B	K	29x29	6	4	0.0928	C	37	0	0	91	298	153	113	0	0	N	153	113	1652	611	0.063	26	26	0
37B	K	29x29	6	4	0.0928	C	37	0.25	0.125	115	377	245	180	0	0	N	245	180	2638	976	0.031	41	41	0
38B	Z	35x35	6	4	0.0945	C	37	0.25	0	110	361	224	165	0	0	N	224	165	2369	876	0.125	37	37	0
39B	Z	35x35	6	4	0.0945	C	37	0.25	0.25	185	607	633	467	173	567	Y	79	59	841	311	0.125	106	13	6
40B	K	29x29	6	4	0.0928	C	37	0	0	251	823	1166	860	249	817	Y	19	14	199	74	0.125	194	3	6
41B	K	29x29	6	4	0.0928	C	37	0	0	211	692	824	608	199	653	Y	91	67	981	363	0.125	137	15	6
42B	K	29x29	6	4	0.0928	C	37	0.25	0.25	163	535	492	363	125	410	Y	202	149	2183	808	0.063	82	34	6
43B	K	29x29	6	4	0.0928	C	37	0	0	215	705	855	631	178	584	Y	269	198	2900	1073	0.063	143	45	6
44B	K	29x29	6	4	0.0928	C	37	0	0	220	722	895	660	162	531	Y	410	302	4419	1635	0.063	149	68	6
45B	Z	35x35	6	4	0.0945	C	37	0	0.375					149	489	Y	Y	Y	Y	Y	0.063			6

Test No.	Target				Impactor			Impact				Residual Vel. (ft/s)	Pene. (J)	K.E. Abs. (ft.lb)	SEA (J/g/cm ²) (ft.lb/ft ²)	Max. Slip (in.)	Impact Energy per Ply (J/ply)	Abs. Energy per Ply (J/ply)	Plies Perf. (# plies)	Yaw (degrees)					
	Mat'l	Mesh	No. of Plies	B.C. Edges Gripped	Areal Density (g/cm ²)	Type	Mass (g)	Distance from Center x (in.), y (in.)	Impact Vel.		K.E. (J)										(ft.lb)	(m/s)	(ft/s)		
									Impact Vel. (m/s)	Impact Vel. (ft/s)															
46B	Z	35x35	6	4	0.0945	C	37	0	0	104	77	1101	0.063	17	6	0									
47E	Z	35x35	6	2	0.0945	C	37	0	0.25	75	246	104	77	0	N	104	77	1101	0.063	17	6	0			
48E	Z	35x35	6	2	0.0945	C	37	0	0.125					159	522	Y						6	0		
49E	Z	35x35	6	2	0.0945	C	37	0.25	0.25	171	561	541	399	136	446	Y	199	147	2104	778	90	33	6	2	
50E	Z	35x35	6	2	0.0945	C	37	0	0	200	656	740	546	0	0	Y	740	546	7831	2897	123	123	6		
51E	Z	35x35	6	2	0.0945	C	37	0.13	0	57	187	60	44	0	0	N	60	44	636	235	10	10	0	2	
52E	Z	35x35	6	2	0.0945	C	37	0	0	189	620	661	487	NA	NA	Y								6	
53E	Z	35x35	6	2	0.0945	C	37	0.25	0	76	249	107	79	0	0	N	107	79	1131	418	18	18	0	2	
54E	Z	35x35	6	2	0.0945	C	37	0.25	0.25	111	364	228	168	0	0	N	228	168	2412	892	38	38	1	5	
55E	Z	35x35	6	2	0.0945	C	37	0	0	144	472	384	283	30	98	Y	367	271	3883	1437	64	61	6	0	
56E	Z	35x35	6	2	0.0945	C	37	0	0	152	499	427	315	27	89	Y	414	305	4380	1621	71	69	6	0	
57E	K	29x29	6	2	0.0928	C	37	0	0	203	666	762	562	165	541	Y	259	191	2789	1032	43	43	6	2	
58E	K	29x29	6	2	0.0928	C	37	0	0	148	485	405	299	38	125	Y	379	279	4081	1510	68	63	6	0	
59E	K	29x29	6	2	0.0928	C	37	0	0	131	430	317	234	10	33	Y	316	233	3403	1259	53	53	6	0	
60E	K	29x29	6	2	0.0928	C	37	0	0	254	833	1194	880	229	751	Y	223	165	2408	891	199	37	6	0	
61E	K	29x29	6	2	0.0928	C	37	0	0	216	708	863	637	190	623	Y	195	144	2105	779	144	33	6	0	
62E	K	29x29	6	2	0.0928	C	37	0	0	267	876	1319	973	241	790	Y	244	180	2634	975	220	41	6		
63E	K	29x29	6	2	0.0928	C	37	0	0	197	646	718	530	152	499	Y	291	214	3132	1159	120	48	6	0	
64E	K	29x29	6	2	0.0928	C	37	0	0	79	259	115	85	0	0	N	115	85	1245	461	19	19	0	3	
65E	Z	35x35	6	2	0.0945	C	37	0	0	241	790	1074	793	229	751	Y	104	77	1104	409	179	17	6	5	
66E	Z	35x35	6	2	0.0945	C	37	0	0					237	777	Y								6	
67E	Z	35x35	6	2	0.0945	C	37	0	0.25	191	626	675	498	140	459	Y	312	230	3305	1223	112	52	6	0	
68E	Z	35x35	6	2	0.0945	C	37	0	0	267	876	1319	973	203	666	Y	556	410	5889	2179	220	93	6	18	
69E	Z	35x35	6	2	0.0945	C	37	0	0	229	751	970	716	216	708	Y	107	79	1133	419	162	18	6	0	
70E	Z	35x35	6	2	0.0945	C	37	0	0	241	790	1074	793	216	708	Y	211	156	2237	828	179	35	6	8	
71E	Z	35x35	6	2	0.0945	C	37	0	0	191	626	675	498	156	512	Y	225	166	2378	880	112	37	6	12	
72E	Z	35x35	6	2	0.0945	C	37	0	0	241	790	1074	793	229	751	Y	104	77	1104	409	179	17	6	0	
73B	K	35x35	6	4	0.0945	C	37	0	0	254	833	1194	880	229	751	Y	223	165	2364	875	199	37	6	11	
74B	K	29x29	6	4	0.0309	C	37	0	0	197	646	718	530	184	604	Y	92	68	2963	1096	359	46	2	2	
75B	K	29x29	6	4	0.0928	C	37	0	0	236	774	1030	760	210	689	Y	215	158	2313	856	172	36	6	2	
76B	K	29x29	6	4	0.0928	C	37	0	0	302	991	1687	1245	276	905	Y	278	205	2997	1109	281	46	6	0	
77B	Z	35x35	6	4	0.0945	C	37	0	0	289	948	1545	1140	250	820	Y	389	287	4115	1523	258	65	6	0	
78P	Z	35x35	6	4	0.0945	C	37	0.13	0.125	197	646	718	530	0	0	N	718	530	7598	2811	120	120	0	2	
79P	Z	35x35	4	4	0.063	C	37	0	0	154	505	439	324	0	0	N	439	324	6964	2577	110	110	0	7	
80P	Z	35x35	4	4	0.063	C	37	0	0	243	797	1092	806	0	0	N	##	806	17340	6416	273	273	4	4	
81B	Z	35x35	6	4	0.0945	C	37	0	0	328	1076	1990	1468	302	991	Y	303	224	3207	1186	332	51	6	13	
82E	K	29x29	6	2	0.0928	C	37	0	0	126	413	294	217	0	0	N	294	217	3166	1172	49	49	0	4	
83E	K	29x29	6	2	0.0928	C	37	0	0	256	840	1212	894	250	820	Y	56	41	605	224	202	9	6	0	
84E	Z	35x35	6	2	0.0945	C	37	0	0	145	476	389	287	0	0	N	389	287	4116	1523	65	65	0	0	
85E	Z	35x35	6	2	0.0945	C	37	0	0	158	518	462	341	30	98	Y	445	328	4711	1743	77	74	6	0	
86E	Z	35x35	6	2	0.0945	C	37	0	0	191	626	675	498	131	430	Y	357	264	3782	1399	112	60	6	12	
87E	Z	35x35	6	2	0.0945	C	37	0	0	342	1122	2164	1596	315	1033	Y	328	242	3473	1285	361	55	6	0	
88P	Z	35x35	4	4	0.063	C	37	0	0	263	863	1280	944	29	95	Y	##	932	20065	7424	1	320	316	4	0
89P	Z	35x35	4	4	0.063	C	37	0.25	0	276	905	1409	1039	217	712	Y	538	397	8541	3160	352	135	4	8	

Test No.	Target				Impactor				Impact				Residual Vel. (ft/s)	Pene. (Y/N)	K.E. Abs. (J)	SEA (ft ³ /lb/ft ³)	Max. Slip (in.)	Impact Energy per Ply (J/ply)	Abs. Energy per Ply (J/ply)	Plies Perf. (# plies)	Yaw (degrees)										
	Mesh	No. of Plies	B.C. Edges Gripped	Areal Density (g/cm ²)	Type	Mass (g)	Distance from Center x (in.)	y (in.)	Impact Vel. (m/s)	(ft/s)	K.E. (J)	(ft-lb)										(m/s)	(ft/s)	(J)	(ft-lb)	(J/g/cm ³)	(in.)	(J/ply)	(J/ply)	(# plies)	(degrees)
90P	Z	35x35	4	4	0.063	C	37	0	0	276	905	1409	1039	245	804	Y	299	220	4743	1755	0.375	352	75	4	0						
91P	Z	35x35	4	4	0.063	C	37	0	0	223	731	920	679	0	0	N	920	679	14603	5403	0.75	230	230	4	10						
92P	Z	35x35	4	4	0.063	C	37	0	0	250	820	1156	853	202	663	Y	401	296	6371	2357	0.5	289	100	4	0						
93P	Z	35x35	4	4	0.063	C	37	0	0	342	1122	2164	1596	321	1053	Y	258	190	4089	1513	0	541	64	4	0						
94P	Z	35x35	4	4	0.063	C	37	0	0	175	574	567	418	0	0	N	567	418	8993	3327	0.5	142	142	0	9						
96P	Z	35x35	4	4	0.063	C	37	0	0	315	1033	1836	1354	301	987	Y	160	118	2532	937	0	459	40	4	0						
97P	Z	35x35	4	4	0.063	C	37	0	0	302	991	1687	1245	289	948	Y	142	105	2256	835	0	422	36	4	0						
98P8	Z	35x35	4	8	0.063	C	37	0.13	0	210	689	816	602	0	0	N	816	602	12950	4792	1	204	204	0	0						
99P8	Z	35x35	4	8	0.063	C	37	0	0	203	666	762	562	0	0	Y	0	0	0	0	0.375	0	0	4	22						
100P8	Z	35x35	4	8	0.063	C	37	0.13	0	210	689	816	602	0	0	N	816	602	12950	4792	1	204	204	0	0						
101P8	Z	35x35	4	8	0.063	C	37	0	0	263	863	1280	944	0	0	Y	0	0	0	0	0.375	0	0	4	0						
102P8	Z	35x35	4	8	0.063	C	37	0	0	223	731	920	679	192	630	Y	238	176	3778	1398	0.5	230	60	4	0						
103P8	Z	35x35	4	8	0.063	C	37	0	0	302	991	1687	1245	288	945	Y	153	113	2426	897	0.25	422	38	4	0						
104P8	Z	35x35	4	8	0.063	C	37	0	0	296	971	1621	1196	278	912	Y	191	141	3034	1123	0.25	405	48	4	1						
105P8	Z	35x35	4	8	0.063	C	37	0	0	263	863	1280	944	236	774	Y	249	184	3956	1464	0.375	320	62	4	0						
106P8	Z	35x35	4	8	0.063	C	37	0	0	263	863	1280	944	235	771	Y	258	190	4095	1515	0.25	320	64	4	0						
107P8	Z	35x35	4	8	0.063	C	37	0	0	328	1076	1990	1468	308	1010	Y	235	174	3735	1382	0.125	498	59	4	1						
108P	K	29x29	4	4	0.0618	C	37	0.25	0	250	820	1156	853	247	810	Y	28	20	446	165	0.125	289	7	4	0						
109P	K	29x29	4	4	0.0618	C	37	0	0	230	754	979	722	177	581	Y	399	294	6453	2388	0.375	245	100	4	0						
110P	K	29x29	4	4	0.0618	C	37	0	0	164	538	498	367	0	0	N	498	367	8046	2977	0.5	124	124	4	8						
111P	K	29x29	4	4	0.0618	C	37	0	0	197	646	718	530	39	128	Y	690	509	11155	4127	0.5	179	172	4	0						
112P	K	29x29	4	4	0.0618	C	37	0	0	289	948	1545	1140	282	925	Y	74	55	1196	442	0.125	366	18	4	6						
113P	K	29x29	4	4	0.0618	C	37	0.25	0.25	315	1033	1836	1354	306	1004	Y	103	76	1672	619	0.125	459	26	4	0						
114EM	Z	35x35	6	2	0.0945	C	37	0	0	191	626	675	498	114	374	Y	434	320	4598	1701	0.125	112	72	6	0						
115EM	Z	35x35	6	2	0.0945	C	37	0	0	145	476	389	287	14	46	Y	385	284	4078	1509	0.375	65	64	6	6						
116EM	Z	35x35	6	2	0.0945	C	37	0	0	177	581	580	428	79	259	Y	464	342	4911	1817	0.25	97	77	6	0						
117EM	Z	35x35	6	2	0.0945	C	37	0	0	92	302	157	115	0	0	N	157	115	1657	613	0.188	26	26	0	2						
118EM	Z	35x35	6	2	0.0945	C	37	0	0	151	495	422	311	62	203	Y	351	259	3711	1373	0.125	70	58	6	2						
119EM	Z	35x35	6	2	0.0945	C	37	0	0	154	505	439	324	22	72	Y	430	317	4548	1683	0.375	73	72	6	2						
120EM	Z	35x35	6	2	0.0945	C	37	0	0	250	820	1156	853	195	640	Y	453	334	4791	1773	0.313	193	75	6	0						
121EM	Z	35x35	6	2	0.0945	C	37	0	0	165	541	504	372	55	180	Y	448	330	4738	1753	0.25	84	75	6	0						
122EM	Z	35x35	6	2	0.0945	C	37	0	0	243	797	1092	806	216	708	Y	229	169	2426	898	0.188	182	38	6	12						
123EM	Z	35x35	6	2	0.0945	C	37	0	0	237	777	1039	766	213	699	Y	200	147	2114	782	0.25	173	33	6	0						
124PC	Z	35x35	4	4	0.063	C	37	0	0	250	820	1156	853	185	607	Y	523	386	8303	3072	0.5	289	131	4	9						
125PC	Z	35x35	4	4	0.063	C	37	0	0	217	712	871	643	70	230	Y	780	576	12389	4584	0.75	218	195	4	2						
126PC	Z	35x35	4	4	0.063	C	37	0	0	230	754	979	722	96	315	Y	808	596	12828	4746	0.625	245	202	4	3						
127PC	Z	35x35	4	4	0.063	C	37	0	0	158	518	462	341	0	0	N	462	341	2712	2712	0.625	115	115	1	5						
128PC	Z	35x35	4	4	0.063	C	37	0.25	0	204	689	770	568	0	0	N	770	568	12221	4522	1.25	192	192	2	2						
129PC	Z	35x35	4	4	0.063	C	37	0	0	204	689	770	568	0	0	N	770	568	12221	4522	1.313	192	192	3	0						
130PC	Z	35x35	4	4	0.063	C	37	0	0	230	754	979	722	96	315	Y	808	596	12828	4746	0.625	245	202	4	3						
131PC	Z	35x35	4	4	0.063	C	37	0	0	263	863	1280	944	252	827	Y	105	77	1664	616	0.625	320	26	4	5						
132PC	Z	35x35	4	4	0.063	C	37	0	0	328	1076	1990	1468	296	971	Y	369	272	5864	2170	0.125	498	92	4	1						
133PC	Z	35x35	4	4	0.063	C	37	0	0	315	1033	1836	1354	301	987	Y	160	118	2532	937	0	459	40	4	1						
134P8C	Z	35x35	4	8	0.063	C	37	0	0	237	777	1039	766	129	423	Y	731	539	11607	4295	0.75	260	183	4	9						

Test No.	Target		Impactor		Impact			Residual Vel.	Pene.	K.E. Abs. (J)	SEA (J/g/cm ³)	SEA (ft. lb/ft ²)	Max. Slip (in.)	Impact Energy per Ply (J/ply)	Abs. Energy per Ply (J/ply)	Plies Perf. (# plies)	Yaw (degrees)								
	Mesh	No. of Edges Gripped	Areal Density (g/cm ²)	Type	Mass (g)	Distance from Center x (in.)	y (in.)											Impact Vel. (m/s)	Impact Vel. (ft/s)	K.E. (J)					
135P8C	Z	35x35	4	8	0.063	C	37	0	0	230	754	979	722	156	512	Y	528	390	8388	3104	0.75	245	132	4	7
136P8C	Z	35x35	4	8	0.063	C	37	0	0	256	840	1212	894	199	653	Y	480	354	7616	2818	0.375	303	120	4	1
137P8C	Z	35x35	4	8	0.063	C	37	0	0	191	626	675	498	0	0	N	675	498	10713	3964	0.875	169	169	4	0
138P8C	Z	35x35	4	8	0.063	C	37	0	0	184	604	626	462	0	0	N	626	462	9942	3678	1	157	157	0	0
139P8C	Z	35x35	4	8	0.063	C	37	0	0	210	689	816	602	0	0	Y	816	602	12950	4792	1.125	204	204	4	0
140P8C	Z	35x35	4	8	0.063	C	37	0	0	263	863	1280	944	212	695	Y	448	331	7114	2632	0.5	320	112	4	3
141P8C	Z	35x35	4	8	0.063	C	37	0	0	302	991	1687	1245	272	892	Y	319	235	5057	1871	0.5	422	80	4	2
142P8C	Z	35x35	4	8	0.063	C	37	0	0	315	1033	1836	1354	293	961	Y	247	183	3928	1453	0.125	459	62	4	2
143P8C	Z	35x35	4	8	0.063	C	37	0	0	309	1014	1766	1303	286	938	Y	253	187	4019	1487	0.25	442	63	4	4
144C	Z	35x35	6	4	0.0945	C	37	0	0	236	774	1030	760	180	590	Y	431	318	4561	1687	0.063	172	72	6	0
145C	Z	35x35	6	4	0.0945	C	37	0.25	0	191	626	675	498	147	482	Y	275	203	2911	1077	0.063	112	46	6	8
146C	Z	35x35	6	4	0.0945	C	37	0	0	184	604	626	462	133	436	Y	299	221	3165	1171	0.125	104	50	6	1
147C	Z	35x35	6	4	0.0945	C	37	0	0	77	253	110	81	0	0	N	110	81	1161	429	0.125	18	18	0	0
148C	Z	35x35	6	4	0.0945	C	37	0	0	171	561	541	399	136	446	Y	199	147	2104	778	0.063	90	33	6	0
149C	Z	35x35	6	4	0.0945	C	37	0	0	166	544	510	376	131	430	Y	192	142	2035	753	0.125	85	32	6	0
150C	Z	35x35	6	4	0.0945	C	37	0	0	123	403	280	206	59	194	Y	215	159	2280	844	0.063	47	36	6	0
151C	Z	35x35	6	4	0.0945	C	37	0	0	276	905	1409	1039	237	777	Y	370	273	3917	1449	0.125	235	62	6	0
152C	Z	35x35	6	4	0.0945	C	37	0	0	267	876	1319	973	233	764	Y	315	232	3328	1231	0.063	220	52	6	0

^aCylindrical projectile

^bTests 7-15 are measured from the star corner instead of the center

^cDistance from corner point

A = random shots

B = 4 clamp, center shots

C = 4 clamp, corner shots

E = 2 clamp, center shots

P = 4 pegs

P8 = 8 pegs

EM = 2 clamp, center midway shots

Z = Zylon

K = Kevlar

APPENDIX D—DATA REDUCTION BACKGROUND

During the experimental investigation of multiple plies of high strength fabric, two critical measurements were collected to specify the ballistic characteristics of Zylon: (1) initial impact velocity, V_o and (2) residual impact velocity, V_f . From these two measured quantities, several important values were obtained: (1) impact kinetic energy, (2) absorbed kinetic energy, (3) specific energy absorbed, (4) impact energy per ply, and (5) absorbed energy per ply. In addition, the areal density played an important role in the data reduction.

The impact kinetic energy is calculated by the basic equation

$$\text{Impact K.E.} = \frac{1}{2}(M_p)(V_o)^2 \quad (\text{D-1})$$

where M_p is the mass in grams of the projectile, and V_o is the initial velocity in meters per second.

To determine the amount of kinetic energy absorbed by the fabric barrier, the difference between the impact and residual kinetic energy of the projectile is calculated with the following equation:

$$\text{Absorbed K.E.} = \left[\frac{1}{2}(M_{\text{projectile}})(V_{\text{impact}})^2 \right] - \left[\frac{1}{2}(M_{\text{projectile}})(V_{\text{residual}})^2 \right] \quad (\text{D-2})$$

The specific energy absorbed (SEA) is the kinetic energy absorbed by the fabric barrier divided by its areal density.

$$\text{SEA} = \frac{\text{Absorbed K.E.}}{\text{Areal Density}} \quad (\text{D-3})$$

The impact and absorbed energy per ply is calculated by dividing the respective values by the number of plies tested.

$$\text{Impact Energy per Ply} = \frac{\text{Impact K.E.}}{\text{No. of Plies}} \quad (\text{D-4})$$

$$\text{Absorbed Energy per Ply} = \frac{\text{Absorbed K.E.}}{\text{No. of Plies}} \quad (\text{D-5})$$

Finally, the areal density is determined by the following equation:

$$\text{Areal Density} = \rho \times \text{No.ofPlies} \quad (\text{D-6})$$

where ρ is equal to $0.01575 \frac{\text{grams}}{(\text{cm}^2)(\text{ply})}$ for Zylon and $0.01546 \frac{\text{grams}}{(\text{cm}^2)(\text{ply})}$ for Kevlar®.

In this experimental investigation, the impact and absorbed energy per ply were used to determine the ballistic behavior of the fabric barriers. By plotting impact energy per ply versus absorbed energy per ply, the perforation limits and performance at high impact energies can be identified. If perforation does not occur in a test, the fabric barrier will have absorbed 100% of the impact energy emitted by the small-scale projectile. Hence, a plot of the impact and absorbed energy per ply will be a straight line. When the projectile nearly perforates the entire fabric barrier (penetrates but stops), the amount of absorbed energy has reached its limit. This pinnacle signifies the perforation limit of the fabric barrier. When the projectile completely perforates the fabric barrier at higher impact energies, the impact and absorbed energy per ply plot is expected to exhibit a horizontal line, which continues from the absorbed energy level of the perforation limit. Ideally, each ply of the fabric barrier should demonstrate a constant absorbed energy value when the impact energies exceed the perforation limits. Intuitively, the absorbed energy per ply cannot increase with increasing impact energy per ply in the complete perforation range. From previous works, the absorbed energy per ply is supposed to decline from the absorbed energy limit as the impact energy per ply increases. The degree to which the absorbed energy decreases is a direct function of material characteristics and impact dynamics.

APPENDIX E—DERIVATION FOR THE FORCE-DEFLECTION EQUATION

To determine the amount of force to deflect a rigidly held linear elastic yarn of fiber, the following equation was derived:

$$E(v-1) = \frac{P}{A_o} \quad (\text{E-1})$$

$$v = \frac{\sqrt{\left(\left(\frac{l_o}{2}\right)^2 + (\delta)^2\right)}}{\left(\frac{l_o}{2}\right)^2} \quad (\text{E-2})$$

where E is the elastic modulus of the yarn, l_o is the original length of the yarn, δ is the deflection, A_o is the cross sectional area of the yarn of the fiber, and P is the amount of force exerted on the yarn at the center.

Solution of the equation results in the following equation, where the force can be determined, given the variables.

$$P = EA_o \left(\sqrt{\frac{\left(\left(\frac{l_o}{2}\right)^2 + (\delta)^2\right)}{\left(\frac{l_o}{2}\right)^2}} - 1 \right)$$